

## Structural and Magnetic Properties of Biocompatible Iron Oxide Nanoparticles for Medical Applications

Amal Nasser

Schlüsseltechnologien / Key Technologies Band / Volume 296 ISBN 978-3-95806-837-7



Forschungszentrum Jülich GmbH Jülich Centre for Neutron Science (JCNS) Neutronenmethoden (JCNS-4)

# Structural and Magnetic Properties of Biocompatible Iron Oxide Nanoparticles for Medical Applicationst

**Amal Nasser** 

Schriften des Forschungszentrums Jülich Reihe Schlüsseltechnologien / Key Technologies Bibliografische Information der Deutschen Nationalbibliothek. Die Deutsche Nationalbibliothek verzeichnet diese Publikation in der Deutschen Nationalbibliografie; detaillierte Bibliografische Daten sind im Internet über http://dnb.d-nb.de abrufbar.

Herausgeber Forschungszentrum Jülich GmbH

und Vertrieb: Zentralbibliothek, Verlag

52425 Jülich

Tel.: +49 2461 61-5368 Fax: +49 2461 61-6103 zb-publikation@fz-juelich.de

www.fz-juelich.de/zb

Umschlaggestaltung: Grafische Medien, Forschungszentrum Jülich GmbH

Druck: Grafische Medien, Forschungszentrum Jülich GmbH

Copyright: Forschungszentrum Jülich 2025

Schriften des Forschungszentrums Jülich Reihe Schlüsseltechnologien / Key Technologies, Band / Volume 296

D 91 (Diss. TU München, 2025)

ISSN 1866-1807 ISBN 978-3-95806-837-7

Vollständig frei verfügbar über das Publikationsportal des Forschungszentrums Jülich (JuSER) unter www.fz-juelich.de/zb/openaccess.



This is an Open Access publication distributed under the terms of the <u>Creative Commons Attribution License 4.0</u>, which permits unrestricted use, distribution, and reproduction in any medium, provided the original work is properly cited.

## Abstract

This thesis presents a comprehensive investigation of the structural and magnetic properties of biocompatible iron oxide nanoparticles coated with three different ligand materials: sodium citrate, (3-aminopropyl)triethoxysilane (APTES), and dextran. The influence of the coating agents on the agglomeration of iron oxide nanoparticles and their oxidation stability over time was studied. Various experimental techniques were used to characterize the structural and magnetic properties of the coated nanoparticles, including cryogenic transmission electron microscopy (cryo-TEM), magnetometry, and small-angle X-ray and neutron scattering. The results show that the coatings successfully stabilize the particles leading to various aggregate structures and sizes. These samples exhibit large saturation magnetization levels close to those of bulk iron oxide and a small coercivity as evidenced by the magnetization hysteresis loop at room temperature. We find that the zero-fieldcooled (ZFC) and field-cooled (FC) magnetization behaviour is influenced by magnetic interactions among the nanoparticles inside clusters. The interaction leads to a shift of the blocking temperature to higher values and a flattening of the FC curves at lower temperatures. Notably, the blocking temperature of the citrate-coated samples were lower than would have been expected for the large clustered structure. Furthermore, for this sample magnetic small-angle neutron scattering (SANS) reveals a multidomain structure, with the magnetic size corresponding to half of the cluster size as observed by SAXS. In the aging study, Mössbauer spectroscopy was used to follow the changes in  $Fe^{2+}$  and Fe<sup>3+</sup> composition over time, while magnetometry allowed the determination of the net

Fe<sup>3+</sup> composition over time, while magnetometry allowed the determination of the net magnetization. In all systems, rapid oxidation was observed after less than 0.1 days (the time between the end of synthesis and the sealing of the samples under  $N_2$  atmosphere). This led to a complete oxidation of the magnetite nanoparticles to maghemite with the dextran coating, while the nanoparticles with citrate and APTES coating showed slower oxidation with 10% - 20% of the magnetite fraction after one month. The variation in oxidation behaviour is linked to the variations in particle size, which in turn are influenced by the coating agent and the synthesis method.

Micromagnetic simulations were performed with the Object Oriented Micromagnetic Framework (OOMMF) software for ensembles of randomly arranged and randomly connected nanoparticles. The "Theta Evolver" within OOMMF was used to include thermal fluctuations of the magnetic superspin moments of the nanoparticles to model the ZFC and FC curves, in addition to the magnetization hysteresis loops. The simulation results help us to understand the effect of exchange and dipolar inter-particle interactions on the energy barriers for magnetization reversal and, thus, on the magnetization hysteresis curves. This

Abstract

knowledge of the altered magnetic behaviour is required in tuning the synthesis route to obtain the desired magnetic properties for future medical applications.

Part of the results presented in this thesis was published in Ref. [1], and a second manuscript on micromagnetic simulations is in preparation.

## Kurzfassung

In dieser Arbeit werden die strukturellen und magnetischen Eigenschaften von biokompatiblen Eisenoxid-Nanopartikeln untersucht, die mit drei verschiedenen Liganden beschichtet sind: Natriumcitrat, (3-Aminopropyl)triethoxysilan (APTES) und Dextran. Der Einfluss der Beschichtungen auf die Agglomeration von Eisenoxid-Nanopartikeln und ihre Oxidationsstabilität im Laufe der Zeit wurde untersucht. Zur Charakterisierung der strukturellen und magnetischen Eigenschaften der beschichteten Nanopartikel wurden verschiedene experimentelle Techniken eingesetzt, darunter kryogene Transmissionselektronenmikroskopie (cryo-TEM), Magnetometrie sowie Röntgen- und Neutronenstreuung unter kleinen Winkeln. Die Ergebnisse zeigen, dass die Beschichtungen die Partikel erfolgreich stabilisieren und zu verschiedenen Aggregatstrukturen und -größen führen. Diese Proben weisen große Sättigungsmagnetisierungen auf, die denen des 'bulk' Eisenoxids nahe kommen. Ferner weisen sie eine geringe Koerzitivfeldstärke auf, wie die Magnetisierungshysteresekurven bei Raumtemperatur zeigen. Wir beobachten, dass die Magnetisierungskurven im nullfeldgekühlten Zustand (ZFC) und im feldgekühlten Zustand (FC) durch magnetische Wechselwirkungen zwischen den Nanopartikeln in den aus Nanopartikeln bestehenden Clustern beeinflusst werden. Die Wechselwirkungen führen zu einer Verschiebung der Blocking-Temperaturen zu höheren Werten und zu einer Abflachung der FC-Kurven bei niedrigeren Temperaturen. Bemerkenswert ist, dass die Blocking-Temperaturen der mit Citrat beschichteten Proben niedriger waren, als man es bei der großen Clusterstruktur erwarten würde. Darüber hinaus ergab die magnetische Kleinwinkel-Neutronenstreuung (SANS) für diese Probe eine Multidomänenstruktur, wobei die magnetische Größe der Hälfte der durch SAXS beobachteten Clustergröße entspricht.

In der Oxidationsstudie mittels Mössbauer-Spektroskopie konnten wir die Veränderungen der Fe<sup>2+</sup>- und Fe<sup>3+</sup>-Zusammensetzung im Laufe der Zeit verfolgen, während wir ferner mit Magnetometrie die Nettomagnetisierung bestimmen konnten. Bei allen Systemen wurde eine schnelle Oxidation nach weniger als 0,1 Tagen beobachtet (die Zeit zwischen dem Ende der Synthese und dem Versiegeln der Proben unter N<sub>2</sub>-Atmosphäre). Dies führte zu einer vollständigen Oxidation der Magnetit-Nanopartikel zu Maghemit in der Dextran-beschichteten Probe, während die Citrat- und APTES-beschichteten Proben eine langsamere Oxidation mit 10 - 20 % der Magnetitfraktion nach einem Monat zeigten. Die Unterschiede im Oxidationsverhalten hängen mit den Unterschieden in der Partikelgröße zusammen, die wiederum durch die Beschichtung und die Synthesemethode beeinflusst werden.

Mikromagnetische Simulationen wurden mit der Software Object Oriented Micromagnetic

Kurzfassung vi

Framework (OOMMF) für Ensembles aus zufällig angeordneten und zufällig verbundenen Nanopartikeln durchgeführt. Der "Theta Evolver" in OOMMF wurde verwendet, um thermische Fluktuationen der magnetischen Superspin-Momente der Nanopartikel einzubeziehen, um die ZFC- und FC-Kurven zu modellieren, zusätzlich zu den Magnetisierungshysteresekurven. Die Simulationsergebnisse helfen uns, die Auswirkungen von Austausch- und dipolaren Wechselwirkungen zwischen den Teilchen auf die Energiebarrieren für die Magnetisierungsumkehr und damit auf die Magnetisierungshysteresekurven zu verstehen. Dieses Wissen über das veränderte magnetische Verhalten ist erforderlich, um die Syntheserouten zu optimieren und die gewünschten magnetischen Eigenschaften für zukünftige medizinische Anwendungen zu erhalten.

Ein Teil der in dieser Arbeit vorgestellten Ergebnisse wurde in Ref. [1], veröffentlicht, und ein zweites Manuskript über mikromagnetische Simulationen ist in Vorbereitung.

## Contents

$\mathbf{A}$	bstra	ct		iii	
K	urzfa	ssung		v	
1	Intr 1.1 1.2		on ation	1 1 3	
2	The	oretica	al Background	5	
_	2.1		etism	5	
	2.1	2.1.1	Magnetic moments	5	
		2.1.2	Magnetization	8	
		2.1.3	Collective magnetism	9	
			2.1.3.1 Magnetic dipole interaction	9	
				10	
		2.1.4	~	14	
			2.1.4.1 Diamagnetism and paramagnetism	14	
			2.1.4.2 Ferromagnetism	16	
			2.1.4.3 Antiferromagnetism	17	
			2.1.4.4 Ferrimagnetism	17	
		2.1.5 Magnetic anisotropy		17	
2.1.6 Nanoparticle magnetism		Nanoparticle magnetism	20		
			2.1.6.1 Single domain particles	20	
			2.1.6.2 Superparamagnetism	22	
			2.1.6.3 Collective superspin states	24	
2.2 Scattering theory		ring theory	25		
		2.2.1	Basics of scattering	25	
		2.2.2	, , ,	28	
		2.2.3		30	
		2.2.4		31	
g ·			9	38	
		2.2.6	•	39	
	2.3	Mössb	ssbauer spectroscopy		

Contents

	2.4	Microi	magnetic simulations			
		2.4.2	The Stochastic Landau-Lifshitz equation			
3	Inst	truments				
	3.1	Small-	angle scattering	. 49		
		3.1.1	Gallium Anode Low Angle X-ray Instrument (GALAXI) & KWS-X:			
			The SAXS/WAXS Laboratory beamline			
		3.1.2	Small-Angle X-ray Scattering beamline for Materials Research (SAXS-			
			MAT) P62 beamline			
		3.1.3	Quokka, ANSTO			
	3.2		etometry devices			
		3.2.1	Superconducting Quantum Interference Device (SQUID)			
	3.3		enic Transmission Electron Microscopy			
	3.4		pauer spectroscopy			
	3.5	·	powder diffraction			
	3.6		tively Coupled Plasma Optical Emission Spectroscopy			
	3.7	Dynar	mic light scattering	. 60		
4	Wa		sed Iron Oxide nanoparticles	63		
	4.1		Oxides			
	4.2		Oxide synthesis			
	4.3		cterization techniques			
	4.4		ural characterization			
	4.5	-	etic characterization			
		4.5.1	Macroscopic magnetic properties			
		4.5.2	Magnetic cluster size			
			4.5.2.1 SANS at a zero field			
			4.5.2.2 SANS with applied magnetic fields			
	4.6		tion stability			
		4.6.1	Mössbauer spectroscopy			
		4.6.2	SQUID magnetometry			
		4.6.3	ASAXS			
	4.7		magnetic simulations			
		4.7.1	Single Iron Oxide nanospheres	. 98		
		4.7.2	Influence of inter-particle interactions onto the magnetic behaviour	404		
			of magnetic nanoparticle systems			
		4.7.3	Multi-core nanosphere-clusters	. 109		
5	Cor	nclusio	ns and outlook	113		
A	ckno	wledgn	nents	116		
T.i	st of	Figure	es	119		
اب	DU UI	u i i u i i	OD CO			

Contents	ix
List of Tables	123
Bibliography	127

## Abbreviations

APTES 3-aminopropyl-triethoxysilane

ASAXS Anomalous Small Angle X-ray Scattering

B47 APTES-coated SPIONs
C71 Citrate-coated SPIONs
D40 Dextran-coated SPIONs
DLS Dynamic Light Scattering

FCC Face-centered cubic

FeSO<sub>4</sub> Iron sulfate

FWHM Full width at half maximum

FC Field cooling

ICP-OES Inductively Coupled Plasma - Optical Emission Spectroscopy

IFT Indirect Fourier transform

LLG Landau-Lifschitz-Gilbert (equation)

MD Multi-domain

MRI Magnetic resonance imaging
MPI Magnetic particle imaging

OOMMF Object-oriented micromagnetic framework

PDI Polydispersity index

SANS Small Angle Neutron Scattering SAXS Small Angle X-ray Scattering

SD Single-domain

SFM Superferromagnetic

SLD Scattering length density

Abbreviations xii

SPION Superparamagnetic iron oxide nanoparticle

SPM Superparamagnetism

SQUID Superconducting Quantum Interference Device

SSG Superspin glass

 $T_B$  Blocking temperature

 $T_g$  Glass transition temperature

 $T_N$  Néel temperature

TEM Transmission Electron Microscopy

XANES X-ray Absorption Near Edge Structure

 $egin{array}{ll} {
m XRD} & {
m X-ray\ Diffraction} \\ {
m ZFC} & {
m Zero\ field\ cooling} \\ \end{array}$ 

Table 4.3 is for a list of samples

## Chapter 1

## Introduction

#### 1.1 Motivation

Iron oxide nanoparticles with diameters ranging from 1 to 100 nm are considered optimal tools for in vivo medical applications for both diagnosis and therapy [2, 3, 4]. Larger nanoparticles (D > 100 nm) tend to aggregate under physiological conditions and are rapidly absorbed by macrophages in the bloodstream, which can limit their usability in medical applications. Employing smaller nanoparticles not only enhances the stability in the bloodstream but also improves the uptake by cells [5]. Such nanoparticles exhibit a large magnetic susceptibility, enabling a large and rapid response. Furthermore, they reduce side effects, i.e., in direct drug delivery with the help of the magnetic nanoparticles with their ability to preferentially accumulate at tumor sites and limit off-target side effects [6]. They find applications in various medical fields for diagnostics such as in magnetic resonance imaging (MRI) as contrast agents [7, 8], or in therapy such as targeted drug delivery [9, 10] and hyperthermia [11, 12]. Furthermore, a novel imaging technique, i.e. Magnetic Particle Imaging (MPI) has gained increasing attention recently due to its enhanced sensitivity and much less expensive logistics [13]. However, significant limitations and challenges remain to be addressed before these nanoparticles can be implemented in clinical use [14]. For example, no magnetic drug delivery system is currently used in clinical practice due to the challenges of producing magnetic carriers with strong and fast enough responses to external magnetic fields under arterial flow conditions, in particular for optimal accumulation of drugs in the bloodstream [15].

Superparamagnetic iron oxide nanoparticles (SPIONs) are a type of magnetic nanoparticles that have gained special attention due to their proven biocompatibility and strong magnetic properties, making them super candidates for different medical applications. SPIONs exhibit superparamagnetic behaviour at a particle size of 5-20 nm. In most cases, they are composed of an iron oxide core and a ligand shell. The specific iron oxide phase composition varies significantly between different synthesis routes and also between core sizes. In the majority of cases, it is a composition of maghemite, magnetite, and wüstite. SPIONs are characterized by having a single magnetic domain. If in addition the magnetization reversal of the single-domain particle occurs via coherent rotation one

1.1. Motivation 2

can associate it with a so-called "superspin" [16, 17, 18]. In this case, the magnetic moments of the nanoparticles behave similarly to paramagnetic moments in the presence of an external magnetic field; however, they are characterized by large magnetic moments  $(m \approx 10^3 - 10^5 \mu_B)$  [19].

SPIONs are promising tools in theranostics, a field that combines therapy and diagnostics [20]. They have the potential to significantly enhance cancer treatment through a combination of imaging and magnetic hyperthermia [21, 22]. SPIONs can be used to identify disease states and deliver therapy simultaneously, allowing the following of the therapy by imaging. Magnetic hyperthermia takes advantage of the heat produced by exposing magnetic nanoparticles to an alternating current (AC) magnetic field [23]. The heating efficiency is characterized by a specific absorption rate (SAR). The mechanism responsible for the heat dissipated is the switching and relaxation behaviour of the particle's magnetic moments. Thus, it is essential to develop high-quality particles with large saturation magnetization that can respond with large SARs to external magnetic fields in the bloodstream.

In most medical applications, magnetic nanoparticles must have a highly crystalline structure and well-controlled physicochemical properties, including particle size [24], shape [25], and surface characteristics [26]. These factors, along with the composition of the iron oxide phases [27], significantly determine the final magnetic properties of the nanoparticles. Therefore, controlling synthesis conditions and the stabilization process is crucial for improving magnetic properties.

Recently, increased interest has focused on multi-core nanoparticles. Such systems are often termed 'clustered nanoparticles' or 'nanoflowers' and consist of several smaller SPION constituents being in close contact thus forming a cluster. Due to the single magnetic cores being closer together or even in contact, magnetic dipolar interactions between the cores are increased. Furthermore, exchange interactions may be found increasing the inter-core interactions even further. The aggregation state has an influence, e.g., on the transverse relaxation time  $T_2$  in MRI [28, 29]. This effect has led to a new strategy of controlling aggregates or clusters to obtain a large degree of magnetic susceptibility and even long-term stability [30, 31].

The collective magnetic behaviour of clustered particles gives rise to macroscopic magnetic properties that differ from those expected for single-core particles. For example, despite the large size of the aggregates, they still show superparamagnetic behaviour. This then implies zero or a small remanent magnetization. Fig.1.1 compares the magnetization curves for single and clustered nanoparticles. While both systems exhibit similar superparamagnetic behaviour, the magnetization of the aggregated particles is significantly larger due to the cooperative interaction of their magnetic moments. The desired aggregates are characterized by coherent rotation of the superspins of the primary particles that constitute the cluster, i.e., the superspins of the primary particles inside the clusters rotate in unison. Some studies propose that this behaviour is related to the existence of exchange coupling among the cores, leading to a superferromagnetic state of the whole aggregate [32]. Consequently, expanding the detailed understanding of inter-core interactions within clusters is essential to optimize the magnetic performance in applications.

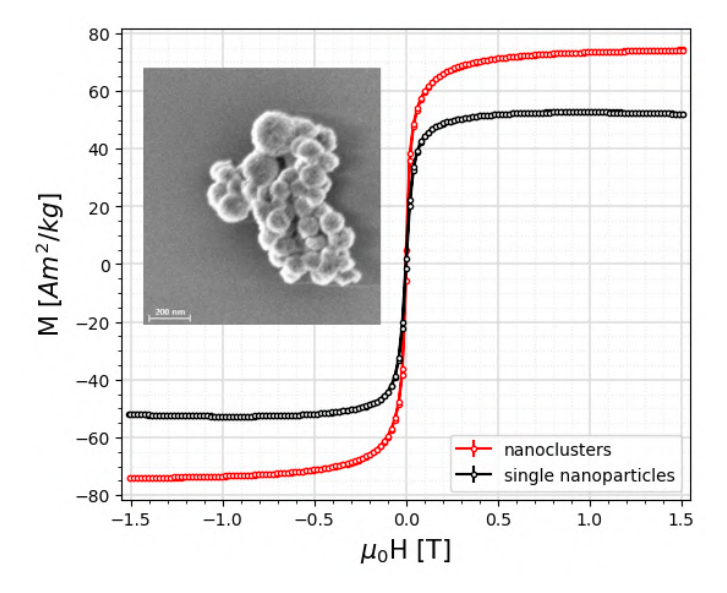


Figure 1.1: Comparison of magnetization curves for single nanoparticles and nanocluster aggregates. The data shown are from the same SPION citrate sample used in this study, while the single nanoparticles are commercial iron oxide nanoparticles (SPA10-10) from Ocean NanoTech (San Diego, USA). The SEM image of the SPION citrate sample is from Ref. [33].

The most commonly used iron oxide phases as magnetic cores of nanoparticles for biomedical applications are magnetite  $Fe_3O_4$  and maghemite  $\gamma-Fe_2O_3$  [34]. Due to the sensitivity of magnetite to oxidation, it is not easy to obtain pure magnetite as nanoparticles, often resulting in a mixture with maghemite [27]. Controlling the oxidation state of the iron oxide cores is crucial for medical applications, as it significantly impacts their functionality. For example, the oxidation of magnetite to maghemite reduces the SPION's saturation magnetization. Also, the magnetocrystalline anisotropy is affected. Consequently, the particles' efficiency and the results' reproducibility are altered [35]. Deliberate control of the oxidation state can hence lead to an increase of e.g. the heating delivery in magnetic hyperthermia applications [36]. Therefore, a systematic study of the impact of surfaces on core oxidation is essential not only for optimizing the synthesis of these materials, but also for the control of their magnetic properties for specific applications.

#### 1.2 The Aim of the Work

Numerous research studies have investigated the synthesis of magnetic clustered nanoparticles, the effects of various coatings, and the resulting physicochemical properties [37, 38, 39, 40]. However, their magnetic properties remain debated [41, 42]. In our study, we

have selected several coating agents, such as negatively charged citrate, positively charged APTES, and neutral hydrophilic polymer dextran, to stabilize the magnetically clustered nanoparticles and to control the oxidation properties of the iron oxide nanoparticles. The aim of our study is therefore to

- Investigate the effects of different coating agents on particle size, structural organization, and magnetic properties. We employed magnetometry combined with small-angle X-ray scattering (SAXS) and cryogenic transmission electron microscopy (cryo-TEM). Additionally, we utilized small-angle neutron scattering (SANS) to examine the magnetic structure of the clustered particles for the citrate-coated system.
- Study the oxidation stability of the particle-coating species from storage to the final product. We used both Mössbauer spectroscopy and magnetometry to be able to track the changes in Fe<sup>2+</sup> and Fe<sup>3+</sup> composition as a function of time for various coating types, determining the net magnetic properties and examining how fast this oxidation takes place and the ratio of the oxidized form.
- Employ micromagnetic simulations to understand the internal magnetic structure of iron oxide nanoparticle clusters.

## Chapter 2

## Theoretical Background

This chapter provides the essential theoretical framework necessary to understand the structural and magnetic properties of self-assembled superparamagnetic iron oxide nanoparticles. In section 2.1.3, we explore the various magnetic interactions present between the atomic magnetic moments in bulk materials, which lead to a variety of magnetic orders (section 2.1.4). We also investigate nanoparticle magnetism and the possibility of the existence of collective inter-particle superspin states depending on the strength of their interactions in section 2.1.6. Next, in section 2.2, we will discuss scattering theory. This section covers theoretical aspects of scattering phenomena, particularly focusing on small-angle X-ray and neutron scattering methods. These techniques are vital for characterizing the structural and magnetic properties of nanoparticles. In section 2.3, we introduce Mössbauer spectroscopy, a powerful technique for probing hyperfine interactions and providing insights into the local environments of atoms in materials. Finally, in section 2.4, we discuss micromagnetic simulations that are used to model magnetic systems. It is essential for the understanding of the dynamic spin behaviour within nanoparticles and their assemblies.

### 2.1 Magnetism

#### 2.1.1 Magnetic moments

In a classical model of an atom, magnetic moments arise from the circular motion of an electron around atomic nuclei. This motion is equivalent to a current flow I around a loop area  $\vec{dA}$ . This results in a magnetic moment given by  $d\vec{\mu} = Id\vec{A}$ , with the direction normal to the area of the loop (Fig.2.1(a)). However, for the correct discussion of atomic magnetic moments, a quantum mechanical description has to be employed. For a single electron atom, the magnetic moments originate firstly from the orbital angular momentum of the electron, given by  $\vec{l} = \vec{r} \times \vec{p}$ , where  $\vec{p}$  is the electron momentum and  $\vec{r}$  is the spatial position. Secondly, electrons exhibit an intrinsic magnetic moment  $\vec{\mu}_s$  which is associated

with its intrinsic spin angular momentum  $\vec{s}$  (Fig.2.1(b)). Hence, the orbital magnetic moment  $\vec{\mu}_l$ , the spin magnetic moment  $\vec{\mu}_s$  and the total angular momentum  $\vec{\mu}_i$  are

$$\vec{\mu}_{l} = -g_{L} \frac{\mu_{B}}{\hbar} \vec{l}$$

$$\vec{\mu}_{s} = -g_{S} \frac{\mu_{B}}{\hbar} \vec{s},$$

$$\vec{\mu}_{j} = -g_{J} \frac{\mu_{B}}{\hbar} \vec{j}$$

$$(2.1)$$

where  $\mu_B = 9.27 \times 10^{-24} {\rm Am}^2$  is the Bohr magneton,  $g_L = 1$  and  $g_S \approx 2$  represent the g-factors for the orbital and spin components, respectively. According to quantum mechanics, the component of orbital angular momentum along a fixed axes such as z-axes is  $m_l \hbar$ , and the magnitude of orbital angular momentum is  $\sqrt{l(l+1)}\hbar$  where l and  $m_l$  are the orbital quantum number and the corresponding magnetic quantum number, respectively. Hence, the component of  $\vec{\mu}_l$ , along the z-axis is given by

$$\mu_l^z = -\mu_B m_l$$
; with  $m_l = -l, -l+1, \dots, 0, \dots, l-1, l$ . (2.2)

Similarly the components of spin magnetic moment  $\vec{\mu}_s$  and of the total magnetic moment  $\vec{\mu}_j$  along the z-axis can be written as [43]

$$\mu_s^z \approx -2\mu_B m_s$$
; with  $m_s = \pm 1/2$ . (2.3)

$$\mu_j^z = -g_L \mu_B m_j; \text{ with } m_j = -j, -j+1, \dots, 0, \dots, j-1, j.$$
 (2.4)

where  $m_s$  is called the spin magnetic quantum number, while j represents total angular momentum quantum numbers, with  $m_j$  corresponding to the total angular momentum magnetic quantum number. The potential energy of an electron with a magnetic moment  $\vec{\mu}$  in a magnetic field  $\vec{B}$  is known as Zeeman energy

$$E_{\text{Zeem}} = -\vec{\mu} \cdot \vec{B} = -\mu B \cos(\theta), \qquad (2.5)$$

where  $\theta$  is the angle of the magnetic moments relative to the magnetic field. The torque is  $G = -\mu B \sin \theta$ , which lets the magnetic moment precess around the field direction.

For an atom with several electrons, the orbital and spin angular momenta are given by  $\vec{L} = \sum_i^N \vec{L_i}$ ,  $\vec{S} = \sum_i^N \vec{s_i}$ , where the summation extends over all electrons. The resulting  $\vec{L}$  and  $\vec{S}$  can be (in case of so-called LS coupling) coupled through the spin-orbital interaction to form the resulting total angular momentum  $\vec{J}$ 

$$\vec{J} = \vec{L} + \vec{S}. \tag{2.6}$$

However, for atoms with relatively large atomic number Z the j-j coupling scheme is dominating [44]. In this scheme, the orbital and spin angular momenta of each individual

electrons are first combined to form the total angular momentum as  $\vec{j}_i = \vec{l}_i + \vec{s}_i$ . The resulting angular momenta,  $\vec{j}_i$ , then interact to yield the total angular momentum of the atom as  $J = \sum_{i=1}^{N} \vec{j}_i$ . The Hamiltonian of spin-orbital coupling is given by

$$\mathcal{H} = \lambda \vec{L} \cdot \vec{S},\tag{2.7}$$

where  $\lambda$  is the spin-orbital coupling constant. Both the  $\vec{L}$  and  $\vec{S}$  precess around  $\vec{J}$ . Then the total magnetic moment of a atom is

$$\vec{\mu_{\text{tot}}} = \vec{\mu_L} + \vec{\mu_S} = -\frac{\mu_B}{\hbar}(\vec{L} + 2\vec{S}).$$
(2.8)

The  $\vec{\mu}_{\text{tot}}$  is directed along the vector  $(\vec{L} + 2\vec{S})$  but not along  $(\vec{J})$ . One should note that it is composed of a constant component which is the projection of  $\mu_{tot}$  on the direction of  $\vec{J}$  and a precessing component around the direction of  $\vec{J}$ . The total magnetic moment with a certain angular momentum J is then written as

$$\vec{\mu}_J = -g_J \frac{\mu_B}{\hbar} \vec{J},\tag{2.9}$$

where  $g_J$  represents the projection of  $\vec{\mu}_{tot}$  on  $\vec{J}$  so that

$$g_J = \frac{(\vec{L} + 2\vec{S}) \cdot \vec{J}}{J^2} = \frac{(\vec{J} + \vec{S}) \cdot \vec{J}}{J^2}.$$
 (2.10)

Since  $\vec{L} = \vec{J} - \vec{S}$ , so  $L^2 = J^2 + S^2 - 2\vec{J} \cdot \vec{S}$ , and hence

$$(\vec{J} + \vec{S}) \cdot \vec{J} = J^2 + \vec{S} \cdot \vec{J} = J^2 + (\frac{J^2 + S^2 - L^2}{2})$$
 (2.11)

Substituting in E.q 2.10 yields:

$$g_J = \left[1 + \frac{J^2 + S^2 - L^2}{2J^2}\right]. \tag{2.12}$$

Replacing  $J^2$ ,  $L^2$ , and  $S^2$  by their quantum mechanical values  $J(J+1)\hbar^2$ ,  $L(L+1)\hbar^2$ , and  $S(S+1)\hbar^2$  respectively, we obtain:

$$g_J = \left[1 + \frac{J(J+1) + S(S+1) - L(L+1)}{2J(J+1)}\right]. \tag{2.13}$$

In the context of an atom with total magnetic moment  $\vec{\mu}_J$  placed in a weak magnetic field  $\vec{B}$ , the Zeeman energy can also be formulated as: [43]

$$E_{\text{Zeem}} = -\vec{\mu} \cdot \vec{B} = g_J \frac{\mu_B}{\hbar} \vec{J} \cdot \vec{B}, \qquad (2.14)$$

when  $\vec{B}$  is applied along the z-axis i.e. defines the z-axis. The Zeeman energy becomes

 $g_J\mu_Bm_JB$ , where  $J_z=m_J\hbar$ . In the absence of a magnetic field, the energy levels associated with different  $m_J$  are degenerate. However, once a magnetic field is applied, this degeneracy is removed, leading to the splitting into (2J+1) discrete sublevels, and each sublevel corresponds to a specific value of the  $m_J$ .

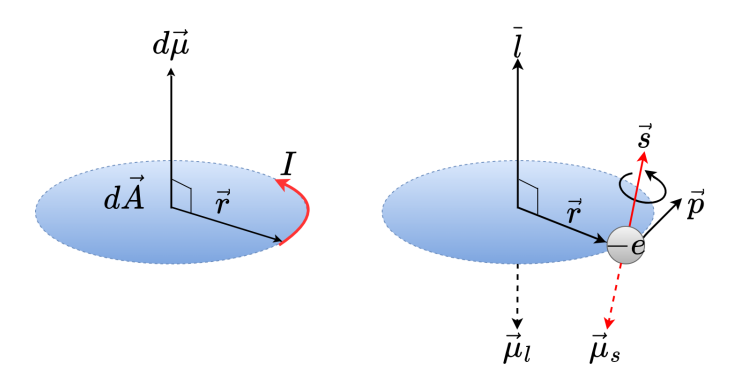


Figure 2.1: (a) Magnetic moments are generated by a current running round of the loop, (b) the magnetic moment  $\vec{\mu}_l$  and  $\vec{\mu}_s$  originate from the orbital angular momentum and the spin of an electron, respectively, with directions opposite to their angular momenta  $\vec{l}$  and  $\vec{s}$ .

#### 2.1.2 Magnetization

A solid typically consists of a large number ( $\sim 10^{23}$ ) of atoms each carrying a magnetic moment. One important quantity characterizing the macroscopic magnetic properties is defined as the sum of all magnetic moments divided by the volume V of the sample, i.e. the magnetization,

$$\vec{M} = \frac{1}{V} \sum_{i}^{N} \vec{\mu}_{i}.$$
 (2.15)

In free space, we define the magnetic field  $\vec{H}$  through the  $\vec{B} = \mu_0 \vec{H}$ , where  $\mu_0 = 4\pi \cdot 10^{-7}$  H/m is the magnetic permeability of vacuum and  $\vec{B}$  is called magnetic flux density. In a magnetic solid, the relation between  $\vec{B}$  and  $\vec{H}$  can be given by

$$\vec{B} = \mu_0(\vec{H} + \vec{M}). \tag{2.16}$$

Magnetic materials can be classified in terms of their magnetic susceptibility  $\chi$  which expresses the relationship between  $\vec{M}$  and the magnitude of  $\vec{H}$  as

$$\chi = \frac{\partial M}{\partial H},\tag{2.17}$$

where M has the unit A/m, being the same as the unit of H, which makes  $\chi$  a dimensionless quantity. Most materials are weakly magnetic and exhibit magnetism only in the presence of an applied field. They are classified as paramagnets when their susceptibility lies in the range of  $10^{-6}-10^{-1}$  or diamagnets when their susceptibility lies in the range of  $-10^{-6}-10^{-5}$ , respectively. However, several materials exhibit ordered magnetic states. The interaction between atomic magnetic moments can give rise to collective magnetism, i.e. spontaneous magnetization without the application of an external magnetic field. They typically have a large value of  $\chi$  and can be either ferromagnetic, antiferromagnetic, or ferrimagnetic. These magnetic types will be described in more detail in the next section 2.1.4.

#### 2.1.3 Collective magnetism

In magnetic solids, different types of magnetic interactions can exist between the atomic magnetic moments, allowing them to interact with each other. These can lead to various types of macroscopic magnetic properties of materials.

#### 2.1.3.1 Magnetic dipole interaction

Magnetic dipoles always interact with each other via long-range dipole-dipole interactions. The magnetic field generated by one magnetic dipole moment  $\vec{\mu}_1$  is given by [45]

$$\vec{B}(\mu_1, r) = \frac{\mu_0}{4\pi r^3} \left[ \frac{3}{r^2} (\vec{\mu}_1 \cdot \vec{r}) \cdot \vec{r} - \vec{\mu}_1 \right]. \tag{2.18}$$

The potential energy of the second magnetic dipole moment  $\vec{\mu}_2$  in the field created by the first moment at a distance r (Fig.2.2) is then

$$E_{\text{dip}} = -\vec{\mu}_2 \cdot \vec{B}(\mu_1, r) \tag{2.19}$$

$$E_{\text{dip}} = \frac{\mu_0}{4\pi r^3} \left[ \vec{\mu}_1 \cdot \vec{\mu}_2 - \frac{3}{r^2} (\vec{\mu}_1 \cdot \vec{r}) \cdot (\vec{\mu}_2 \cdot \vec{r}) \right]$$
 (2.20)

The classical dipole-dipole energy depends on the distance and relative orientation of the two moments, which leads to a strongly anisotropic type of interaction. The dipole energy may be written as follows

$$E_{\rm dip} = -\frac{\mu_0 \mu_1 \mu_2}{4\pi r^3} \left[ 2\cos\theta_1 \cos\theta_2 - \sin\theta_1 \sin\theta_2 \right]. \tag{2.21}$$

where  $\theta_1$  and  $\theta_2$  are the angle between the  $\vec{\mu}_1$  and  $\vec{\mu}_2$  relative to  $\vec{r}$ . For simplicity, we consider two dipoles that are aligned parallel and antiparallel to each other. In the case of magnetic moments oriented parallel to each other, where the angle  $\theta_1 = \theta_2 = 90^{\circ}$ , the energy is expressed as  $(E = \frac{\mu_0 \mu_1 \mu_2}{4\pi r^3})$ , indicating a repulsive interaction. If, on the other hand, the dipoles are aligned anti-parallel, where the angle  $\theta_1 = 90^{\circ}$  and e  $\theta_2 = -90^{\circ}$ , the

energy is given by  $(E = -\frac{\mu_0 \mu_1 \mu_2}{4\pi r^3})$ , which indicates an attractive interaction. Usually, dipole interactions are too weak to explain magnetic order at room temperature in regular solids. E.g. for atomic spins with  $\mu = 1\mu_B$  separated by  $|\vec{r}| = 1$  Å, the magnetic dipole energy is 54  $\mu$ eV, which corresponds to 0.6 K. Therefore, thermal fluctuations can destroy the alignment of the dipolar coupled moments at ambient temperature. In contrast, magnetic dipole interactions are pronounced in fine particles with large magnetic moments about  $10^3 - 10^5 \mu_B$  and separations in the order of nm. Then, the magnetic dipolar energy corresponds to several tens or even hundreds of Kelvin and can hence have a significant influence during the self-assembly or aggregation of particles.

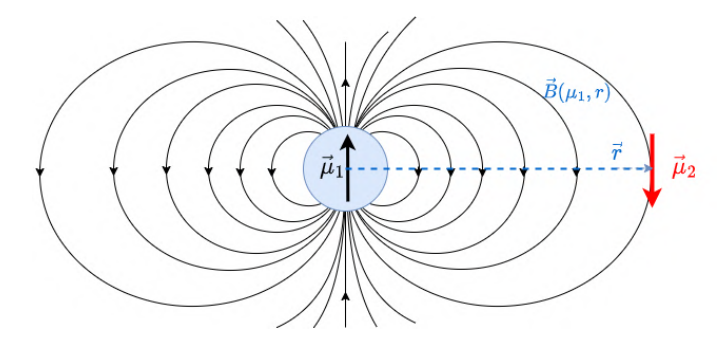


Figure 2.2: Schematic of a magnetic dipole moment  $\vec{\mu}_1$  with the corresponding dipolar field, and a second moment  $\vec{\mu}_2$  located at distance r.

#### 2.1.3.2 Exchange interactions

The exchange interaction is a short-range magnetic interaction that allows the nearest magnetic moments to interact strongly (in the order of 1 eV  $\approx$  10000 K). This interaction can be explained involving the exchange of two electrons due to both the Pauli principle and Coulomb interactions. According to the Pauli exclusion principle, when two electrons occupy the same orbital, they must have different spin quantum numbers ( $S=\pm\frac{1}{2}$ ), whereas, if they have the same spin quantum numbers, they cannot occupy the same orbital. In a solid, the atomic orbitals overlap, and so if two electrons on neighboring atoms occupy the same state, they must take opposite spins. On the other hand, the Coulomb interaction tends to maximize a distance between two electrons regardless of their spins, so that eventually ferromagnetic coupling is favored. However, this effect is small when the electrons are well separated, leading to an increase in kinetic energy. If the benefit of Coulomb energy can not overcome the increase in the kinetic energy, two electrons stay in the same state with an antiparallel alignment.

When considering two electrons located at spatial positions  $\vec{r}_1$  and  $\vec{r}_2$  with the wave functions  $\psi_a(\vec{r}_1)$  and  $\psi_b(\vec{r}_2)$ , it is important to recognize that the electrons are identical fermions. Since they are indistinguishable particles, their combined wave function must be totally antisymmetric. The total wave function is given by the combination of a spatial part and a spin part. The spatial wave function  $\psi(\vec{r}_1, \vec{r}_2)$  can be written as

$$\psi_{\pm}(\vec{r}_1, \vec{r}_2) = \frac{1}{\sqrt{2}} [\psi_a(\vec{r}_1)\psi_b(\vec{r}_2) \pm \psi_b(\vec{r}_2)\psi_a(\vec{r}_1)]. \tag{2.22}$$

The spatial wave function is symmetric (+) or antisymmetric (-). For spin functions, there are two possible configurations for coupled spins: an antisymmetric singlet state with S=0 and a symmetric triple state with S=1. The quantum number  $m_s$  of the composite system is just  $m_{s1} + m_{s2}$ , where both  $m_{s1}$  and  $m_{s2}$  take only value of  $\pm 1/2$ . Then the states of the coupling two spins are written in the notation  $|Sm_s\rangle$ 

$$X_T : \left\{ \begin{array}{ll} |11\rangle & =\uparrow\uparrow\\ |10\rangle & =\frac{1}{\sqrt{2}}(\uparrow\downarrow+\downarrow\uparrow)\\ |1-1\rangle & =\downarrow\downarrow \end{array} \right\} \quad S = 1 \text{ (triplet)}. \tag{2.23}$$

$$X_S; \left\{ |00\rangle = \frac{1}{\sqrt{2}} (\uparrow \downarrow - \downarrow \uparrow) \right\} \quad S = 0 \text{ (singlet)}.$$
 (2.24)

In conclusion, the antisymmetric total wave function can be written as

$$\psi_T = \psi_-(\vec{r})X_T \tag{2.25}$$

$$\psi_S = \psi_+(\vec{r})X_S \tag{2.26}$$

The energies of the singlet and triplet states amount to:

$$E_S = \int \psi_S^* \mathcal{H} \psi_S \, \mathrm{d}V_1 \, \mathrm{d}V_2 \tag{2.27}$$

$$E_T = \int \psi_T^* \mathcal{H} \psi_T \, \mathrm{d}V_1 \, \mathrm{d}V_2 \tag{2.28}$$

The energy difference between the singlet and triplet state is defined as the exchange constant 2J, which depends on the orientation of the neighboring spins as follows:

$$J = \frac{E_S - E_T}{2} = \int \psi_a^*(\vec{r}_1) \,\psi_b^*(\vec{r}_2) \,\mathcal{H}\psi_a(\vec{r}_2) \,\psi_b(\vec{r}_1) \,\mathrm{d}V_1 \,\mathrm{d}V_2. \tag{2.29}$$

If J>0, the triplet state S=1 is favored, and two spins prefer to align parallel. If J<0, the singlet state is favored, and two spins align antiparallel. Since the energy difference between the single and triple states depends on the orientations of the spins, the spin-dependent term of Hamiltonian coupling of two electrons is written as

$$\mathcal{H} = -2J\vec{S}_1 \cdot \vec{S}_2 \tag{2.30}$$

Considering a spin-spin coupling, the total spin is  $\vec{S} = \vec{S}_1 + \vec{S}_2$ , after taking the square one obtains the product  $\vec{S}_1 \cdot \vec{S}_2 = \frac{1}{2}[(S)^2 - S_1^2 - S_2^2]$ . Both electrons have a spin  $\frac{1}{2}\hbar$  with eigenvalue of  $S_1^2 = S_2^2 = \frac{3}{4}\hbar$ , and according to whether the spin quantum number S is 0 or

1, the eigenvalues of the coupled spins  $\vec{S}_1 \cdot \vec{S}_2$  are  $-\frac{3}{4}\hbar$  or  $+\frac{1}{4}\hbar$ , respectively.

In a solid, the Hamiltonian generalized to a sum over all pairs of atoms on lattice sites can then be written

$$\mathcal{H} = -2\sum_{i>j} J_{i,j} \vec{S}_i \cdot \vec{S}_j \tag{2.31}$$

with  $J_{i,j}$  being the exchange constant between atom i and atom j. The summation  $\sum_{i>j}$  ensures that the sum is limited to pairs of spins  $\vec{S}_i$  and  $\vec{S}_j$  only once. If the electrons belong to different atoms, direct exchange can occur when magnetic orbitals of neighboring atoms have significant overlap, but this is rare in oxides due to the separation of atomic orbitals. In most cases, indirect exchange interactions take place in oxides.

In the case of indirect exchange mediated by a non-magnetic atom, in oxides usually oxygen, it is known as super-exchange interaction. The exchange interaction J is on the order of  $2t^2/U$ , with t as the hopping integral and U as the energy cost of making an excited state (Coulomb energy). A larger exchange interaction results from electrons hopping from a magnetic cation to a non-magnetic anion and then to the next cation. However, the strength of this exchange interaction depends on the degree of overlap of orbitals, and thus, super-exchange interaction depends on the angle of cation-ion-cation bonds, leading to various magnetic orders. An example is shown for two iron (Fe<sup>3+</sup>) cations within an octahedral structure, with oxygen ions  $(O^{2-})$  centered at the bonds. In an octahedral structure, the five d-orbitals split into  $t_{2g}$ -orbitals  $(d_{xy}, d_{yz}, and d_{zx})$  with lower energy and  $e_q$ -orbitals  $(d_{x^2-y^2}, \text{ and } d_{z^2})$  with higher energy. Fe<sup>3+</sup> has a configuration of  $3d^5$ with five unpaired electrons. The oxygen would have two p electrons in the neutral state. The hopping of electrons from Fe<sup>3+</sup> via O<sup>2-</sup> to the next Fe<sup>3+</sup> leads to antiferromagnetic coupling, thus lowering the kinetic energy and lowering the energy of the system. In contrast, ferromagnetic coupling is limited to interactions between the oxygen and only one magnetic cation because two electrons cannot occupy the same orbital in the same quantum state. Consequently, this ferromagnetic coupling requires more energy than the antiferromagnetic coupling. The configuration cation-anion-cation can align with two bond angles, i.e. 90° and 180° (Fig.2.3). If the angle is 180°, the cation-anion-cation shares the same main axes, in which, i.e., the  $d_{x^2-y^2}$  orbitals in both cations couple with  $2P_x$ orbitals, resulting in antiferromagnetic coupling. In the case of 90°, the main axes of the two cations are perpendicular, leading to partial overlap of the  $d_{x^2-y^2}$  orbital with  $2P_x$ from one cation and both  $d_{x^2-y^2}$  and  $2P_y$  from the other cation, resulting in ferromagnetic coupling. These qualitative descriptions of magnetic ordering can be further understood through the Goodenough-Kanamori-Anderson (GKA) rule [46].

In magnetite (Fe<sub>3</sub>O<sub>4</sub>), cations include Fe<sup>3+</sup> and Fe<sup>2+</sup> located on the octahedral A site and only Fe<sup>3+</sup> on the tetrahedral B site. The Fe<sup>3+</sup> cations at both A and B sites can interact antiferromagnetically through an intermediate angle of 125°. The Fe<sup>3+</sup> cations on the A site can exhibit ferromagnetic coupling at the angle of 90° between the two cations (see Fig.2.4(a)). If the magnetic ions are in a mixed valence state, ferromagnetic interaction among the ions is possible, known as **double exchange**. In this interaction,

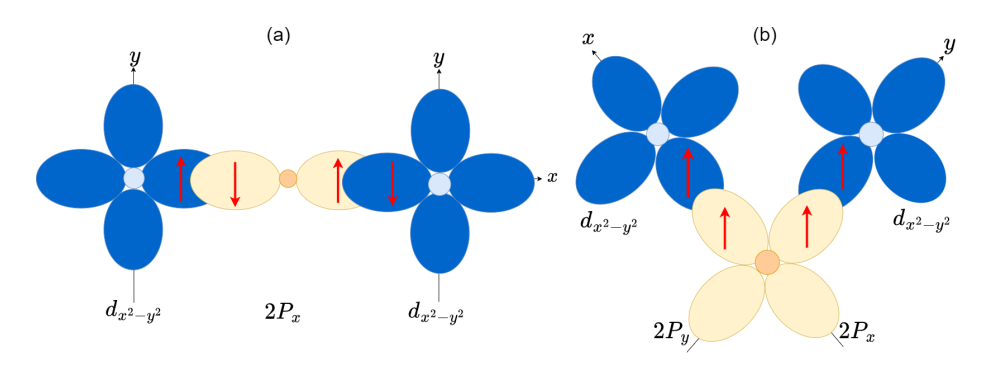


Figure 2.3: Schematic representation of the configuration Fe<sup>3+</sup>-O<sup>2-</sup>-Fe<sup>3+</sup> at (a) 180°, (b) 90°.

the additional electron of  $Fe^{2+}$  at the A site can transition to the  $Fe^{3+}$  at the same site only if the spins of these ions are parallel to each other (see Fig.2.4(b)).

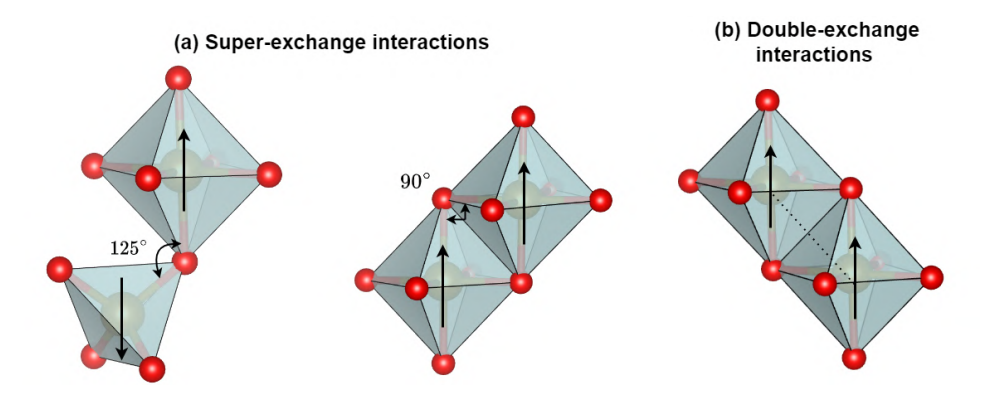


Figure 2.4: Schematic representation of the super-exchange and double-exchange interactions in Fe<sub>3</sub>O<sub>4</sub>. (a) Super-exchange interactions showing the antiferromagnetic coupling between the Fe<sup>3+</sup> cations on the A and B sites at 125°, along with weak ferromagnetic coupling between the Fe<sup>3+</sup> cations on the A sites at 90°. (b) Double-exchange interactions illustrating the ferromagnetic coupling between Fe<sup>3+</sup> and Fe<sup>2+</sup> cations on the A sites.

#### 2.1.4 Magnetic properties of matter

In the previous section, different types of magnetic interactions between the magnetic moments in a solid were introduced. In this section, we will examine the different types of magnetism, the origin of this different behaviour, and the resulting magnetic properties. We will start with diamagnetism and paramagnetism in materials in which the magnetic moments do not interact with each other. We then discuss materials that have strong interactions among their magnetic moments, which have influenced these interactions in a range of magnetic order states, including ferromagnetism, antiferromagnetism, and ferrimagnetism.

#### 2.1.4.1 Diamagnetism and paramagnetism

To study the different types of magnetism, it is necessary to first look at the response of an atom with one electron in a magnetic field. The Hamiltonian is then the sum of kinetic and potential energies:

$$\mathcal{H}_0 = -\frac{\hbar^2}{2m_e} \nabla^2 - \frac{Ze^2}{4\pi\epsilon_0 r}$$
 (2.32)

with the momentum  $\vec{p}=i\hbar\nabla$ , where  $m_e$  is the electron mass, e is the electron negative charge, Z is the atomic number, r is the distance from the nucleus to the electron, and  $\epsilon_0$  is the permittivity of vacuum. In the presence of a magnetic field, the momentum is replaced with  $\vec{p} \to \vec{p} + e\vec{A}(r)$ , where  $\vec{A}(r)$  is the vector potential [44, 47]. The Hamiltonian is also modified by adding an additional term due to the interaction of spin  $\vec{S}$  with the magnetic field  $\vec{B}$ . The resulting Hamiltonian can be written as

$$\mathcal{H} = \left(\frac{[p^2 + 2e\vec{p} \cdot \vec{A(r)} + e^2 \vec{A^2(r)}]}{2m_e} - \frac{Ze^2}{4\pi\epsilon_0 r}\right) + g_s \frac{\mu_B}{\hbar} \vec{S} \cdot \vec{B} \quad . \tag{2.33}$$

Assuming  $\vec{B} = Be_z$ , the vector potential  $\vec{A}$  can have the value  $\vec{A}(r) = \frac{1}{2}B(-y, x, 0)$ . The Z component of the angular momentum is then  $L_z = xp_y - yp_x$ , and hence we obtain:

$$\mathcal{H} = \frac{p^2}{2m_e} - \frac{Ze^2}{4\pi\epsilon_0 r} + \frac{\mu_B}{\hbar} \vec{B}(\vec{L}_z + 2\vec{S}_z) + \frac{e^2 B^2}{8m_e} (x^2 + y^2)$$

$$= \mathcal{H}_0 + \mathcal{H}_{\text{para}} + \mathcal{H}_{\text{dia}}.$$
(2.34)

The first term is the original Hamiltonian, the second term is the paramagnetic contribution and the last term the diamagnetic contribution.

#### Diamagnetism

Diamagnetism is a type of magnetism present in all materials. The magnetization in the presence of a magnetic field is calculated as  $\vec{M} = -\frac{1}{\mu_0 V} \left( \frac{\partial E}{\partial \vec{H}} \right)$  and susceptibility  $\chi = \frac{\partial M}{\partial H}$  [48]. Hence:

$$\vec{M} = -\frac{ne^2\vec{B}\langle r^2\rangle}{6m_e},\tag{2.35}$$

$$\chi = -\frac{ne^2\mu_0\langle r^2\rangle}{6m_e},\tag{2.36}$$

where n is the number of atoms per unit volume. The diamagnetic susceptibility has a negative value, and thus these materials produce a magnetization in a direction opposite to the applied field. It is also temperature independent.

#### Paramagnetism

Although we mentioned above, all materials exhibit diamagnetism, this can be negligible compared to a positive magnetic susceptibility arising from the magnetic moments of unpaired electrons aligning in the direction of the magnetic field. This is known as paramagnetism. One should note that in solid state magnetism, the term paramagnetism denotes, on the one hand, systems with zero or negligible interactions between the magnetic moments and, on the other hand, the unordered magnetic phase. I.e. a ferromagnet shows a phase transition at a critical temperature to the paramagnetic phase. However, both definitions share the same macroscopic properties, i.e. in the absence of an applied field the orientations of magnetic moments are stochastically random leading to canceling out and a zero net magnetization. When an external magnetic field is applied, the magnetic moments align in the direction of the field to show a net macroscopic magnetization. Thermal fluctuations counteract the alignment. The energy of magnetic moments  $\vec{\mu}_J$  in an external field  $\vec{B} = Be_z$  is given by  $E = g_J \mu_B m_J B$ . With the partition function  $Z = \sum_{m_J=-J}^J e^{-E\frac{1}{k_B T}} = \sum_{m_J} e^{-\mu_B g_J m_J B\frac{1}{k_B T}}$ , the general behaviour of the magnetization can be shown as follows

$$M(B,T) = M_s B_J(y), (2.37)$$

$$B_J(y) = \frac{2J+1}{2J} \coth\left(\frac{2J+1}{2J}y\right) - \frac{1}{2J} \coth\left(\frac{y}{2J}\right),\tag{2.38}$$

$$y = \frac{\mu_B g_J B}{k_B T},\tag{2.39}$$

where the saturation magnetization is  $M_s = ng_J\mu_B J$  with n - the number of magnetic moments per unit volume, and  $B_J(y)$  - the Brillouin function for a certain value of J. In the limit of  $J \to \infty$ , the Brillouin function is equal to the Langevin function [49].

At low temperatures (and hence  $y \ll 1$ ), the Brillouin function takes the form

$$\lim_{y \ll 1} B_J(y) = \frac{J+1}{3J}y \tag{2.40}$$

so that the susceptibility  $\chi$  becomes

$$\chi = \frac{n\mu_0 g_J^2 \mu_B^2 J(J+1)}{3k_B T} = \frac{n\mu_0 \mu_{\text{eff}}^2}{3k_B T} = \frac{C}{T},$$
(2.41)

where  $\mu_{\text{eff}} = g_J \mu_B [J(J+1)]^{1/2}$  is the effective moment and  $C = n \mu_0 g_J^2 \mu_B^2 J(J+1)/3k_B$  is the Curie constant. Thus, the dependence of the susceptibility on the inverse temperature is known as the Curie law. The magnetic susceptibility is positive in contrast to the diamagnetic effect.

#### 2.1.4.2 Ferromagnetism

Ferromagnets are characterized macroscopically by a spontaneous magnetization in the absence of an external magnetic field and microscopically by a long-range order in which the magnetic moments are aligned in parallel. This arises from a positive exchange interaction. The ferromagnetic order vanishes above a critical temperature called the Curie temperature  $T_c$ . Above  $T_c$ , these materials behave paramagnetically. The origin of spontaneous magnetization was investigated by P. Weiss [50]. He assumed that in ferromagnets, each magnetic moment is subject to an internal field or so-called molecular field  $\vec{H}_{\rm mf} = \lambda \vec{M}$ , which is generated by neighboring moments, and  $\lambda \approx 10^4$  is a material constant and represents the strength of the molecular field as a function of magnetization. The magnetization of ferromagnets can then be formally treated as a simple paramagnet by replacing the magnetic field  $\vec{H}$  with  $\vec{H} + \vec{H}_{\rm mf}$  [51]. At low temperatures, the molecular field is responsible for the spontaneous magnetic order, and the susceptibility can then be expressed as

$$\chi = \frac{M}{H + H_{\rm mf}} = \frac{C}{T}.\tag{2.42}$$

Thus we obtain:

$$\vec{M} = \frac{C\vec{H}}{T - C\lambda}.\tag{2.43}$$

The susceptibility is then given by:

$$\chi = \frac{C}{T - \theta},\tag{2.44}$$

where  $\theta = C\lambda$  is the Curie–Weiss temperature, which is directly related to the molecular field coefficient  $\lambda$ . If  $\theta = 0$ , the material is paramagnetic, while if  $\theta > 0$  the material is ferromagnetic with a value of  $\theta$  approximately equal to  $T_C$ . Above  $T_C$ , thermal fluctuations overcome the magnetic order leading to a susceptibility macroscopically similar to the one of a paramagnet.

#### 2.1.4.3 Antiferromagnetism

In antiferromagnets, the molecular field is negative, making it favorable for the nearest neighbor magnetic moments to be oriented antiparallel to one another. The system can be considered as consisting of two interpenetrating sublattices, such that the nearest neighbors are always in the other sublattice. Within each sublattice, the magnetic moments are aligned parallel to one another, while an antiparallel orientation is found between the two sublattices. Since the total magnetic moment and the magnetization direction of both sublattices are equal and opposite  $(M = |M_-| = |M_+|)$ , the resulting magnetization is zero in the absence of a magnetic field. The magnetic order disappears at temperatures above a transition temperature known as the Néel temperature  $T_N$ . In this regime, the susceptibility exhibits a temperature dependence similar to that of a paramagnet, where the material obeys the Curie–Weiss law but with a negative value of  $\theta < 0$ , and it is expected  $\theta = -T_N$ :

$$\chi \propto \frac{1}{T - \theta}.\tag{2.45}$$

Experimentally, however,  $|\theta| \neq T_N$ . This difference arises mainly from the assumption that the molecular field on one sublattice depends only on the magnetization of the other sublattice.

#### 2.1.4.4 Ferrimagnetism

Ferrimagnetism can be treated as an antiferromagnetic system in which the two sublattices are not equivalent, resulting in different molecular fields acting on each sublattice. Magnitudes of the magnetic moments in this case are unequal, such that  $|M_-| \neq |M_+|$  and the total magnetic moment of the sublattices will not cancel out, leading to a non-zero net magnetization of the system. Such materials obey the Curie-Weiss law but with a negative value of  $\theta$  at high temperatures. Fig. 2.5 represents magnetic spin ordering and the variation of the inverse susceptibility as a function of temperature for paramagnetic, ferromagnetic, antiferromagnetic, and ferrimagnetic systems.

#### 2.1.5 Magnetic anisotropy

The term "magnetic anisotropy" describes the fact that the magnetic properties depend on the direction of the measurement. The magnetic anisotropy affects the magnetization and hence the hysteresis curve behaviour. This directional dependence creates easy and hard directions. In the easy directions, it is easier to magnetize the material compared to the hard directions, where the total magnetization of the system will prefer to lie along the easy axis. This section will discuss the contributions to magnetic anisotropy: magnetocrystalline anisotropy, shape anisotropy, and surface anisotropy.

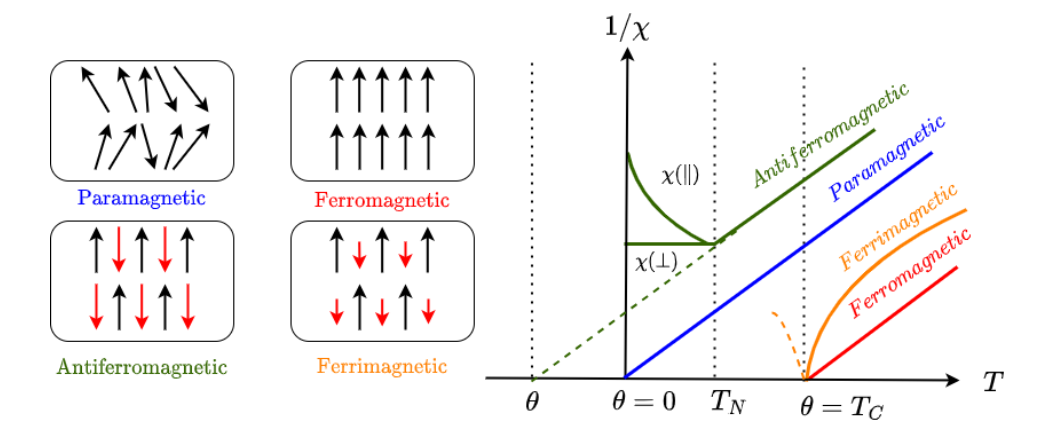


Figure 2.5: Magnetic spin ordering and inverse susceptibility as a function of temperature for paramagnetic, ferromagnetic, antiferromagnetic, and ferrimagnetic systems. This figure is adapted from Ref. [52].

#### Magnetocrystalline anisotropy

The magnetization M-H curves of single crystals of the 3d ferromagnetic elements such as iron (Fe) and cobalt (Co), show that for certain crystallographic directions, it is easy to saturate the crystal magnetically, while along others, it is harder. These directions are called easy axes and hard axes of magnetization, respectively. There is an energy cost for magnetization aligned away from an easy axis, toward a hard axis [48].

Co with hexagonal crystal, i.e., exhibits a so-called uniaxial anisotropy with one easy axis. Then the energy depends on the angle to the easy axis as:

$$E_u = V K_1 \sin^2 \theta, \tag{2.46}$$

where V is the crystal volume,  $\theta$  is the angle between the  $\vec{M}$  and the easy axis,  $K_1$  is the anisotropy constant. Because these constants have a positive value  $K_1 > 0$ , the energy is minimized when  $\vec{M}$  is aligned along its easy axis. This alignment typically occurs at angles of  $\theta = 0$  or  $\theta = \pi$ , which represent the easy axis directions. For the hard direction, typically the value of the angle is  $\theta = \pi/2$ . In a cubic system, e.g. Fe, the anisotropy energy is described by [53]

$$E_{\text{cub}} = V K_{c1}(\alpha_1^2 \alpha_2^2 + \alpha_2^2 \alpha_3^2 + \alpha_3^2 \alpha_1^2) + V K_{c2}(\alpha_1^2 \alpha_2^2 \alpha_3^2 + ..),$$
 (2.47)

where  $\alpha_i = \cos \theta_i$ , and  $\theta_i$  is the angle between the magnetization and a cubic crystal axes, and  $K_{c1}$  and  $K_{c2}$  is the first and second order anisotropy constant, respectively.  $K_{c2}$  and other higher-order terms can usually be neglected [54]. The sign of  $K_{c1}$  determines the

easy axes for magnetization. For  $K_{c1} > 0$ , the easy axis for the magnetization is oriented along  $\langle 100 \rangle$ , while for  $K_{c1} < 0$  the easy axis for the magnetization is aligned along  $\langle 111 \rangle$ . The magnetocrystalline anisotropy constant is temperature dependent, and the typical values at a room temperature are  $K_{c1} = -13 \text{ kJ/m}^3$  and  $K_{c2} = -3 \text{ kJ/m}^3$  in the case of Fe resulting in cubic diagonal  $\langle 111 \rangle$  being the easy magnetization axes [55].

The magnetocrystalline anisotropy arises from the interplay of spin-orbit interaction and crystal symmetry. This is because the shape of the electron orbitals and hence their overlap are linked to the crystallographic structure.

#### Shape anisotropy

Shape anisotropy is, as the name implies, related to the shape of the objects and originates from the demagnetizing field. The magnetization prefers to align at these directions which reduce the demagnetizing field (or stray fields outside the sample). Fig. 2.6 provides an example of the an ellipsoidal particle. When the ellipsoidal object is magnetized in the direction of the short axes, a larger stray field outside the particle occurs and vice versa. As a consequence, elongated particles typically exhibit a preferred magnetic orientation along the long symmetry axis. The energy of the demagnetization field is given by

$$E_{\text{demag}} = -\frac{\mu_0}{2} \int_V \vec{M} \cdot \vec{H}_d \, dV,$$
 (2.48)

where  $\vec{H}_d$  is the demagnetization field inside the solid and its magnitude is proportional to the magnetization via

$$\vec{H}_d = -\mathcal{N} \cdot \vec{M} = -\begin{pmatrix} \mathcal{N}_x & 0 & 0\\ 0 & \mathcal{N}_y & 0\\ 0 & 0 & \mathcal{N}_z \end{pmatrix} \cdot \vec{M}, \tag{2.49}$$

where  $\mathcal{N}$  is a demagnetization tensor, which is represented by a  $3 \times 3$  matrix. Here the simplified case of a diagonalized tensor is presented. In general the demagnetization tensor can have also non-diagonal elements. The sum of the diagonal elements, the demagnetization factors,  $\mathcal{N}_x$ ,  $\mathcal{N}_y$ ,  $\mathcal{N}_z$ , satisfy  $\mathcal{N}_x + \mathcal{N}_y + \mathcal{N}_z = 1$ . In a spherically shaped structure, all components of the demagnetization factor are equal, with  $\mathcal{N}_x = \mathcal{N}_x = \mathcal{N}_x = 1/3$ , resulting that the demagnetization energy is isotropic. This in turn means that the contribution of shape anisotropy is zero. However, for a prolate ellipsoid, the demagnetization energy is anisotropic and thus the shape anisotropy favors the alignment of the magnetization along the long symmetry axis [56].

#### Surface anisotropy

Surface anisotropy is caused by the breaking of crystallographic symmetry and reduced coordination, as well as broken exchange bonds of atoms on the surface of nanoparticles. These factors contribute to the phenomenon known as the surface canting effect, in which surface spins align in directions that deviate from those determined by the

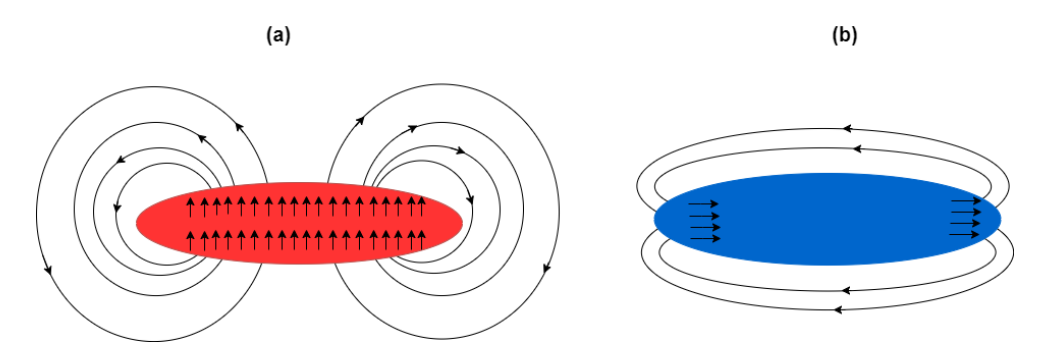


Figure 2.6: Sketch of the stray field of a bar magnet resulting from the distribution of magnetic poles on its surface. In (a), the magnetic moments are pointed normally to the surface, resulting in a larger stray field compared to (b), where the magnetic moments are aligned along the longitudinal axis (the preferred axes), leading to a reduced stray field.

internal magnetocrystalline anisotropy. In addition, defects could contribute to both surface and internal spin canting. The disorder on the surface also has an impact on the saturation magnetization. The magnetic nanoparticles are treated as a core-shell model, consistent with a core of magnetically coupled spins, usually with a ferromagnetic spin order, surrounded by a shell with a disordered spin order.

Due to the spin canting observed in magnetic nanoparticles, the effective  $K_{\text{eff}}$  magnetic anisotropy differs from that of the corresponding bulk material. The  $K_{\text{eff}}$  can be expressed as

$$K_{\text{eff}} = K_V + \frac{6}{D}K_S,$$
 (2.50)

where D is the diameter of the nanoparticle,  $K_V$  is the volume anisotropy, and  $K_S$  is surface anisotropy. The effective anisotropy of a small particle increases as its diameter decreases, as it is proportional to the 1/D.

#### 2.1.6 Nanoparticle magnetism

#### 2.1.6.1 Single domain particles

The magnetization in ferromagnetic or ferrimagnetic materials tends to break into magnetic domains in order to minimize the magnetic stray field energy  $(E_{\rm MS})$ . In each domain, the absolute value of the magnetization is approximately equal to the saturation value, but the directions of the magnetization vector between domains varies. Common are orientations of 45°, 90° or 180° of domain magnetizations relative to each other. In competition to the reduction of stray field energy by forming domains is the energy cost of domain walls. Within the domain wall, the magnetization vector rotates from one anisotropy to another, leading to an increase in the exchange energy  $(E_{\rm ex})$  and of the magnetic anisotropy

energy ( $E_{\text{MCA}}$ ), as both tend to align the spins along one of the anisotropy directions. In equilibrium a stable magnetic domain structure is obtained due to the balance between the cost of domain wall energy ( $E_{\text{ex}}$  and  $E_{\text{MCA}}$ ) and the gain in reduction of the stray field energy ( $E_{\text{MS}}$ ).

When the size of the system is reduced to below a critical threshold the energy cost for the presence of domain walls outweighs the energy gain from reducing the stray field (demagnetization) energy. Below this threshold only a single magnetic domain is then energetically stable. This result can be easily seen from the fact that the energy to form a domain wall with areal energy density  $\sigma_{\rm DW}$ , is proportional to  $R^2$ , where R is the radius of the particle. However, the demagnetization energy scales as  $R^3$ . In detail, one finds for the critical radius  $R_c$  below which the single-domain state is favorable and assuming a ferromagnetic sphere [57]:

$$R_c \approx 9 \frac{\sigma_{\rm DW}}{\mu_0 M_s^2} \approx 9\pi \frac{\sqrt{AK}}{\mu_0 M_s^2},\tag{2.51}$$

where  $A = \frac{nJS^2}{a}$  is the exchange constant, a is the lattice constant, n is the number of atoms in the unit cell, J is the exchange coupling constant, K is anisotropy constant, and  $M_s$  is the saturation magnetization. The concrete value of  $R_c$  depends on the material, but it is usually in the order of tens of nanometers. For example, the critical diameter for Fe<sub>3</sub>O<sub>4</sub> is about 49 nm [19].

Stoner–Wohlfarth (SW) Model is a model used to estimate the equilibrium state of the orientation of the magnetic moment of a nanoparticle in an external magnetic field  $(H_{\rm ext})$  and includes an effective uniaxial anisotropy of the particle  $(K_{\rm eff})$  [58, 59]. In the framework of this model one further assumes that there is only one single magnetic domain and that the magnetic reversal occurs by a coherent rotation, i.e. in which spins rotate in unison. For the case of a prolate ellipsoidal-shaped particle with Zeeman energy  $(E_{\rm Zeem})$  and one effective uniaxial anisotropy term  $(E_{\rm anis})$ , the total energy is [57, 58]

$$E_{\text{tot}} = E_{\text{anis}} + E_{\text{Zeem}}$$
  
=  $K_{\text{eff}} V \sin^2(\alpha) - \mu_0 M_s V H_{\text{ext}} \cos(\theta - \alpha),$  (2.52)

where V is the volume of the particle,  $\theta$  and  $\alpha$  are the angles between the external field and the magnetization vector and magnetization vector to the anisotropy easy axis (see Fig. 2.7(a)), respectively. Effective anisotropy means here that both magnetocrystalline and shape anisotropy are combined to one single effective contribution. For the case of two independent directions of magnetocrystalline and shape anisotropy two independent anisotropy terms and an additional angle need to be introduced. Such an extended model is usually not considered in the literature.

By minimizing the total energy  $E_{\rm tot}$ , the equilibrium direction of the magnetization vector is determined depending on the strength of the applied field and its direction relative to the anisotropy easy axis. The  $E_{\rm anis}$  is  $\propto \sin^2(\theta)$  with two degenerate minima at  $\alpha = 0^{\circ}$  and  $180^{\circ}$ , which are called easy axes in which the magnetization is directed along one of the two

2.1. Magnetism 22

energetically favored magnetization orientations. The necessary applied field to rotate the magnetization from the positive easy direction to the negative one is equal to  $2K_{\rm eff}/\mu_0 M_s$ , which is called the anisotropy field  $H_K$ . Fig. 2.7(b) shows the dependence of the energy on the direction of magnetization for a series of constant values of h= normalized field  $=H_{\rm ext}/H_K$ , where the direction of the external applied field  $H_{\rm ext}$  is at  $\theta=180^\circ$  relative to one easy axis. Starting with h=0, the two degenerate energy minima exist and the magnetization aligns preferentially along one of these easy axes. As h increases, the two energy values at the minima are not equal, and the degeneracy is removed. For h=1, only the energy minimum at  $\alpha=180^\circ$  remains, and the magnetization jumps to the lowest minimum in the applied field direction regardless of its initial orientation.

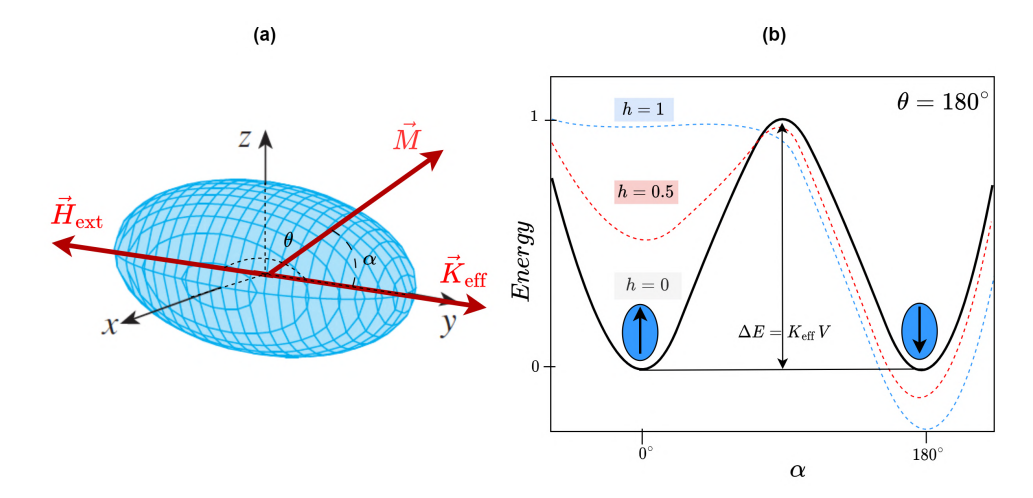


Figure 2.7: (a) Ellipsoidal particle with an effective uniaxial anisotropy constant  $K_{\text{eff}}$  along the easy axis (y-axis), in the presence of an external magnetic field  $H_{\text{ext}}$  with  $\alpha$  the angle between the magnetization and the anisotropy axis,  $\theta$  the angle between the anisotropy axis and the external magnetic field. (b) Energy change of the system as a function of parameter h ( $h = \frac{H_{\text{ext}}}{H_K}$  with  $H_K$  being the anisotropy field) [51].

#### 2.1.6.2 Superparamagnetism

Superparamagnetism (SPM) often appears in ferromagnetic or ferrimagnetic nanoparticles, typically in the size range from few nanometers to few tens of nanometers, depending on the material. Such nanoparticles are often in a magnetic single-domain state, as outlined above. If, in addition, the magnetization reversal occurs solely by a coherent rotation of particle magnetic moments, then it is possible to consider the entire nanoparticle as one giant macrospin which is then referred to as a superspin[60].

As shown in the SW model above, a single-domain particle displays in zero magnetic field

2.1. Magnetism 23

two energy minima separated by an energy barrier  $\Delta E = K_{\rm eff}V$ . In the limit  $k_BT \ll K_{\rm eff}V$ , the superspins cannot switch spontaneously. The system then behaves like a permanent ferromagnet (or ferrimagnet). Upon reducing the anisotropy barrier, e.g. by reducing the size of the particle, thermal energy can be sufficient to allow stochastic reversals of the superspin direction. Once it reaches  $k_BT \approx KV$  or above, the dynamics of superspins show a crossover to so-called unblocked SPM [61].

In the unblocked SPM state the field-dependent magnetization can be described by the Langevin model of atomic paramagnetism, with the difference that large magnetic moments are extracted from a fit [62, 63]. Typical superspin moments are in the order of  $1000\mu_B$ . The magnetization is given by the Langevin function as

$$M(H,T) = nmL(x), (2.53)$$

$$L(x) = \coth(x) - \frac{1}{x}, \ x = \frac{\mu_0 mH}{k_B T},$$
 (2.54)

where  $k_B$  is Boltzmann constant, n is the number of particles, and m is the particle magnetic moment. In this model, the anisotropy energy is neglected. A real single-domain particle typically exhibits anisotropic energy contributions such as shape anisotropy, magnetocrystalline anisotropy, and surface anisotropy. However, when the particle size is relatively small, the anisotropy energy becomes smaller than the thermal energy. The particle magnetic moments start to fluctuate, leading to a crossover to an unblocked superparamagnetic state. The relaxation of magnetization of these particles can be described by an Arrhenius-type law [64, 63]:

$$\tau_{Neel} = \tau_0 \exp\left(\frac{\Delta E}{k_B T}\right) = \tau_0 \exp\left(\frac{K_{\text{eff}} V}{k_B T}\right),$$
(2.55)

where  $\tau_0$  is the elementary spin flip attempt time of about  $10^{-9} - 10^{-13}s$ . This mechanism is dominant in small particles and when particles are not free to rotate, i.e. in frozen suspensions.

Because of the specific measurement time window,  $\tau_M$ , characteristic for each measurement technique, one observes a blocked superparamagnetic state if  $\tau_M$  is small compared to  $\tau_{Neel}$ , and conversely, an unblocked state if  $\tau_M \gg \tau_{Neel}$ . This crossover from a blocked to an unblocked state occurs at the so-called blocking temperature,  $T_B$ , which is hence defined as the temperature at which  $\tau_M = \tau_{Neel}$ :

$$T_B = \frac{K_{\text{eff}}V}{k_B\Phi}, \quad \Phi = \ln\left(\frac{\tau_M}{\tau_0}\right).$$
 (2.56)

Since the blocking temperature,  $T_B$ , is inversely proportional to the parameter  $\Phi$ , "slow" techniques with large measurement time windows, i.e., SQUID magnetometers with  $\tau_M$  of 10-100 s ( $\Phi \approx 30$ ), lead to relatively small blocking temperatures. In contrast, "fast" techniques with small time windows, e.g. Mössbauer spectroscopy with  $\tau_M$  of  $10^{-9}$ s ( $\Phi \approx 5$ ), lead to relatively larger blocking temperatures.

Experimentally, the  $T_B$  can be determined from the peak in the zero-field-cooled (ZFC)

2.1. Magnetism 24

magnetization curve. The ZFC curve is obtained by first cooling the sample from above its blocking temperature without applying an external magnetic field to low temperatures and then recording the magnetization upon heating in a small external field. This peak also serves as an indicator of the particle size distribution. Since different particle sizes imply a range of different anisotropy energy barriers ( $E=K_{\rm eff}V$ ) and thus different  $T_B$  values, this leads to a broadening of the peak. Another qualitative assessment of the particle size distribution can be made using the temperature difference between the peak position of the ZFC curve and the splitting temperature between the zero-field-cooled (ZFC) and Field cooled (FC) curves. The FC magnetization curve is obtained during cooling the sample in the presence of a magnetic field. A system in which the splitting temperature is much higher than  $T_B$  indicates a large particle size distribution.

#### 2.1.6.3 Collective superspin states

The superparamagnetic state of magnetic nanoparticles is characterized by the lack of inter-particle interactions. However, with increasing concentration of particles, the magnetic inter-particle interactions become non-negligible. For large enough interactions, a collective state becomes possible [65]. One case is the so-called superspin glass (SSG) state, which is found in systems with large dipolar inter-particle interactions and randomness in the particle positions or anisotropy axes orientations [66, 67]. The SSG state is then found below a critical glass freezing temperature,  $T_g$ , which is the order of the dipolar coupling energy. The  $T_g$  increases with the increase of coupling strength [68]. At larger concentrations of magnetic particles, also ferromagnetically or antiferromagnetically oriented order of superspins can be observed. Particle arrangements with ferromagnetic superspin order were termed superferromagnetic (SFM) systems [61].

SSG behaviour can be identified by various experimental procedures such as ZFC/FC magnetization curves and AC susceptibility. In the latter, the shift of peak temperature  $T_g$  as a function of AC frequency is analyzed [42]. Both SPM and SSG samples typically exhibit a peak in the ZFC curve, but SSG systems often display a decrease in the FC curve upon cooling. Magnetic inter-particle interaction leads to a broadening of the ZFC peak and a shift to larger temperatures due to the extension of the relaxation towards longer times. Thus, the magnetic relaxation significantly differs from that of the noninteracting particles. The corresponding transition temperature  $(T_g)$  is smaller than the blocking temperature of the individual nanoparticles. Consequently, the collective order is overshadowed by SPM blocking behaviour [19].

A clearer way to distinguish an SSG system from an SPM or weakly interacting SPM system is using the memory effect detected in ZFC curve [68, 69]. At high temperatures above the  $T_B$ , thermal fluctuations dominate the magnetic behaviour, causing spins to act independently. However, as the temperature decreases below  $T_B$ , these independent spins slow down and group into correlated units known as domains or droplets, e.g. in which the randomness of spin sites is frozen and only the spin orientation can vary. Further cooling towards the glass transition temperature  $(T_g)$  results in a reduction of fluctuations within these clusters, which causes them to grow and form long-range correlations among

spins. At  $T_g$ , the system is quenched into random but highly correlated orientations. At temperatures below  $T_g$ , the SSG system has the chaotic nature of the magnetic state, meaning a small change in temperature results in a completely different spin arrangement. This new configuration can be approached only gradually over time. This slow evolution forms the basis for observing the so-called memory effect during the aging process [61]. To investigate the memory effect, a standard ZFC curve is measured first. Then, a similar measurement is performed, but this time, the cooling process stops at a temperature below the SSG system. After this stop, the sample is further cooled to very low temperatures, and the magnetization is then recorded while heating in the same magnetic field that was used for the first ZFC measurement. When the standard ZFC curve is compared to the curve with the stop, a peak is expected at the stop temperature. This peak shows the memory effect, i.e. the system remembers the temperature at which it stopped during cooling without a magnetic field.

Relaxation times of strongly coupled superspins tend to be longer compared to noninteracting SPM particles. The relaxation time is given by a power law as following

$$\tau = \tau_0 \left(\frac{T}{T_g} - 1\right)^{-z\nu},\tag{2.57}$$

where  $\tau_0$  is the relaxation time of individual particle moment, and  $z\nu$  is dynamic critical exponent. Above  $T_g$ , it is possible to relate the relaxation time to the correlation length as  $\tau \propto \xi^z$ , where  $\nu$  is the critical exponent of the correlation length,  $\xi = \left(\frac{T}{T_g} - 1\right)^{-\nu}$ .

## 2.2 Scattering theory

#### 2.2.1 Basics of scattering

The scattering of an X-ray photon or a neutron by a sample involves a change in momentum  $\vec{P}$  and energy E. In the scattering process, incident and scattered plane waves are described by wave vectors  $\vec{k}_i$  and  $\vec{k}_f$ , respectively. The momentum transfer can be expressed as:

$$\vec{P} = \hbar(\vec{k}_f - \vec{k}_i) = \hbar \vec{Q},\tag{2.58}$$

where  $\hbar = \frac{h}{2\pi}$  is the Planck constant and  $\vec{Q}$  is the scattering vector. The incident wave vector  $\vec{k}_i$  is related to the energy of incident particles as  $E_i = \frac{\hbar^2 k i^2}{2m}$ , with  $k_i = \frac{2\pi}{\lambda}$ , where m and  $\lambda$  are the mass and wavelength of incident particles, respectively. If we assume that the energy of scattered particles  $E_f$  does not change, then the wave vector of the incident and scattered particle are equal,  $|\vec{k}i| = |\vec{k}f|$ . The latter case is known as an elastic scattering. Otherwise, one has the case of inelastic scattering. The magnitude of the elastic scattering wave vector  $\vec{Q}$  can be calculated from the wavelength  $\lambda$  and the scattering angle  $2\theta$  between  $\vec{k}_i$  and  $\vec{k}_f$  as follows:

$$Q_{\text{elastic}} = |\vec{Q}| = \sqrt{2k^2(1 - \cos(2\theta))} = k\sqrt{2(1 - \cos^2(\frac{\theta}{2}) + \sin^2(\frac{\theta}{2}))} = \frac{4\pi\sin(\theta)}{\lambda}.$$
 (2.59)

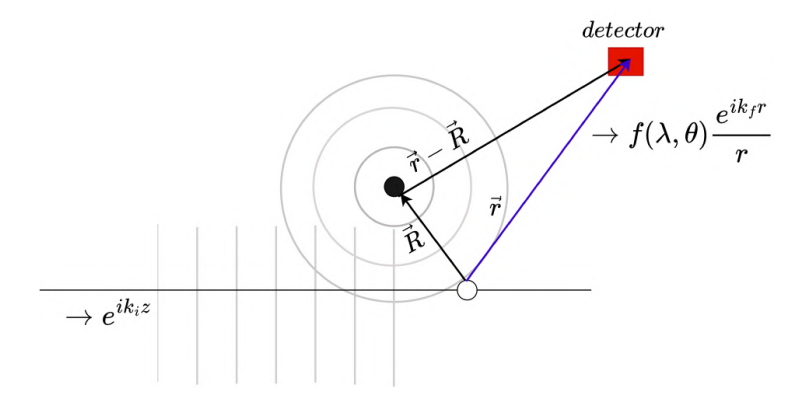


Figure 2.8: An incoming plane wave is scattered by a single fixed scatterer located at position  $\vec{R}$ . This interaction generates an outgoing isotropic scattered wave, which is detected at the position  $\vec{r}$  on the detector. In the far-field approximation, it is assumed  $|\vec{r}| \gg |\vec{R}|$ .

We consider an incident wave traveling along the Z direction characterized by a wave function  $\Psi_i = \psi_0 e^{ik_i z}$ , where  $\psi_0$  represents the amplitude of the incident wave. This wave is then scattered by a point-like fixed scatterer located at position  $\vec{R}$ , which is defined by a non-zero interaction potential  $V(r) \neq 0$ , producing an outgoing isotropic spherical wave (see Fig. 2.8). For the scattering of an incident wave, i.e. a neutron with a wavelength typically in the Årange that is larger as the ensemble of nuclei ( $\approx 10^{-4}$  Å), it is natural to replace the nuclei by a point-like scatterer. The scattered wave can then be described by the first Born approximation, which is valid under the condition that the potential is weak when calculating the amplitude of the scattered wave. In this approximation, the scattered wave can be expressed as follows:

$$\Psi_f = \Psi_i f(\lambda, \theta) \frac{e^{i\vec{k}_f \cdot (\vec{r} - \vec{R})}}{|\vec{r} - \vec{R}|}, \tag{2.60}$$

where  $f(\lambda, \theta)$  known as a scattering amplitude. For  $|\vec{r}| \gg |\vec{R}|$ , a far-field approximation can be applied, and thus  $|\vec{r} - \vec{R}| \approx |\vec{r}| = r$ . If we next consider a three-dimensional assembly of scatterers at position  $\vec{R}_j$ , the scattered wave of a certain atom labeled as  $[\Psi_f]_j$ , is given by

$$[\Psi_f]_j = \psi_0 e^{ik_i R_j} f_j(\lambda, \theta) \frac{e^{ik_f \cdot (\vec{r} - \vec{R}_j)}}{r}. \tag{2.61}$$

The superposition of scattered waves from all N atoms is written as

$$\Psi_{f} = \frac{\psi_{0}}{r} \sum_{j=1}^{N} f_{j}(\lambda, \theta) e^{i(\vec{k_{i}} - \vec{k_{f}}) \cdot \vec{R_{j}}} e^{i\vec{k_{f}} \cdot \vec{r}}$$

$$= \frac{\psi_{0}}{r} e^{i\vec{k_{f}} \cdot \vec{r}} \sum_{j=1}^{N} f_{j}(\lambda, \theta) e^{-i\vec{Q} \cdot \vec{R_{j}}}.$$
(2.62)

However, in scattering experiments, the scattered waves  $\Psi_f$  is not measurable. Instead, only the scattered intensity is determined as

$$I(\vec{Q}) \propto |\psi_f(\vec{Q})|^2 = \frac{\Phi}{r^2} \left| \sum_{j=1}^{N} f_j e^{-i\vec{Q} \cdot \vec{R}_j} \right|^2,$$
 (2.63)

where  $\Phi = |\psi_0|^2$  is the incident flux. Since  $|e^{i\vec{k_f}\cdot\vec{r}}|^2 = 1$ , it means the phase information is lost, and a reconstruction of the structure of the sample via a simple Fourier transform is impossible [70].

#### Differential scattering cross-section

In scattering experiments, the scattered waves are deflected into a detector with a small area  $\partial A$ , in the direction of  $2\theta$  and  $\phi$ . The detector can only cover a small solid angle of  $\delta\Omega = \frac{\delta A}{r^2}$ . Here, the  $\delta A$  represents the area of the detector, and  $\vec{r}$  is the distance from the scattering source to the detector. The probability of the scattering event per unit of time can be expressed as

$$R(2\theta,\phi) = \left| \psi(\vec{Q}) \right|^2 \delta A = \Phi \delta \Omega \left| \sum_{j=1}^{N} f_j e^{-i\vec{Q} \cdot \vec{R}_j} \right|^2.$$
 (2.64)

In this equation, the incident flux  $\Phi$  is usually specified by the number of incident particles per unit area per second (with SI units of m<sup>-2</sup> s<sup>-1</sup>). The probability of the scattering event detected within a defined solid angle leads to the concept of the differential scattering cross-section  $\frac{d\sigma}{d\Omega}(\vec{Q})$ , which is given by

$$\frac{d\sigma}{d\Omega}(\vec{Q}) = \frac{R(2\theta, \phi)}{\Phi d\Omega} = \left| \sum_{j}^{N} f_{j} e^{-i\vec{Q} \cdot \vec{R}_{j}} \right|^{2}.$$
 (2.65)

The total scattering cross-section is obtained by the integration of the probability of all the scattering angles

$$\sigma_{\text{total}} = \int_0^{4\pi} \left(\frac{d\sigma}{d\Omega}\right) d\Omega \tag{2.66}$$

The microscopic scattering cross section  $\sigma$  characterizes interactions with single isotopes, has SI units of m<sup>2</sup>, and the common area unit used in scattering physics is the barn, which is equivalent to  $10^{-28}$  m<sup>2</sup>.

#### Coherent and incoherent scattering cross-section

The scattering amplitude  $f(\lambda, \theta)$  is used to describe interaction potential depending on the size and shape of the scatterers. For point-like scatterers  $f(\lambda, \theta) = -b$ , where b is the scattering length that describes the scattering probability. The magnitude of b determines the strength of the interaction between neutron and nucleus, whereas its sign indicates whether the interaction with nucleus is attractive (positive b) or repulsive (negative b). For the assembly of atoms with scattering lengths  $b_j$ , averaging becomes essential for samples containing a natural mixture of isotopes or various nuclear spin states for a given atom. The differential scattering cross-section can then be expressed as:

$$\frac{d\sigma}{d\Omega}(\vec{Q}) = \left\langle \sum_{i=1}^{N} \sum_{j=1}^{N} b_{i} b_{j} e^{i\vec{Q} \cdot (\vec{r}_{i} - \vec{r}_{j})} \right\rangle 
= \left\langle b \right\rangle^{2} \sum_{i,j}^{N} \left\langle e^{i\vec{Q} \cdot (\vec{r}_{i} - \vec{r}_{j})} \right\rangle + \sum_{i}^{N} \Delta b_{i}^{2} = \left[ \frac{d\sigma}{d\Omega} \right]_{\text{coh}} + \left[ \frac{d\sigma}{d\Omega} \right]_{\text{inc}}.$$
(2.67)

With  $\langle b \rangle^2$  as the square average scattering length, and  $\Delta b_i^2 = (b_i - \langle b \rangle)^2$  [71]. Consequently, the scattering cross-section consists of a coherent and an incoherent scattering contribution. Coherent scattering corresponds to an interference of the scattering resulting from an average scattering length, where  $b_i = b_i$ , while incoherent scattering is due to deviation from the average scattering length  $b_i \neq b_j$ . Coherent scattering contains phase information. Hence, the structural arrangement of scatters can be determined. In contrast, incoherent scattering contains no phase information and is directly proportional to the number of atoms N, providing a constant background. The total coherent scattering cross-section for an element composed of various isotopes can be expressed as  $\sigma_{\rm coh} = 4\pi \langle b \rangle^2$ , while the incoherent scattering cross-section, which accounts for the variations in scattering lengths among the different isotopes, is given by  $\sigma_{\text{inc}} = 4\pi (\sum_{i=1}^{N} (b_i - \langle b \rangle)^2$ . Most elements have a significant coherent scattering cross-section, but there are a few prominent examples of isotope incoherence, such as nickel, as well as nuclear spin incoherence, which is significant for light elements, such as hydrogen. As a result, a large background is observed. The coherent scattering is negligible for single isotopes or zero nuclear spins such as <sup>4</sup>He and <sup>36</sup>Ar, which is used in the experiment to eliminate or minimize incoherent scattering.

#### 2.2.2 Electron, X-ray, and Neutron interaction with matter

The basic scattering of various probes such as X-rays, neutrons, and electrons is the same since all these particles have a wave description [72]. However, they have differences in scattering behaviour arising from the different physical properties such as charge, spin, and energy.

The neutrons are particles with zero electrical charge and interact directly with the atomic nuclei via the short-range nuclear force or via dipole-dipole interaction with atoms due to non-zero spin S=1/2. The lack of charge results in a large penetration depth, allowing

massive bulk samples to be investigated. Additionally, neutrons have magnetic moments, along with their ability to penetrate deeply into a variety of materials, making them ideal for investigating the internal magnetic structures of bulk condensed matter. The energy of free neutrons is calculated by

$$E = \frac{\hbar^2 k^2}{2m_n},\tag{2.68}$$

where  $m_n$  is the mass of neutrons, and  $k = \frac{2\pi}{\lambda}$ . A neutron with a momentum P linked with the de Broglie wavelength  $\lambda$  through the equation:

$$\lambda = \frac{h}{n}.\tag{2.69}$$

X-ray photons, on the other hand, have zero charge and zero mass and interact with the electron shells of atoms via electromagnetic forces. The energy of the X-rays can be linked with accelerating voltage V and wavelength through

$$E = eV = \frac{hc}{\lambda},\tag{2.70}$$

where e is the charge of the electron, and c is the speed of light.

Electrons are negatively charged particles interacting strongly with matter via Coulomb interactions with the electron shell or the positively charged nuclei. Hence, the penetration of electrons in matter is less due to the repulsion of orbital electrons. Thus, either absorption or multiple scattering effects can not be neglected. This makes electrons useful for studying the surface layers of materials.

It is useful to compare the strength of scattering for X-rays, electrons, and neutrons. The scattering strength of these particles by an atom is quantified as the scattering length. For X-rays, the scattering length for each element is proportional to the number of electrons (the atomic size). Therefore, there is a weak contrast between light and heavy elements, such as hydrogen and metal ions. For electrons, scattering cross-sections are several orders of magnitude larger—typically by a factor of several million [73]. In contrast, for neutrons, the scattering length is dependent on the nuclear structure. This results in a significant contrast among different hydrogen isotopes as well as between hydrogen and heavy elements. Another advantage is that non-destructive techniques allow us to look inside large or complex objects.

Finally, both neutrons and X-rays are used to study the magnetic structure at the atomic level. Since X-rays are electromagnetic radiation and some electrons in magnetic materials carry a magnetic moment due to spin and angular momentum, it is only natural to expect a magnetic interaction in addition to the purely charge-based interactions. However, magnetic X-ray scattering is several orders of magnitude weaker than charge scattering. In contrast, neutrons can interact with the magnetic induction within the sample, resulting in magnetic scattering that is comparable in strength to nuclear scattering (E.q 4.5). By controlling the neutron spin, researchers can also perform polarized scattering experiments that allow the separation of the scattering terms.

#### 2.2.3 Diffraction

Diffraction is typically a coherent elastic scattering method that yields information about the atomic structure. In the case of the crystalline samples, diffraction geometry is described by the concept of the reciprocal lattice. Each point in the reciprocal space is related to a set of planes in real space.  $\vec{G}$  is the reciprocal lattice vector and is perpendicular to the planes with Miller indices (hkl). Its magnitude  $|\vec{G}| = \frac{2\pi}{d_{\rm hkl}}$ , where d is the spacing between adjacent parallel planes. In the diffraction experiment, the scattering vector  $\vec{Q}$  satisfies Laue condition  $\vec{Q} = \vec{G}$ , which is equivalent to Bragg's law of diffraction [74]:

$$\vec{k}_f = \vec{G} + \vec{k}_i. \tag{2.71}$$

By taking the square of the above equation

$$k_f^2 = G^2 + 2\vec{G} \cdot \vec{k}_i + k_i^2. (2.72)$$

Then, the diffraction condition is written as  $2(-\vec{G}) \cdot \vec{k_i} = G^2$  because  $|\vec{k_i}| = |\vec{k_f}|$ . To show its equivalent to the Bragg condition, the  $2(-\vec{G}) \cdot \vec{k_i} = G^2$  can be written as

$$G = 2k_i \sin(\theta) \to \frac{2\pi}{d} n = 2\frac{2\pi}{\lambda} \sin(\theta) \to n\lambda = 2d\sin(\theta),$$
 (2.73)

where  $\theta$  is the angle between the incident beam and the crystal plane and n is an integer. In real space, the position of an atom i in the unit cell is given by  $r_i = x_i \vec{a}_1 + y_i \vec{a}_2 + z_i \vec{a}_3$ , where coefficients  $x_i$ ,  $y_i$ , and  $z_i$  are the atomic coordination, and  $\vec{a}_1$ ,  $\vec{a}_2$ , and  $\vec{a}_3$  are three basic vectors of the unit cell. The reciprocal lattice vector is given by

$$\vec{G} = h\vec{b}_1 + k\vec{b}_2 + l\vec{b}_3. \tag{2.74}$$

The corresponding basis vector of the reciprocal lattice is given by

$$\vec{b}_1 = 2\pi \frac{\vec{a}_2 \times \vec{a}_3}{\vec{a}_1 \cdot (\vec{a}_2 \times \vec{a}_3)},\tag{2.75}$$

$$\vec{b}_2 = 2\pi \frac{\vec{a}_3 \times \vec{a}_1}{\vec{a}_1 \cdot (\vec{a}_2 \times \vec{a}_3)},\tag{2.76}$$

$$\vec{b}_3 = 2\pi \frac{\vec{a}_1 \times \vec{a}_2}{\vec{a}_1 \cdot (\vec{a}_2 \times \vec{a}_3)}.$$
 (2.77)

Here, the basic vector in reciprocal space satisfies the condition of  $\vec{a}_i \cdot \vec{b}_j = 2\pi \delta_{ij}$ , where  $\delta_{ij} = 1$  in case i = j and 0 in the case  $i \neq j$ . The structure factor is introduced in the case of periodically ordered structures, such as crystallites. It describes atomic coordination, and it is written as

$$F(\vec{Q}) = \sum_{j} f_{j}(\vec{Q}) \exp^{(i\vec{G}.\vec{r}_{j})}$$

$$= \sum_{j} f_{j}(\vec{Q}) \exp^{2\pi i(hx_{j} + ky_{j} + lz_{j})}.$$
(2.78)

$$= \sum_{j} f_{j}(\vec{Q}) \exp^{2\pi i(hx_{j} + ky_{j} + lz_{j})}. \tag{2.79}$$

The structure factor contains the complete structural information, including the atomic coordination by  $(x_i, y_i, \text{ and } z_i)$ , and site occupations by observing the absence of the structure factor. For example, the body-centered cubic arrangement has two lattice points, one at the origin with a coordination (0,0,0) and the other point at the canter with a coordination (1/2, 1/2, 1/2). Substituting these values for  $r_j$  into Eq. 2.79 gives

$$F(\vec{Q}) = f(1 + \exp^{\pi i(h+k+l)}). \tag{2.80}$$

Since h, k, and l are integer, we can define the sum h + k + l = N. The exponential function can then take values: +1 for N even, and -1 for N odd in E.q 2.80. Therefore:

$$F = 2f$$
 if  $(h + k + l)$  is even.  
 $F = 0$  if  $(h + k + l)$  is odd.

#### 2.2.4Small-angle scattering

The objects studied in the thesis are in the range of 1 to 100 nm. To resolve such large structures, small scattering angles or small scattering vector Q is required (i.e.  $\frac{2\pi}{Q} > 1$  nm). This requirement for small angles can also be expressed in the Bragg equation. With a wavelength  $\lambda = 0.7$  nm, which is larger than the atomic distance of ca. 0.15 nm, it becomes essential to use small angles to observe a Bragg peak and hence study the structure on the nanoscale. This method is known as small-angle scattering (SAS), i.e., for neutron or X-ray beams, it is termed small-angle neutron scattering (SANS) or small-angle X-ray scattering (SAXS), respectively. To achieve experimentally small scattering angles, the detector must be positioned at large distances away from the sample.

For large structures such as nanoparticles, the atomic scattering lengths are not relevant anymore to describe the scattering phenomena. Instead, it is more appropriate to use a continuous coherent scattering length per unit volume, known as scattering length density  $\rho(r)$ , defined as:

$$\rho(\vec{r}) = \frac{\sum_{i=1}^{N} b_i}{dV}.$$
(2.81)

where  $b_i$  is the atomic scattering length of the (i)-th atom, and N is the total number of scattering length in the volume dV. This allows to exchange of the sum in the differential cross-section equation in E.q 2.65 by integrals as follows

$$\sum_{i=1}^{N} f_j \dots \to \int_{V} \rho(\vec{r}) dV \tag{2.82}$$

The differential cross section is normalized to the particle volume, that gives the single scattering intensity with the unit [cm<sup>-1</sup>]:

$$\frac{d\Sigma}{d\Omega} = \frac{1}{V} \frac{d\sigma}{d\Omega}(\vec{Q}) = \frac{1}{V} \left| \int_{V} \rho(\vec{R}) e^{(i\vec{Q} \cdot \vec{r})} dV \right|^{2}. \tag{2.83}$$

#### Diluted system

For dilute nanoparticles dispersed in a solvent, the differential cross-section has no structure factor and is proportional to the contrast. The contrast represents the difference in scattering length density (SLD) between particles and solvent, given by  $\Delta \rho = \rho_p(\vec{r}) - \rho_s(\vec{r})$ . However, most solvents do not have strong coherent scattering intensity for the Q range covered by the SAS, it is often more convenient to write  $\Delta \rho = \rho_p(\vec{r}) - \rho_s$ . The scattering amplitude of a single sphere particle in a solvent is written as:

$$\begin{split} F(\vec{Q}) &= \int \rho(\vec{r}) e^{i\vec{Q}\cdot\vec{r}} d^3r \\ &= \int_{V_{\text{particle}}} \rho(\vec{r}) e^{i\vec{Q}\cdot\vec{r}} d^3r + \int_{V^* = V - V_{\text{particle}}} \rho(\vec{r}) e^{i\vec{Q}\cdot\vec{r}} d^3r \\ &= \int_{V_{\text{particle}}} \rho_p(\vec{r}) e^{i\vec{Q}\cdot\vec{r}} d^3r + \int_{V^*} \rho_{H_2O} e^{i\vec{Q}\cdot\vec{r}} d^3r \\ &= \int_{V_{\text{particle}}} \rho_p(\vec{r}) e^{i\vec{Q}\cdot\vec{r}} d^3r + \left( \int_V \rho_{H_2O} e^{i\vec{Q}\cdot\vec{r}} d^3r - \int_{V_{\text{particle}}} \rho_{H_2O} e^{i\vec{Q}\cdot\vec{r}} d^3r \right) \\ &= \int_{V_{\text{particle}}} \rho_p(\vec{r}) e^{i\vec{Q}\cdot\vec{r}} d^3r - \int_{V_{\text{particle}}} \rho_{H_2O} e^{i\vec{Q}\cdot\vec{r}} d^3r + \int_V \rho_{H_2O} e^{i\vec{Q}\cdot\vec{r}} d^3r \\ &\approx \Delta \rho V \frac{3[\sin(QR) - QR\cos(QR)]}{(QR)^3} \\ &\approx \Delta \rho V \frac{3j_1(QR)}{QR} \end{split}$$

where  $j_1(x)$  is the first-order spherical Bessel function.

When N particles dispersed in a solvent are oriented randomly, the scattering pattern is isotropic, and the scattering function depends only on the absolute value of the wave vector  $|\vec{Q}|$ . The differential scattering cross-section is then given by:

$$\begin{split} \frac{d\Sigma}{d\Omega}(Q) &= \frac{N}{V} |F(Q)|^2 = n \left| \Delta \rho V \frac{3j_1(QR)}{QR} \right|^2 \\ &= n \Delta \rho^2 V^2 \left[ \frac{3j_1(QR)}{QR} \right]^2 \\ &= n \Delta \rho^2 V^2 \tilde{P}(Q), \end{split} \tag{2.84}$$

where  $n = \frac{N}{V}$  is the particle number density, and  $\tilde{P}(Q)$  is the normalized form factor. The condition  $\frac{d\Sigma}{d\Omega}(Q)|_{Q=0}$  is equal  $n\Delta\rho^2V^2$ . The form factor is then  $P(Q) = n\Delta\rho^2V^2\tilde{P}(Q)$ . The scattering intensity at small Q of dilute colloids can describe by the Guinier scattering law as follows [75]

$$\frac{d\Sigma}{d\Omega}(Q \to 0) = \frac{d\Sigma}{d\Omega}(0) \cdot \exp\left[-\frac{1}{3}Q^2R_g^2\right],\tag{2.85}$$

where  $R_g$  is the radius of gyration of the particle. It is defined as the average squared distance between any point of the particle and its center of mass [76]. The Guinier law model provides a method to determine particle sizes using SAS data and is valid in the limit  $QR_g \leq 1.3$ . By plotting SAS data as  $\ln[I(Q)]$  against  $Q^2$  and fitting the slope of the line at low Q the radius of gyration  $R_g$  can be determined. Using the  $R_g$ , one can further calculate relevant particle sizes. For example, the radius of a sphere is  $R = \sqrt{5/3}R_g$ , and the length of a thin rod is  $L = \sqrt{12}R_g$ .

When the particles have not the same sizes, E.q 2.84 takes the following form:

$$\frac{d\Sigma}{d\Omega}(Q) = n \int_{V} D(R)F(Q,R)e^{(i\vec{Q}\cdot\vec{R})}dR, \qquad (2.86)$$

where D(R) is a particle size distribution function (for instance, lognormal distribution). It is notable that when there is a larger particle size variation, the scattering profile smears out and shows less oscillation at high Q.

#### Concentrated system

For a concentrated nanoparticle dispersion in a solvent, there will be correlations between the particle centers of mass and thus modulations of the scattering intensity. To account for this modulation, the structure factor S(Q) is introduced in the general formula of the scattering intensity (E.q 2.84) [77]

$$\frac{d\Sigma}{d\Omega}(Q) = n\Delta\rho^2 V^2 \tilde{P}(Q)S(Q). \tag{2.87}$$

The structure factor S(Q) is defined as

$$S(Q) = 1 + \frac{2}{N} \sum_{i=1}^{N} \sum_{j>i}^{N} \frac{\sin(Qr_{ij})}{Qr_{ij}},$$
(2.88)

where  $r_{ij}$  is the distance between the *i*-th and *j*-th particles. S(Q) describes the correlation

between the particle centers of mass. Specifically, when  $S(Q) \neq 1$ , the particles can be considered correlated, while S(Q) = 1 for uncorrelated particles. S(Q) is most prominent at small Q, while at large Q, the scattering from inner structure dominates representing the form factor. S(Q) is related to the pair correlation function g(r), which describes the local order of particles, i.e., the probability of finding a particle at a given distance from another one:

$$S(Q) = 1 + 4\pi N \int_0^\infty (g(r) - 1) \frac{\sin(Qr)}{Qr} r^2 dr.$$
 (2.89)

S(Q) behaves like an oscillatory function, approaching a value of 1 for large Q [78].

#### Aggregated system

Aggregated nanoparticles are typically formed when the interactions between particles are strong enough that the cores come into contact. Visually, their structure may appear to be randomly ordered. In a fractal, the primary particles aggregate in such a way that the total mass of the particles is proportional to the power law of aggregate size  $\zeta$  [79]

$$M \propto \zeta^{D_f},$$
 (2.90)

where  $D_f$  is the fractal dimension, which describes the packing of the particles forming the aggregate. It takes values of 3, 2, and 1. The higher the value of  $D_f$ , the more densely packed the aggregates corresponding to globular aggregates ( $D_f = 3$ ). Another type of aggregate is characterized by the varying arrangement of particles with various scales called hierarchical structures [80]. For example, primary particles are arranged together to form clusters, which in turn are agglomerated into a mass fractal (see Fig. 2.9).

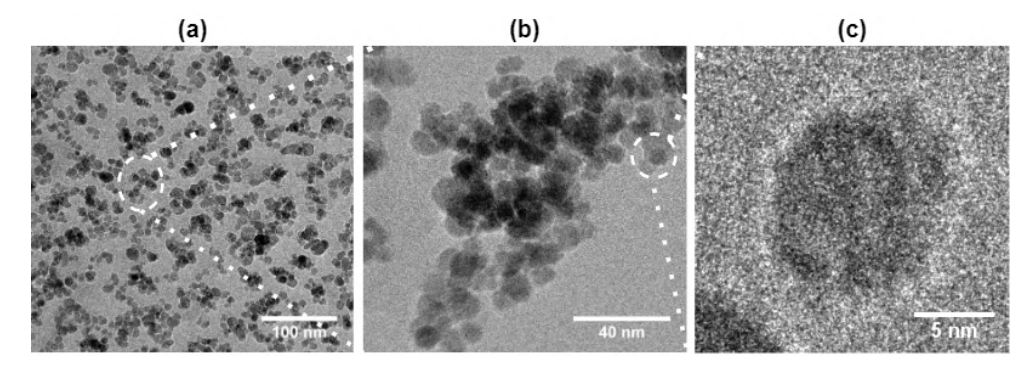


Figure 2.9: Electron microscopy images representing the arrangement of particles as a function of the scale (a) agglomeration of cluster particles, (b) aggregation of primary particles, and (c) the smallest building blocks [81].

The scattering intensity patterns are characteristic of three Q-regions

- The first region, known as the Guinier region, exists at small-Q values ( $Q < \zeta$ ) and follows the Guinier law, allowing to determine the size of the clusters.
- The second region, located in the intermediate Q-range  $(1/\zeta < Q < 1/r_{cluster})$ , displays a decreasing intensity that can be modeled as a power law of  $I(Q) \propto Q^{-D_f}$ , providing insights into the fractal dimension of the cluster particles and the cluster sizes. However, if the size of the clusters is very small compared to the sizes of the fractal, they may not produce distinct Guinier knees in the scattering pattern.
- Finally, the last region describes the scattering intensity behaviour from the primary particles, the smallest building blocks, appearing at the highest Q region ( $Q > 2/r_{core}$ ). The oscillatory behaviours are linked to the size distribution of the primary particles, which in turn helps to identify the degree of polydispersity within the sample. This region is associated with Porod zone of primary particles, which means that the scattering intensity decreases following a power law of  $I(Q) \propto Q^{-4}$  [82].

#### Pair Distance Distribution Function

The following method consists of inverse Fourier transformation of the experimental scattering intensity curves. This yields a Pair Distance Distribution Function (PDDF), P(r). The PDDF gives information about the structure in real space and needs to be compared to the calculated models, i.e. sphere and cylinder. The differential scattering cross-section in equation 2.83 can be rearranged to

$$\frac{d\sigma}{d\Omega}(\vec{Q}) = \left| F(\vec{Q}) \right|^2 = \left| \int_V \rho(\vec{R}) e^{i\vec{Q} \cdot \vec{R}} d^3 R \right|^2 
= F(\vec{Q}) \cdot F^*(\vec{Q}) = \int_V \int_V \rho(\vec{R}_1) \rho^*(\vec{R}_2) e^{i\vec{Q} \cdot \vec{R}_1 - \vec{R}_2} d^3 R_1 \ d^3 R_2.$$
(2.91)

We put  $\vec{r} = \vec{R}_1 - \vec{R}_2$  and use  $\vec{R}_2 = \vec{R}_1 - \vec{r}$ :

$$\frac{d\sigma}{d\Omega}(\vec{Q}) = \left| F(\vec{Q}) \right|^2 = \int_V \left[ \int_V \rho(\vec{R}_1) \rho^* (\vec{R}_1 - \vec{r}) d^3 R_1 \right] e^{i\vec{Q} \cdot \vec{r}} d^3 r$$

$$= \int_V \gamma_0(\vec{r}) e^{i\vec{Q} \cdot \vec{r}} d^3 r. \tag{2.92}$$

The term  $\gamma_0(\vec{r})$  is called the autocorrelation function of the scattering length density distribution and it is largest at the origin at r=0:

$$\gamma_0(\vec{0}) = \int_V \rho(\vec{R}_1) \rho^*(\vec{R}_1) d^3 R_1. \tag{2.93}$$

The scattering intensity is simply the Fourier transformation of the correlation function, hence providing information about the correlations within the scattering length density (SLD) at different separations r [83]. An example of the autocorrelation function for an individual spherical particle can be described geometrically as the overlap between the particle and its offset copy by the vector  $\vec{r}$ . In this case, the autocorrelation function

starts with  $\gamma(\vec{r}) = 1$  at r = 0, and gradually decreases and reaches zero at r = 2R, where R is the radius of spheres.

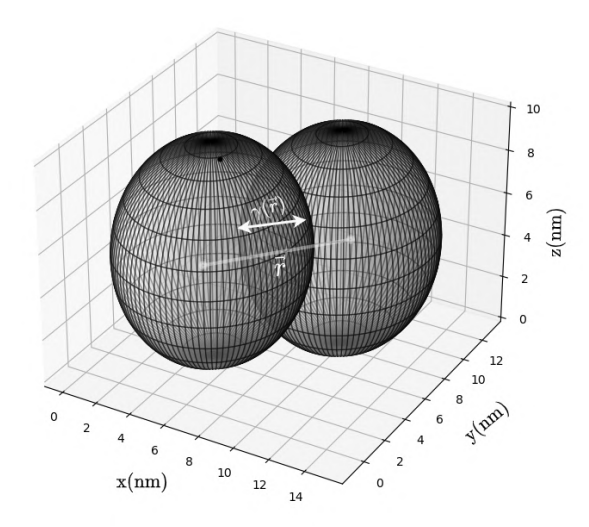


Figure 2.10: Physical meaning of the autocorrelation function for two identical spherical particles with radius R.

As we investigate structures in a solvent that has a different scattering length density, the contrast terms need to be included in the equation, which yields

$$\begin{split} \frac{d\sigma}{d\Omega}(\vec{Q}) &= \int_{V} \left[ \int_{V2} \Delta \rho(\vec{R}) \Delta \rho(\vec{r} + \vec{R}) d^{3}R \right] e^{i\vec{Q} \cdot \vec{r}} d^{3}r \\ &= \int_{V} \Delta \rho^{2} \gamma_{0}(\vec{r}) e^{i\vec{Q} \cdot \vec{r}} d^{3}r \\ &= \int_{V} \gamma(\vec{r}) e^{i\vec{Q} \cdot \vec{r}} d^{3}r, \end{split} \tag{2.94}$$

where  $\gamma(\vec{r}) = \Delta \rho^2 \gamma_0(\vec{r})$ . It is defined as the auto-correlation function of the scattering length density contrast. Finally, the scattering cross-section is written in spherical coordinates as:

$$\frac{d\sigma}{d\Omega}(\vec{Q}) = 4\pi \int_0^{D_{\text{max}}} r^2 \gamma(\vec{r}) \frac{\sin(Qr)}{Qr} dr, \qquad (2.95)$$

$$P(\vec{r}) \propto 4\pi r^2 \gamma(\vec{r}).$$
 (2.96)

Mathematically,  $P(\vec{r})$  can be obtained from the differential cross-section through an inverse Fourier transform:

$$P(\vec{r}) = \frac{2}{\pi} \int_0^\infty Qr \frac{d\sigma}{d\Omega}(\vec{Q}) \sin(Qr) dQ. \tag{2.97}$$

The P(r) function provides information about the maximum dimension of particles, where it reaches zero value at  $r = D_{max}$ . The behaviour of the P(r) function can also be directly used to obtain information about the overall shape of the studied objects, such as to distinguish spherical from prolate objects [84]. However, particle aggregation can affect the quality of P(r) giving a 'tail' in the function with larger values than expected for the largest inter-particle distance,  $D_{max}$ .

#### Contrast variation

The contrast, defined as  $\Delta \rho = \overline{\rho} - \rho_s$ , represents the difference between the average scattering length density (SLD) of particle and the scattering length density of solvent. The contrast dependence of small-angle scattering follows the three basic scattering functions [85]

$$I(Q) = (\Delta \rho)^2 I_c(Q) + (\Delta \rho) I_{cs}(Q) + I_s(Q), \tag{2.98}$$

where I(Q) is the total scattering,  $I_c(Q)$  is the shape scattering which can be used to determine the average particle shape at infinite contrast  $(\Delta \rho \to \infty)$ .  $I_s(Q)$  is the scattering by the inner inhomogeneities within the particle which can be measured directly at zero contrast  $(\Delta \rho = 0)$ , when the particle is said to be contrast match i.e.  $\bar{\rho} = \rho_s$ .  $I_{cs}$  is the term correlating both the shape and inner structure. Fig. 2.11 shows that the expansion enables the separation of contributions from the particle shape and its inner inhomogeneities to the scattering intensity. At least scattering intensities for three different contrasts has to be collected in order to obtain the basic scattering functions. Contrast variation is achieved by isotope substitution in the solvent (i.e. a mixture of  $H_2O/D_2O$ ).

An important aspect of small-angle scattering is that zero-angle scattering and radius

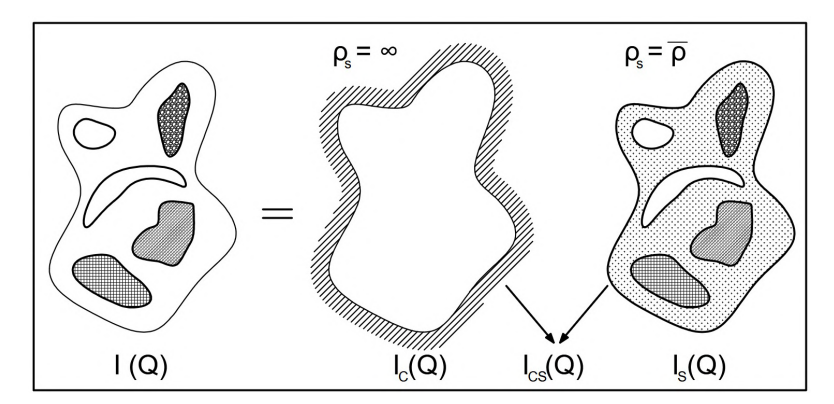


Figure 2.11: Contribution of the shape and inner structure. Figure is adapted from Ref. [72].

gyration of  $R_g$  depend on contrast. I(0) is a quadratic function of the contrast, as described by

$$I(0) = n(\Delta \rho)^2 I_c(0) = n(\Delta \rho)^2 V_c^2, \tag{2.99}$$

where  $V_c$  is the particle volume corresponding to the particle shape and n is the particle number density. A plot of the extrapolated zero-angle scattering intensity against the solvent SLD shows a minimum at the so-called match point, where I(0) assumes the value zero and thus the average SLD of the particles is equal to the SLD of the solvent at this point. The radius of gyration of a particle is given by

$$R_a^2 = R_c^2 + \alpha/\Delta\rho - \beta/\Delta\rho^2, \tag{2.100}$$

where  $R_c$  is the radius of gyration of the overall shape of the particle, obtained at infinite contrast (when  $1/\Delta \rho = 0$ ),  $\alpha$  and  $\beta$  describe the distribution of inhomogeneities within the particles;  $\alpha$  describes the relative arrangement of higher and lower density regions with respect to the center of mass of a shape  $\alpha > 0$ , if denser regions are close to the periphery, and vice versa. The value of  $\beta$  represents an estimate of the distance between the center of mass of a particle and that of the distribution of inhomogeneities ( $\beta = 0$ , if they coincide, and  $\beta \neq 0$ , if the particle center of mass is displaced with varying solvent SLD)[72].

#### 2.2.5 Anomalous scattering

Contrast variation is a crucial technique in neutron scattering, commonly achieved through isotope substitution, such as modifying the volume ratios of <sup>1</sup>H to <sup>2</sup>H. However, contrast variation can be implemented in SAXS by using X-ray energies near an absorption edge of elements present in the studied sample. This variation of the atomic scattering factor of elements also makes contrast variation possible. Then, the form factor close to the absorption edge can be expressed as [86]:

$$f(Q, E) = f_0(Q) + f'(Q, E) + if''(Q, E), \tag{2.101}$$

where  $f_0$  is the constant contribution to the form factor, f' and f'' are the real and imaginary part of resonance contributions, respectively. At small Q, this expression can be approximated as

$$f(E) = f_0 + f'(E) + if''(E), (2.102)$$

where  $f_0 = Z$ , with Z the atomic number of the element. The atomic scattering factor can be approximated as Z far from the absorption edges and is the only term considered

in standard X-ray experiments. Near the absorption edges both the resonant parts are included, which are energy dependent. Close to the edge f' decreases, therefore the intensity close to the edge decreases.

In anomalous small-angle x-ray scattering (ASAXS), the scattering intensity consists of a non-resonant, a mixed-resonant, and a pure-resonant terms [87]:

$$I(Q, E) = |f_{\text{non-res}}(Q, E)|^2 + |f_{\text{mix}}(Q, E)|^2 + |f_{\text{res}}(Q, E)|^2.$$
(2.103)

For a two-component system consisting of two elements, the scattering intensity calculated can be separated into the non-resonant scattering  $P_{11}$  for the first element, the pure-resonant  $P_{22}$  for the second element, and the mixed-resonant  $P_{12}$  for the pattern of the mixed elements. To separate the pure-resonant pattern, which is  $P_{22}$ , five different energies below the absorption edges are needed and, consequently, five different values of anomalous scattering factors [88]. In our project, we have used ASAXS to detect the increase of the valence state of Fe<sup>3+</sup> at the surface of the nanoparticles during the oxidation of magnetite nanoparticles, which have both valence states Fe<sup>2+</sup> and Fe<sup>3+</sup>, resulting in a magnetite maghemite core-shell structure.

#### 2.2.6 Macroscopic differential cross-section

The absolute scattering intensity  $I(\vec{Q})$  detected on 2D detector is a function of the following parameters [78]:

$$I_{\text{sample}}(\vec{Q}) = I_0 \cdot A \cdot d \cdot \Delta\Omega \cdot \epsilon \cdot T_{\text{sample}} \cdot \frac{d\Sigma_{\text{sample}}}{d\Omega}(\vec{Q}), \tag{2.104}$$

where  $\frac{d\Sigma}{d\Omega}(\vec{Q})$  is the macroscopic differential cross-section,  $I_0$  is the incoming neutron flux, T is the sample transmittance, A is the area of the sample, d is the thickness of the sample,  $\epsilon$  is detector efficiency, and  $\Delta\Omega$  is pixel size in units of solid angle. The  $\frac{d\Sigma_{\text{sample}}}{d\Omega}(\vec{Q})$  contains useful information about the structure of the sample; hence, it needs to be determined. However, the collected scattering intensity during the experiments contains not only helpful scattering from the sample but undesired scattering contribution from the sample holder (empty cell) and scattering from sources of background (blocked beam or electronic noise). The total scattering intensity is then written as

$$I_{\text{total}} = I_0 \cdot A \cdot d \cdot \Delta\Omega \cdot \epsilon \cdot T_{\text{sample+cell}} \cdot \frac{d\Sigma_{\text{sample+cell}}}{d\Omega} + I_{\text{bgd}}, \tag{2.105}$$

The measured empty cell scattering intensity is expressed as the following:

$$I_{\text{cell}} = I_0 \cdot A \cdot d \cdot \Delta\Omega \cdot \epsilon \cdot T_{cell} \cdot \frac{d\Sigma_{\text{cell}}}{d\Omega} + I_{\text{bgd}}, \tag{2.106}$$

The sample or empty cell transmissions are the ratio of the intensities through the sample or empty cell and the incident intensity, obtained with no sample in the beam path.

$$T_{\text{sample, cell}} = \frac{I}{I_0} = \exp\left(-\Sigma \cdot d_{\text{sample, cell}}\right),$$
 (2.107)

Where  $\Sigma$  is the total cross-section, including coherent, incoherent, and absorption cross-section. The thickness of the sample has to be thin enough to avoid multiple scattering, in which the scattered neutron is scattered again in the sample. Multiple scattering is favored by large-size scatterers, strong contrast, and its probability increases with the neutron wavelength [89].

The incoming flux,  $I_0$ , can be determined with a direct beam measurement with nothing in the beam except an attenuator:

$$I_{\text{direct}} = I_0 \cdot A \cdot d \cdot \Delta\Omega \cdot \epsilon \cdot T_{\text{atten}}, \tag{2.108}$$

where  $T_{\text{atten}}$  is the attenuator transmission.

From the Eqs. (2.105)-(2.106), the corrected data, but not calibrated data, can be calculated by the following:

$$I_{\text{corr}} = (I_{\text{total}} - I_{\text{bgd}}) - \frac{T_{\text{sample + cell}}}{T_{\text{cell}}} (I_{\text{cell}} - I_{\text{bgd}})$$
(2.109)

Where  $I_{\text{corr}}$  is the scattering of the sample corrected for the background scattering of the empty cell  $I_{\text{cell}}$  and other backgrounds such as the blocked beam, the electronic noise and the transmission of sample and empty cell.

Additionally, the detector efficiency should be taken into account. To correct the variation in detector efficiency, the measurement of a standard sample with a known cross-section is used [90]. The detector efficiency is usually measured before the experiment, i.e. at the beginning of the facility cycle. For SANS, samples with predominant incoherent scattering, such as water or Plexiglass plate, are indeed common for detector efficiency, which gives strong isotropic scattering. Such samples show a flat scattering profile that is independent of the scattering angle. The corrected SANS data is then calibrated with detector sensitivity  $I_{\text{calib}} = I_{\text{corr}}/\text{detector}$  efficiency. This measurement makes it possible to calculate the sensitivity of each pixel and thus obtain the calibration  $I_{\text{calib}}$ .

$$I_{\text{calib}} = I_0 \cdot A \cdot d \cdot T_{\text{sample+cell}} \cdot \frac{d\Sigma_{\text{sample}}}{d\Omega}(Q) \cdot \Delta\Omega \cdot \epsilon, \qquad (2.110)$$

To put the sample scattering cross-section on an absolute scale (i.e. with the exact knowledge of the incoming flux) the standard sample is measured with the exact same instrument configuration as the sample under study:

$$I_{\text{std}} = I_0 \cdot A \cdot d_{\text{std}} \cdot \Delta\Omega \cdot \epsilon \cdot T_{\text{std} + \text{cell}} \cdot \frac{d\Sigma_{\text{std}}}{d\Omega}, \tag{2.111}$$

where  $d_{\text{std}}$  is the thickness of the standard sample, which does not necessarily have to be equal to sample thickness d. The sample cross-section in absolute units is obtained as

$$\frac{d\Sigma_{\text{sample}}}{d\Omega} = \frac{I_{\text{calib}}}{I_{\text{std}}} \cdot \frac{d_{\text{std}}}{d} \cdot \frac{T_{\text{std +cell}}}{T_{\text{sample +cell}}} \cdot \frac{d\Sigma_{\text{std}}}{d\Omega}$$
(2.112)

Here, expression relates the differential cross-section of the sample to the differential cross-section of the standard sample to quantities measured during the scattering experiment, namely the intensity and the transmission. In addition, all the terms relating to the geometry of the instrument in E.q 2.104 are canceled out.

Further correction for nanoparticles in solutions, particle scattering intensity is obtained by the following:

$$\frac{d\Sigma_{\rm NP}}{d\Omega} = \frac{d\Sigma_{\rm NP+solvent}}{d\Omega} - (1 - C_{\rm vol}) \frac{d\Sigma_{\rm solvent}}{d\Omega}, \tag{2.113}$$

where  $C_{\text{vol}}$  is the volume concentration of the nanoparticles.

## 2.3 Mössbauer spectroscopy

Mössbauer Spectroscopy is a method used to study the magnetic structure in materials by analyzing the absorption spectrum of  $\gamma$ -rays by the  $^{57}$ Fe nuclei. The basic principle of  $^{57}$ Fe-Mössbauer spectroscopy is the utilization of the recoil-free-emission and resonant absorption of  $\gamma$ -rays by the  $^{57}$ Fe nuclei, which was discovered by R. L. Mössbauer in 1957 and later become commonly known as Mössbauer effect. Fig. 2.12 shows that the radioactive source material ( $^{57}$ Co) decays into the excited state  $^{57}$ Fe (I=5/2) with a half-life of about 270 days. From the excited state, the nuclei can either decay to the ground state I=1/2 via emission of a gamma ray with energy of 136 keV or decay to the state I=3/2, followed by the transition to the ground state by emitting a  $\gamma$ -ray with energy 14.4 keV. The half-life of the I=3/2 state is 97.8 ns.

In the Mössbauer technique, the 14.4 keV  $\gamma$ -rays are partially absorbed by the material, and those transmitted through the sample are detected. In general, the Fe nuclei in the sample have a different environment than the Fe nuclei in the source. This difference can lead to the absence of resonant absorption, meaning that the energy of the  $\gamma$ -rays may not match the energy gap in the sample. For this purpose, the source is moved relative to the absorber at different velocities v, which leads to tuning the energy of the  $\gamma$ -rays emitted by the source via the Doppler effect, as described by equation 2.114. For a velocity of v=12 mm/s, one can detect the energy variation with a resolution in the range of neV.

$$E(v) = E_{\gamma} \left( 1 + \frac{v}{c} \right) \to E(12 \text{ mm/s}) = E_{\gamma} + 720 \text{ neV},$$
 (2.114)

Another important requirement for the Mössbauer effect is the embedding of the  $^{57}$ Fe nuclei in a solid medium, such as a crystalline structure. In a free atom, the nucleus recoils due to the conservation of momentum, causing the emitted  $\gamma$  rays to have lower energy than the nuclear transition energy. This results in a shift of the emission and absorption lines due to the recoil energy. However, when the Fe nuclei are fixed within

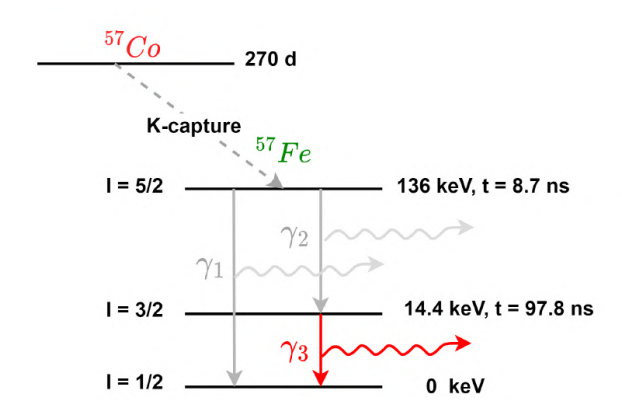


Figure 2.12: Decay scheme of  $^{57}$ Co nucleus into excited state of the  $^{57}$ Fe nucleus. The transition energy from the state with I=3/2 to the ground state I=1/2 is used in Mössbauer spectroscopy. Figure is adapted from [91].

the crystal lattice, the recoil energy is absorbed by the surrounding lattice rather than being transferred to the Fe nuclei. This phenomenon allows for recoil-free emission and absorption of  $\gamma$ -rays, which is the essence of the Mössbauer effect.

Mössbauer spectroscopy allows one to analyze variations in nuclear energy levels with high energy resolution (on the scale of neV), visible by shifts in the absorption lines caused by electronic and magnetic interactions (hyperfine interactions) of the iron nucleus with its local environment. The three main types of hyperfine interactions are the isomer shift, quadrupole splitting, and magnetic hyperfine splitting (see Fig. 2.13). The isomer shift arises from the interaction between the nucleus and its electronic surroundings, being significantly influenced by the s-electrons due to their high probability density near the nucleus. However, these s-electrons can be screened by intervening electrons i.e. the 3d-electrons in iron, resulting in different isomer shifts seen in Fe<sup>2+</sup> and Fe<sup>3+</sup>. Thus, the isomer shift provides valuable information about valence states due to the electronic screening directly impacting the density of s-electrons surrounding the nucleus. The quadrupole splitting arises from the interaction between a nucleus carrying an electric quadrupole moment and an electric field gradient, which can be found in certain crystal environments due to anisotropic charge distribution. In the ground state, the iron nucleus with (I=1/2) does not have an electric quadrupole moment. However, in the excited state (I=3/2), the nucleus can have a non zero quadrupole moment, resulting in the splitting of the energy level into two sublevels. In the case of magnetic hyperfine splitting, the nuclear energy level splits into 2I + 1 sublevels, which is observed in the presence of an external magnetic field due to its interaction with the nuclear magnetic dipole moment. For the Fe nucleus, it is split into four sublevels for the state with I = 3/2 and two sublevels for the ground state with I=1/2. Due to the selection rules of dipole radiation, only transitions of  $\Delta m = 0, \pm 1$  are allowed. Therefore, for the transition from  $3/2 \to 1/2$ , there are only six possible transition lines in the Mössbauer spectra. Magnetic hyperfine splitting is also influenced by the local magnetic fields from magnetically ordered materials.

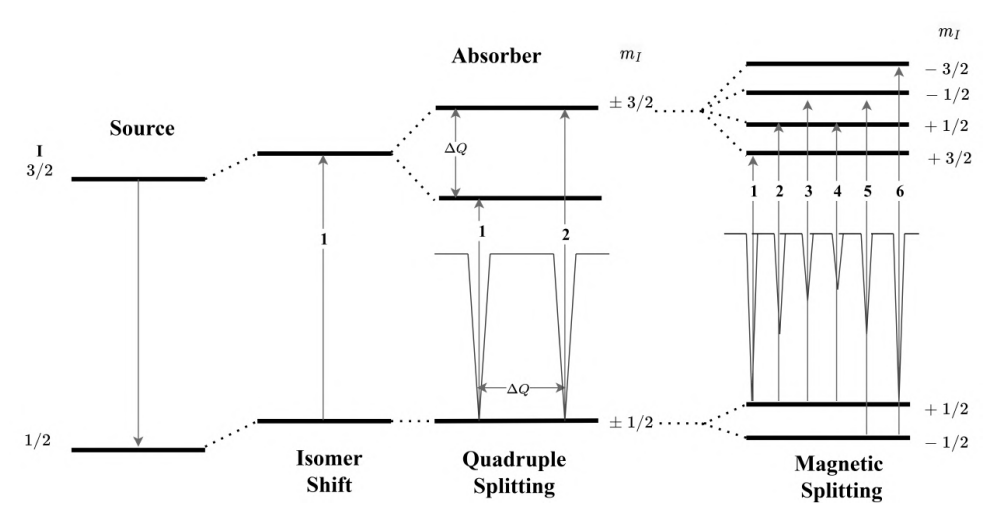


Figure 2.13: Hyperfine interactions within the absorber material and the resulting Mössbauer spectrum. Figure is taken from Ref. [92].

Mössbauer spectroscopy in large magnetic fields is a very useful method to investigate spin canting in magnetic materials [93]. The line intensities in the magnetic hyperfine splitting depend on the angle  $\theta$  between the spin direction and the direction of the incident  $\gamma$ -rays. Here, the line intensities ration follows the pattern 3:A<sub>25</sub>:1:1:A<sub>25</sub>:3, where the line intensity ratio of lines 2 and 5 is defined by

$$A_{25} = \frac{I_2}{I_5} = \frac{4\sin^2(\theta)}{1 + \cos^2(\theta)}. (2.115)$$

When the spins are aligned coaxially with the  $\gamma$ -ray direction (i.e.  $\theta = 0^{\circ}$ ), the coefficient  $A_{25}$  approaches zero, indicating that the intensities of lines 2 and 5 are negligible. As spin canting occurs, with  $\theta$  varying between  $0^{\circ}$  and  $90^{\circ}$ , the  $A_{25}$  value ranges from 0 to 4 due to the effects of spin orientation. At an angle of  $\theta = 54.7^{\circ}$ , the general line intensity ratio transitions to 3:2:1:1:2:3. This change indicates that spin canting has a significant impact on the observed intensities.

Mössbauer spectroscopy can also be used to study fluctuations of the magnetic moments in the sample by observing the fluctuations of the magnetic hyperfine interaction [94].

## 2.4 Micromagnetic simulations

Micromagnetic theory (or the so-called continuum description) is an approach to describe the macroscopic magnetization of usually metallic ferromagnetic or ferrimagnetic materials using a continuous magnetization vector  $\vec{M}(r,t)$  instead of localized atomic magnetic moments. However, often this approach is nevertheless also employed to model systems with localized magnetic moments. Typically, the size of the investigated systems ranges from 0.01  $\mu$ m to 10  $\mu$ m [95]. The magnetization  $\vec{M}(r,t)$  can be written as  $\vec{M}(r,t) = M_s \vec{m}(r,t)$ , where  $M_s$  is the saturation magnetization, which is assumed to be constant in magnitude, and  $\vec{m}(r,t)$  is the normalized magnetization vector.

Within the micromagnetic simulation framework, one investigates both the static and dynamic behaviour of samples in the continuum description by solving the Landau-Lifshitz-Gilbert (LLG) equation of motion of the magnetization vector for each discretization cell of the sample. The magnetization dynamics is governed by the Landau-Lifshitz equation [96]:

$$\frac{d\vec{M}}{dt} = -\frac{\gamma}{1+\alpha^2} \vec{M} \times \vec{H}_{\text{eff}} - \frac{\alpha}{M_S(1+\alpha^2)} \left( \vec{M} \times \vec{M} \times \vec{H}_{\text{eff}} \right)$$
(2.116)

or in the equivalent form given by Gilbert

$$\frac{d\vec{M}}{dt} = -\gamma \vec{M} \times \vec{H}_{\text{eff}} + \alpha \left( \vec{M} \times \frac{\partial \vec{M}}{\partial t} \right) \quad \text{with} \quad \vec{H}_{\text{eff}} = -\frac{\partial E}{\partial \vec{M}}, \tag{2.117}$$

where  $\gamma$  is the gyromagnetic ratio and  $\alpha$  is the damping constant. The effective field (H<sub>eff</sub>) provides a torque that acts on the magnetization, and it is defined as the negative functional derivative of the total magnetic energy. The equation is a nonlinear partial differential equation of space and time, which can be numerically solved by initial conditions and boundary conditions [97]. The first term in Eq. 2.117 represents the precession of the magnetization vector around the effective field while the second term describes the dissipation of energy and consequently the damping of the magnetization vector rotation. It causes the magnetization to become eventually aligned parallel to the effective field as the system proceeds towards equilibrium. The main method used in this work is to use the integration of the LLG equation to minimize the energy. For this purpose, it is better to use a large value for the damping constant and remove the precession term.

#### 2.4.1 The effective magnetic field

In the concept of micromagnetics the total magnetic energy of a bulk ferromagnet can be expressed as

$$E_{\text{tot}} = E_{\text{exc}} + E_{\text{ani}} + E_{\text{demag}} + E_{\text{Zeem}}, \tag{2.118}$$

which consists of the following energy contributions:  $E_{\rm exc}$ , due to the exchange interaction,  $E_{\rm ani}$ , due to the magnetocrystalline anisotropy,  $E_{\rm demag}$ , due to the demagnetization, and  $E_{\rm Zeem}$ , due to the potential energy in an external magnetic field. The total energy can be considered as a function of ferromagnet's magnetization, in which energies appearing in the atomistic level are substituted by a functional of  $\vec{M}$  and is expressed as

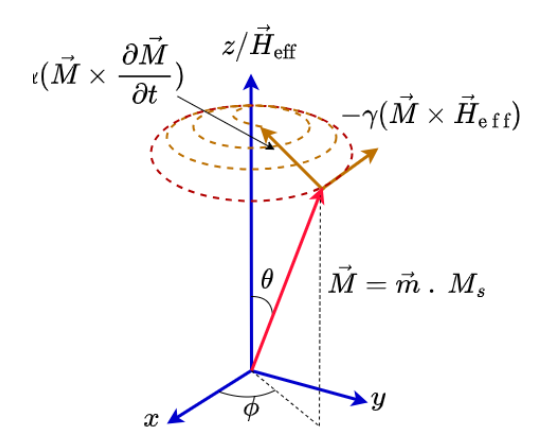


Figure 2.14: Sketch of the precession of the magnetization vector,  $\vec{M}$ , precessing around the effective field,  $\vec{H}_{\rm eff}$ , with damping effects, which are described by the Landau-Lifshitz-Gilbert equation.

$$E_{tot} = \int_{V} \left[ A_{ex} (\nabla M)^{2} + K_{u} (\vec{M} \cdot \vec{u})^{2} - \frac{1}{2} \mu_{0} \vec{M} \cdot \vec{H}_{d} - \mu_{0} \vec{M} \cdot \vec{H}_{ext} \right] dV, \qquad (2.119)$$

where  $A_{\rm ex}$  is the exchange stiffness,  $K_1$  is the first order term of the anisotropy energy,  $\vec{u}$  is the anisotropy easy-axis unit vector,  $\vec{H_{ext}}$  and  $\vec{H_d}$  are the external field and demagnetization field, respectively. The effective magnetic field is then written as

$$\vec{H}_{\text{eff}} = -\frac{\partial E}{\partial \vec{M}}.\tag{2.120}$$

In a micromagnetic system, the competition between exchange and magnetostatic self-interactions is characterized by a characteristic length scale, the so-called exchange length,  $l_{ex}$ . It describes the distance at which the exchange interaction dominates [98]. It is defined as

$$l_{\rm ex} = \sqrt{\frac{A_{\rm ex}}{\mu_0 M_s^2}}.$$
 (2.121)

The exchange length typically does not exceed a few nanometers in ferromagnetic materials, imposing significant constraints on the mesh size required for numerical simulations in order to keep the computation time low and resolve important magnetization processes [99].

#### 2.4.2 The Stochastic Landau-Lifshitz equation

In a nanomagnetic system, with decreasing the size, the anisotropy barrier can be small enough to be overcome by thermal fluctuations at relevant temperatures as described above. However, the Landau–Lifshitz equation does not include temperature effects in its definition. Therefore, thermal activation is important in order to understand magnetic relaxation from a fundamental point of view. Thermal activation can be introduced using a stochastic thermal field,  $\vec{H}_{th}$ , which is added to the effective magnetic field,  $\vec{H}_{\text{eff}}$  [100]. It can be modeled as

$$\vec{H}_{\rm th} = \vec{\eta} \sqrt{\frac{2\alpha k_B T}{\gamma M_s V \Delta t}},\tag{2.122}$$

where  $\Delta t$  is the time step, and  $\vec{\eta}$  is a random vector redetermined for every time step. It can be considered as a white noise, which introduces randomness in the system and is independent across time steps. We applied, in particular, the so-called "theta evolver" inside the Object Oriented Micromagnetic Framework (OOMMF) to be able to investigate the influence of temperature. This add-on to the OOMMF software is developed at Hamburg University [101].

In this thesis, the OOMMF software provided by the National Institute of Standards and Technology (NIST), is used to solve the LLG equation [102]. The simulation process begins with specifying essential input material parameters (e.g. anisotropy, K, saturation magnetization,  $M_s$ , exchange stiffness, A) and the external field,  $\vec{H}_{\rm ext}$ , as well as the geometry of the material i.e, Rectangle, spheres, cylinders. The input parameters and the initial conditions of any problem are specified in OOMMF micromagnetic input format (MIF).

OOMMF uses the finite difference (FD) method to find the solution of the LLG equation, which requires the discretization of the sample [95]. The geometry under study is represented by a cubic mesh of small finite elements of the same size, where each cell is defined by the dimensions  $\Delta x$ ,  $\Delta y$ , and  $\Delta z$ , within each magnetization is uniform. The dimension of cells is a crucial parameter. It is better to choose a smaller cell size to better resolve the geometry, but not too small to avoid long calculation times. In general, it is important to choose a cell size smaller than the exchange lengths in order to achieve accurate results. The time evolution of the system is also treated with a discrete time step of  $\Delta t$ . It is important for the time step to be at least two orders of magnitude smaller than the precession frequency [99]. This requirement means that the time step is on the order of  $10^{-13}$  s. As a result, simulations can effectively explore time scales on the order of  $10^{-9}$  s.

Within each cell, a magnetization vector is positioned in the center of each mesh. The basic idea of the finite difference method is to approximate the derivatives of  $\vec{m}(r)$  by quotients of finite differences  $\Delta x$ ,  $\Delta y$ ,  $\Delta z$ . After discretization, the partial differential equations can be transformed into a system of algebraic equations, which is solved numerically by an iterative process to obtain an approximate solution. The discretization in the finite

difference method for the energy terms can be approximated by replacing the integral with a sum over all grid points. Volume quantities such as the magnetization and the effective field are treated at the center of each cell (and considered constant within each cell). Coupling quantities, such as the exchange field, are considered at the surfaces between the cells. After discretization, the partial differential equations can be transformed into a system of algebraic equations, which is solved numerically by an iterative process to obtain an approximate solution.

## Chapter 3

## Instruments

This chapter provides details on the instruments used to characterize the structure and magnetic behaviour of the SPIONs. It also presents the sample environments used in most of these studies.

### 3.1 Small-angle scattering

# 3.1.1 Gallium Anode Low Angle X-ray Instrument (GALAXI) & KWS-X: The SAXS/WAXS Laboratory beamline

SAXS experiments were performed at the instrument GALAXI (Gallium Anode Low-Angle X-ray Instrument) at the institute JCNS-2, Forschungszentrum Jülich [103]. The setup of GALAXI is illustrated in Fig. 3.1. This instrument is equipped with a metal-jet X-ray source and a Pilatus 1M 2D position-sensitive detector. Using a metal jet of a GaInSn alloy as the anode allows for generating a high-intensity and brilliant X-ray beam. At the sample position, the flux of  $1 \times 10^9$  photons/mm<sup>2</sup>·s is achieved [103]. A parabolic Montel-type optics is used to obtain monochromatic X-ray beams with Ga  $K_{\alpha}$  radiation of wavelength  $\lambda = 0.13414\,$  nm. The X-ray beam size is defined and collimated by two slits  $S_1$  and  $S_2$  separated by a 4 m distance and with an inclination of 0.4°. To reduce the background, a third slit  $S_3$  is used, allowing the sample zone width to be only few mm. The X-ray beam path is fully evacuated between the X-ray source and the detector. The detector distance can be adjusted between 0.835 m and 3.535 m in 5 steps, which allows the scattering vector Q to cover a wide range from 0.004 to 8 nm<sup>-1</sup>.

SAXS experiments were also performed at KWS-X: X-ray laboratory of JCNS at Heinz Maier-Leibnitz Zentrum (MLZ). The SAXS instrument is equipped with a high flux metal-jet source and a moveable Eiger 2R4M SAXS detector. The metal-jet composed of a GaInSn alloy used as a source to produce X-ray radiation of Ga K $\alpha$  with  $\lambda=0.13414\,$  nm. The scattering vector Q covers a wide range from 0.002 to 0.7 nm<sup>-1</sup>.

For SAXS measurements, nanoparticle dispersions in water were sealed in quartz capillaries with 2 mm diameter and 0.01 mm wall thickness. Background measurements with empty capillaries as well capillaries filled with water were preformed. The SAXS measurments

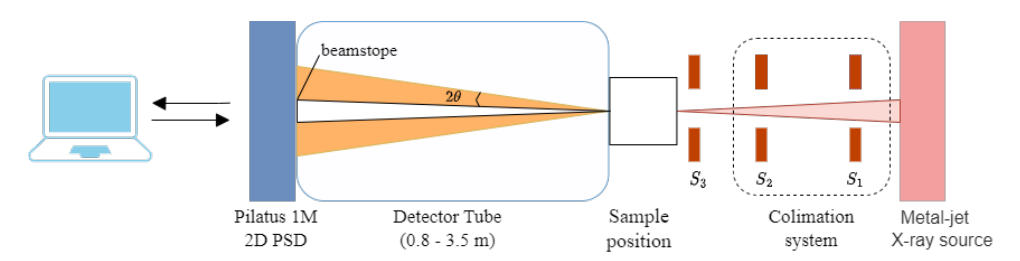


Figure 3.1: Schematics of the instrument GALAXI showing the main components. Figure adapted from Ref. [103].

were preformed in transmission mode.

## 3.1.2 Small-Angle X-ray Scattering beamline for Materials Research (SAXS-MAT) P62 beamline

The SAXS experiments were performed at the P62 beamline at PETRA III at DESY, Hamburg [104]. The beamline uses a U32 undulator with a peak brilliance  $1 \times 10^{20}$  photon s<sup>-1</sup> mard<sup>-1</sup> at 7 keV and provides a wide X-ray energy range from 3.5 keV to 35 keV. This allows for performing anomalous small-angle X-ray scattering (ASAXS) experiments and therefore obtaining element sensitive structural information. This option allows to perform X-ray absorption near edge structure (XANES) studies.

The beamline layout is divided into three parts: the front end, the optical, and the experiment hutches. A schematic sketch of the beam optics is shown in in Fig. 3.2. From the source to the sample, the beam must pass a Si(111) pairs double-crystal monochromator and focusing mirror. The function of the Si(111) monochromator is to select the desired photon energy with an accessible energy range of 3.5–35 keV from the incident white synchrotron radiation beam. An additional Si(311)-pair of crystals is implemented to increase the energy resolution and to obtain higher X-ray energies. After passing through the monochromator, the beam is focused vertically with two mirrors. It also uses 2D-Be compound refractive lenses (CRL) to to enhance the focusing capabilities of the beamline.

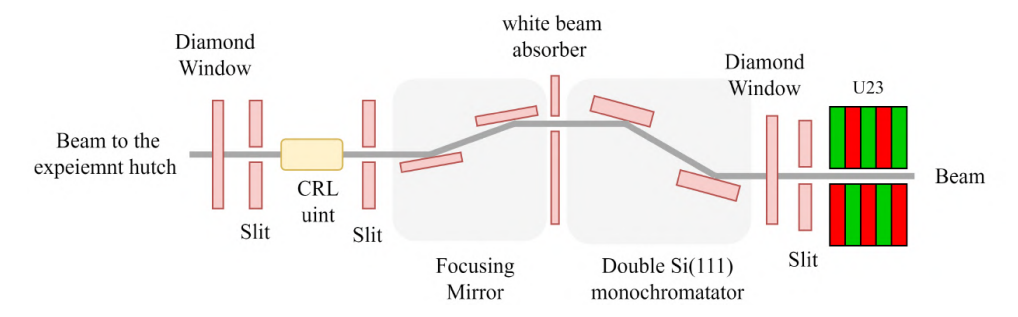


Figure 3.2: Schemeatics of the optics of the P62 beamline. Figure adapted from Ref. [104].

The experiment hutch includes optics components, sample position, and SAXS/WAXS instrumentation as shown in Fig. 3.3. The optical components are located inside a vacuum tube and include the following: slits system, an absorber to adjust the primary intensity, a fast shutter, and a monitor that counts the intensity of the monochromatic beam during data collection. The sample environment is placed on the top of the table at a nominal sample position. The sample may be exposed to different environment conditions: vacuum, and high and low temperatures. A after the sample position, there is a vacuum stainless steel tube being 13 m of length with the detector inside. A motorized translation stage inside the tube moves the SAXS detector and beamstops from 1.9 m to 13.0 m to the sample position. The SAXS detector is an Eiger2 X 4M. The WAXS detector is an Eiger2 X 9M, which is mounted outside the tube system and the sample to detector distance can be adjusted within 0.2 m to 0.7 m.

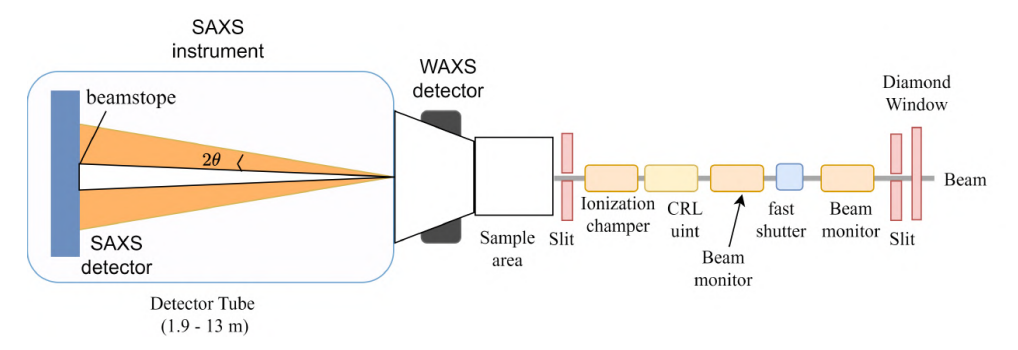


Figure 3.3: Schematics of the SAXS setup in the experiment hutch of the P62 beamline. Figure adapted from Ref. [104].

For SAXS measurements, the powder samples were fixed between two pieces of Kapton foil, ensuring they were not closed tightly to allow exposure to environmental conditions. Fig. 3.4 shows the samples being mounted on a piece of the ceramic heater with a hole in the middle to let the X-ray beam pass through. SAXS/WAXS measurements were first performed at ambient temperature, followed by heating for approximately half an hour at two different temperatures, 120°C and 170°C, in vacuum for the reduction process. The temperature was then kept constant for 5 h, followed by the x-ray absorption near edge spectroscopy (XANES) and SAXS/WAXS measurements. After completing the reduction measurements, the samples were exposed to air and oxidized at two temperatures, 80°C and 120°C, for 4 h, followed by SAXS/WAXS measurements. The XANES measurements were conducted separately from the SAXS/WAXS measurements to capture the changes in the sample during annealing, as each spectrum takes 7 minutes. The samples were measured in transmission mode for SAXS/WAXS and XANES. For the experiments as described here, we used iron foil as a reference sample for the Fe K-absorption edge. Because the X-ray K-edge of Fe is at 7112 eV, we chose five X-ray energies for the SAXS/WAXS measurement that are sufficiently below Fe K-edge. X-ray absorption edges are found at 7103, 7093, 7073, 6953, 6793, and 6473 eV.

XANES was chosen due to its sensitivity to the electronic configuration of atoms, i.e. their oxidizing state. XANES focuses on the K absorption edge in case of 3d and 4d transition metals, which is the highest excitation level in terms of energy corresponding to an excitation of a 1s electron. Key features of interest in XANES include the absorption edge and the pre-edge region. By comparing the positions of the absorption edges across different compounds containing the same element, shifts in the edge position can be correlated with changes in oxidation states. Generally, an increase in oxidation state results in a corresponding rise in edge energy [105].

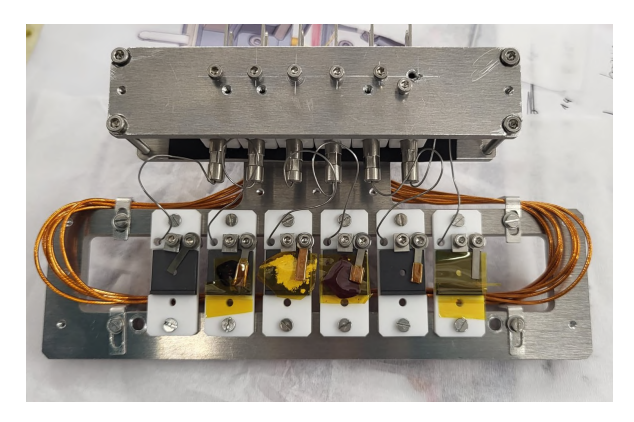


Figure 3.4: Mounting of the powder sample in the ceramic heater.

#### 3.1.3 Quokka, ANSTO

Small-angle neutron scattering (SANS) measurements were performed at the QUOKKA instrument of the Australian Center for Neutron Scattering (ACNS), at the Australian Nuclear Science and Technology Organization (ANSTO), NSW, Australia [106, 107]. Fig. 3.5 shows a sketch of the QUOKKA instrument layout.

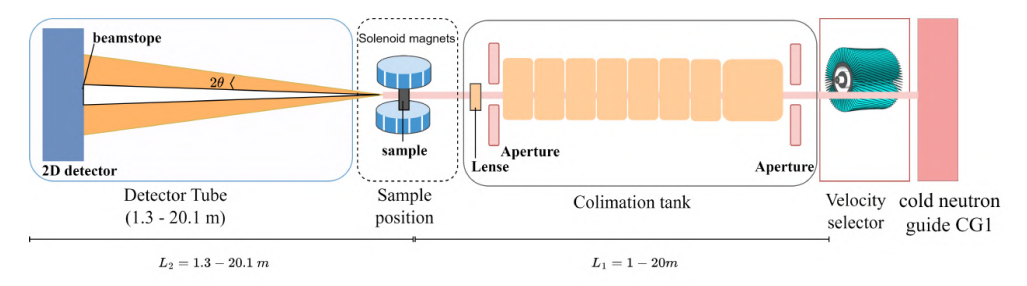


Figure 3.5: Scheme of the QUOKKA instrument layout. Figure adapted from Ref. [107].

The neutrons are produced in the core of the OPAL research reactor using a uranium fission process that generates a thermal power output of 20 MW. The produced neutrons

are then moderated with water  $(H_2O \text{ and } D_2O)$ , where the reactor core is surrounded by the  $D_2O$  tank, and the outer area of the water tank is filled with  $H_2O$ . This setup moderates the neutrons energy to the temperature of the surrounding water to obtain the wavelength of the order of several Å. Additionally it also serves as a biological shielding. The thermal neutrons are effectively moderated again by liquid  $D_2$ , producing cold neutrons that are directed to the SANS setup through the cold neutron guide CG1. The principle of their operation is based on total internal reflection phenomena and is similar to one of the light guides, where the light propagating in an optically dense media is totally reflected from the glass-air interface. In the neutron guide, the index of refraction of the mirror coating applied to the guide is less than 1, effectively preventing the neutrons from escaping the guide and transporting them to the scattering instruments. The cold neutron guide CG1 made of borosilicate glass with polished surfaces, coated with special neutron-reflecting materials of Ni-Ti supermirrors [108].

A velocity selector is used to select a neutron wavelength in the range from 4.5 to 43 Åwith a resolution from 4.1 to 14 %. The incoming neutron flux is then monochromatized. The source-to-sample distance  $(L_1)$  can be adjusted from 1 to 20 m through controlling the arrangement of the neutron guides in the collimation tank. The  $L_1$  is usually chosen as a compromise between flux intensity and the desired Q-resolution of the instrument. The more guided neutrons, the better the resolution, but the cost of decreased intensity. The setup also uses 24 MgF<sub>2</sub> lenses inside the collimation tank for focusing the neutron beam and enabling it to perform low-Q measurements at a wavelength of 5 Å.

After the sample, there is a vacuum tank with 2D  $^3$ He gas-filled proportional counter detector inside, which is 20 m long. The detector can move along the tank so that the sample-to-detector distance ( $L_2$ ) can be varied from 1.3 up to 20.1 m thus providing an accessible Q-range from 0.004 Å $^{-1}$  (and from 0.0006 Å $^{-1}$  with focusing lens optics) to 1.3 Å $^{-1}$ . A beam stop made from boron carbide/aluminum composite material is used to protect the detector from the direct beam.

In this thesis, unpolarized small-angle neutron scattering (SANS) was used with a neutron wavelength of 5 Åand a wavelength resolution of 10 %. The citrate coated nanoparticles, coded as C71, dispersed in  $D_2O$  solvent were placed in a 1 mm quartz cuvette (Hellma) positioned within a sample holder designed for an electromagnet. The latter was used to apply vertical magnetic fields from 0 up to 1.1 T perpendicular to the neutron beam direction. The contrast variation experiment in zero magnetic fields was also performed by dispersing the C71 particles in variable mixtures of  $H_2O$  and  $D_2O$ . The measurements were performed at room temperature and at three detector distances (2, 12, and 20 m) to cover a Q-range of (0.004 – 0.7 Å $^{-1}$ ). The data reduction was performed using the IGOR Pro software [109].

## 3.2 Magnetometry devices

### 3.2.1 Superconducting Quantum Interference Device (SQUID)

The magnetometry data in this thesis have been obtained using a superconducting quantum interference device (SQUID) magnetometer (Quantum Design MPMS-XL). The MPMS design includes several components: the dewar, probe, SQUID, and electronic control system. The dewar is filled with liquid helium, which is used for cooling the sample space and the superconducting solenoid. The sample is mounted within a plastic straw and connected to the end of a sample rod, which is inserted into the sample space in the dewar. The other end is attached to a linear motor, which is used to precisely position the sample at the center of the SQUID pickup coils. The probe consists of a high-precision temperature control system that allows measurements between a range of 2-400 K, along with a superconducting magnet that generates vertical magnetic fields of up to 7 T and a detection coil (pick-up coil).

Fig. 3.6 shows the SQUID setup and basic principle. The sample is moved vertically through the pick-up coil in discrete steps using the DC option, as opposed to the Reciprocating Sample Option (RSO), where the sample is oscillated vertically using a motor. The pick-up coil, designed in the form of a second-order gradiometer, helps in suppressing any constant magnetic flux [110]. As the coil forms a closed superconducting loop, the change in magnetic flux is converted into a current. The current is coupled to a SQUID ring, which is then converted into a voltage signal. The output voltage signal (V) is recorded as a function of sample position. By analyzing the voltage curve, parameters of interest such as the net magnetic moment of the sample and its position inside the detection coil can be derived.

The core of the SQUID sensor consists of a superconducting ring with one (AC-SQUID) or two (DC-SQUID) Josephson junctions made of thin insulating material. This design enables electron pairs to tunnel across the weak link, resulting in a critical current ( $I_c$ ) [111]. The RF-SQUID sensor functions like an LC circuit with just one junction having a capacitance C within a superconducting loop with inductance L. The fundamental property of superconducting rings is that they enclose magnetic flux only in integer values of the magnetic flux quantum  $\Phi = n\Phi_0$ , where  $\Phi_0 = 2.07 \times 10^{-15}$  mT [112, 113]. This means that the sensitivity of the SQUID sensor is determined by the magnetic flux quantum. The total magnetic flux  $\Phi$  in the loop has a contribution from the circulating current I of the RF coil, which penetrates through the Josephson function, producing a super-current ( $I_s$ ) flowing across the weak link with a phase difference  $\Delta \phi = 2\pi \frac{\Phi}{\Phi_0}$  related to the critical current  $I_c$  as

$$I_s = I_c \cdot \sin(2\pi \frac{\Phi}{\Phi_0}). \tag{3.1}$$

An external magnetic flux  $\Phi_{ext}$  is added to the SQUID ring resulting from the current in the pick-up coil. The total magnetic flux in the SQUID loop is then given as

$$\Phi = \Phi_{\text{ext}} - LI_c \cdot \sin(2\pi \frac{\Phi}{\Phi_0}). \tag{3.2}$$

This external magnetic flux induces a circulating current to flow around the ring, leading to a change in phase difference across the weak link and causing alterations in the current inside the ring produced by the applied magnetic field. Detecting the resulting current inside the loop that has a period of variation of the magnetic flux quantum  $\Phi_0$  allows the use of SQUID as a highly sensitive magnetometer.

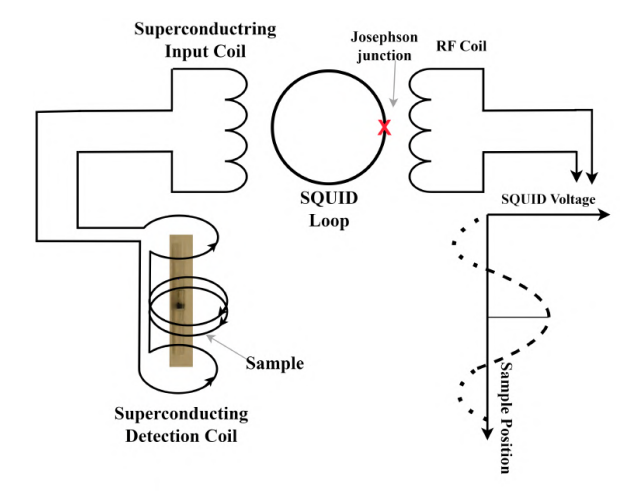


Figure 3.6: The SQUID design and principle. Figure adapted from Ref. [114].

In this thesis, magnetization measurements were conducted using zero-field-cooled (ZFC) and field-cooled (FC) protocols in a temperature range of 5 K to 225 K. These measurements aim at obtaining information about the particle size distribution and interparticle interaction. It is important to note that the chosen temperature range is well below the melting point of water, ensuring that the particle clusters inside the solvent remain immobilized, as shown in Fig. 3.7. To avoid the formation of large ice crystal domains, which would lead to an unwanted agglomeration of clusters inside the domains, the samples were rapidly cooled in a liquid nitrogen bath at room temperature. After cooling to 5 K, a small magnetic field of 5 mT is applied, and the ZFC magnetization curve is recorded while the temperature is gradually increased to 225 K. The FC magnetization curve is recorded while the temperature gradually decreases to 5 K in the same magnetic field.

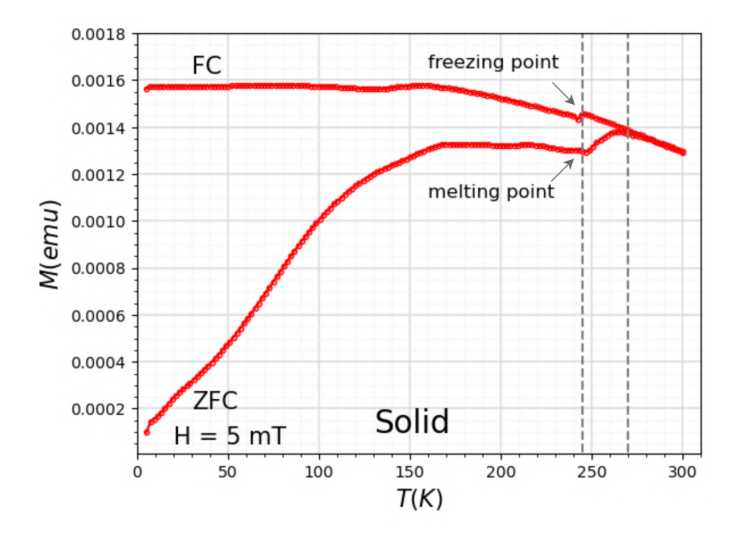


Figure 3.7: The magnetization measurements were recorded in a temperature range between 5 K and 225 K, with the area between two dashed lines representing the water melting range.

## 3.3 Cryogenic Transmission Electron Microscopy

In this thesis, cryogenic transmission electron microscopy (cryo-TEM) was employed to characterize the nanoparticles, particularly in a cryogenic environment, in terms of size, shape, and aggregation behaviour [115]. For this, a JEOL JEM-FS2200 field emission electron microscope operated at 200 kV was utilized.

A TEM instrument can be visualized as a light microscope, in which the sample is illuminated by an electron beam. The typical instrument combines three main components arranged in an evacuated column: the illumination system, the stage and objective lens, and the imaging system [116].

The illumination system consists of a field emission gun at the top of the instrument and two condenser lenses operating either a broad or a focus beam at the sample. The field emission consists of one cathode and two anodes. The first anode is charged with several kV with respect to the field emission tip to pull electrons out of the tip. The second anode accelerates the electrons to 100~kV or more. The electron source is considered an object for the illumination system and the two condenser lenses are used to illuminate the sample with a parallel beam of electrons.

The second component is the objective lens, which is the heart of the TEM, responsible for forming both images and diffraction patterns of the sample. After propagating through an objective lens all scattered electrons from the sample are focused on the image plane. The following diagram (see Fig. 3.8) shows the basic operations for forming image and diffraction patterns. It shows three important planes: the object plane, which always lies above the lens; the image plane, which contains the image point; and the focal plane of the

lens, where parallel rays are brought to a focus. The diagram also defines three important distances: the object distance  $(d_0)$ , which is the distance from the object plane to the lens; the image distance (d), which is the distance from the lens to the image plane; and the focal length (f), which is the distance from the lens to the back focal plane. The three distance combines in the following basic equation

$$\frac{1}{f} = \frac{1}{d_0} + \frac{1}{d}. ag{3.3}$$

The magnification equation of the a convex lens is [117]

$$M = \frac{d}{d_0} = \frac{d-f}{f}. ag{3.4}$$

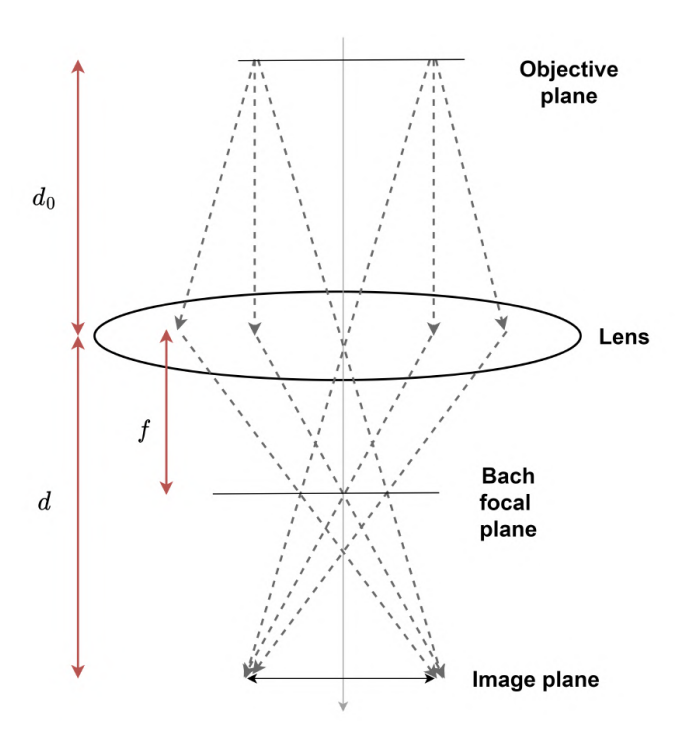


Figure 3.8: A diagram representation of the objective lens function in transmission electron microscopy.

Magnification can be adjusted by moving the object plane closer to the lens, thereby reducing  $d_0$  and increasing M. Additionally, changing the strength of the lens affects magnification. If the lens is made stronger, the f is shortened, which requires the d to be correspondingly shorter while the  $d_0$  remains unchanged, resulting in a smaller image magnification.

The real image is formed when the object distance (and therefore the image distance)

exceeds the focal length. In this case, a real image is produced on the other side of the lens, beyond the back focal plane. If the lens is too weak and the image forms below the desired image plane, the image will be out of focus, and the lens is said to be under-focused. Conversely, if the lens is too strong and the image forms above the image plane, the lens is referred to as over-focused [118].

The last component is the imaging system, which uses an intermediate lens and projection lenses further down the TEM column to magnify the image or the diffraction pattern produced by the objective lens and to focus these on the viewing screen. The adjustment of the strength of the intermediate lens (i.e. the focal distance) allows one to choose between imaging or diffracted modes. If the back focal plane of the objective lens acts as the object plane for the intermediate lens, we can obtain diffraction on the viewing screen. In imaging mode, the object plane of the intermediate lens is the image plane of the objective lens. The projection lenses are used for post-magnification of the image. The image formation by mass-thickness contrast or Diffraction contrast. Diffraction contrast arises when the electrons are Bragg-scattered. High-resolution TEM specifically uses diffraction contrast to enable the observation of crystal structures at the atomic level. This imaging mode allows for precise indexing of atomic planes by employing a Fast Fourier Transform (FFT) function [116]. The mass-thickness contrast technique for image formation arises from incoherent elastic scattering of electrons [119]. As electrons go through the sample, they are scattered off the axis by elastic nuclear interaction, i.e., Rutherford scattering. The cross-section for elastic scattering is a function of the atomic number (Z). As the thickness of the specimen increases, there will be more elastic scattering because the mean-free path remains fixed. Similarly, a sample consisting of higher Z elements will scatter more electrons than a low-Z sample. Thus, variation in the Z will cause a change in the contrast. Two different imaging modes use the mass-thickness contrast method: bright field and dark field. A sample of larger Z scatters electrons more strongly and therefore appears dark in bright field images and bright in dark field images. Fig. 3.9 presents the steps for preparing the sample for TEM imaging. The freezing takes place in a device called a plunge freezer (Fig. 3.9(a)). A 4  $\mu$ l droplet of SPIONs in a water solution with a concentration of 5.5 mg/ml is deposited onto a grid surface of 3 mm diameter that consists of copper meshes with perforated carbon foil (Fig. 3.9(b)). The excess liquid was then blotted with filter paper to ensure that the particles are trapped in a thin layer of ca. 100 nm in the holes of the carbon grid. After the blotting, the grid was then rapidly plunged into a bath of liquid ethane kept at the temperature  $-180^{\circ}$ C (Fig. 3.9(c)) to obtain an amorphous (non crystalline) ice film (Fig. 3.9(d))[120]. After freezing the sample, the grid was transferred immediately into liquid nitrogen and inserted into the cryo-holder. The cryo-holder was then immediately inserted into the TEM microscope. The images were taken using a cryo-TEM system with a G910 multi-position specimen cryo-holder.

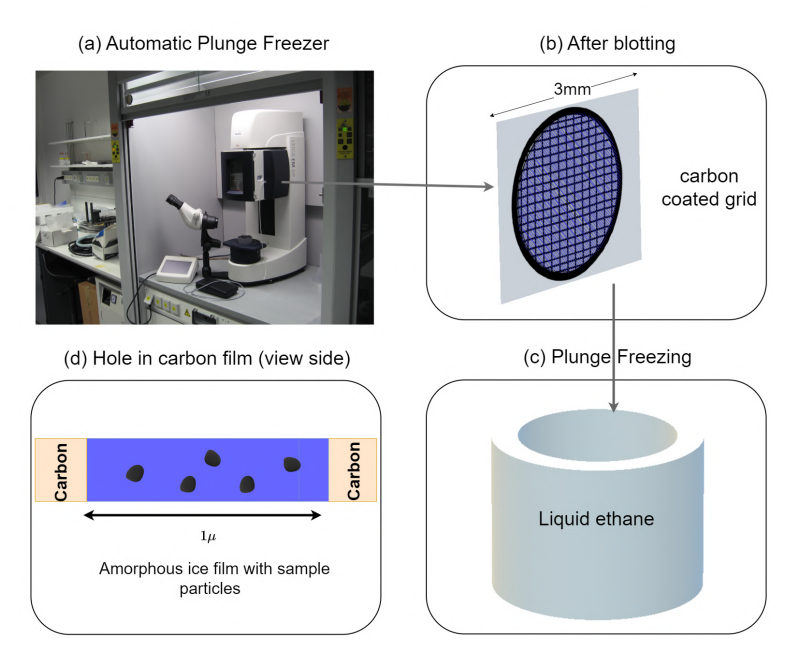


Figure 3.9: Sample preparation steps in a plunge freezer device (a), starting with the blotting step (b), followed by the freezing step (c) and ending with a thin film of the sample covering the holes of the grid (d).

# 3.4 Mössbauer spectroscopy

Mössbauer absorption spectra were obtained in a standard transmission geometry using a radioactive source consisting of  $^{57}$ Co embedded in a rhodium matrix material and a drive unit in constant acceleration mode. The rhodium matrix with a non-magnetic site provides a solid environment for the  $^{57}$ Co atoms. A liquid He cryostat (Oxford SM4000-10) with split-pair geometry of superconducting magnet coils was utilized to carry out experiments at 5 K in an external magnetic field of 8 T parallel to the  $\gamma$ -ray incidence direction. The measurement was performed at low temperatures to overcome the thermal effect that caused a reduction in magnetic splitting while applying a large external magnetic field to distinguish between ferromagnetic and antiferromagnetic ordering. Before the first Mössbauer spectrum was recorded, the particles dispersed in the water had been stored in sealed containers under  $N_2$  atmosphere. Samples were stored under ambient conditions during the oxidation studies. The liquid sample was sealed tightly in a copper cylinder capped with mylar foil. The experimental spectra were analyzed using a least squares fitting routine using the "Pi" program package [121] to determine the hyperfine parameters

.

# 3.5 X-ray powder diffraction

Synchrotron X-ray diffraction was performed on a material science (MS) beamline at the SESAME synchrotron, Jordan, at a wavelength of 0.059 nm [122]. The MS beamline is a wiggler-based beamline that uses two X-ray Rhodium-coated mirrors and a double crystal Si (111) Kohzu monochromator, while the second crystal horizontal curvature is bendable. An ionization chamber in the experimental station is used to continuously track the incident flux on the sample. An iron oxide nanoparticles dispersion in water were filled into glass capillaries as well as empty cell and water background mounted on a standard goniometer head and then fixed on a capillary spinner were used for the XRD measurements. To calibrate the instrument, a NIST (640f) Silicon standard was measured, using the lattice parameter of silicon to accurately determine the wavelength during the experiments The XRD experiments were collected in transmission mode at room temperature.

# 3.6 Inductively Coupled Plasma Optical Emission Spectroscopy

Inductively Coupled Plasma Optical Emission Spectroscopy (ICP-OES) is a powerful analytical technique used for the determination of metals in various types of samples. In this technique, a high-temperature plasma is used to excite atoms in the sample, which then emits characteristic electromagnetic radiation specific to the elements present. The intensity of this emitted radiation is proportional to the concentration of the element in the sample.

We determined the iron content in the samples using an iCAP 7600 device at the Central Institute for Engineering, Electronics and Analytics (ZEA-3), Forschungszentrum Jülich GmbH. For sample preparation, each sample was digested using a mixture of 2 mL of nitric acid (HNO<sub>3</sub>) and 1 mL of hydrogen peroxide ( $\rm H_2O_2$ ), which was then completely transferred into closed vessels for microwave digestion. The vessels were heated to 160°C over a period of 20 minutes and maintained at this temperature for 15 minutes to accelerate the reaction. After digestion, each solution was transferred and diluted to a final volume of 14 mL. Subsequently, two replicate dilutions of each digestion solution were prepared: one at a 20-fold dilution and another at a 5-fold dilution.

# 3.7 Dynamic light scattering

The hydrodynamic size of the nanoparticles in water was obtained by dynamic light scattering with a Nanophox photon cross-correlation spectrometer (Sympatec, Germany). After temperature equilibration at 25°C, DLS experiments were carried out with a set-up based on two He-Ne laser beams ( $\lambda=632.8$  nm) perpendicular to each other. The measurement time for the experiment was set at two minutes. The experiment was conducted in triplicate, and the results were averaged to obtain the final data. The

obtained intensity fluctuations of the scattered light over time from a fixed location are directly linked to the particles' motions or particle sizes [123].

# Chapter 4

# Water-Based Iron Oxide nanoparticles

The aim of this chapter is to provide an outline of the structure, magnetic properties, and oxidation stability of water-based iron oxide nanoparticles, in particular of particles in the form of clusters. In this work, we synthesized the iron oxide nanoparticles by co-precipitation method and then applied three different biocompatible coatings, such as negatively charged citrate, positively charged (3-aminopropyl)triethoxysilan (APTES), and neutral hydrophilic polymer dextran, to stabilize the particles in water and enable further biochemical functionalization. While there are numerous studies exploring the impact of these coatings on cluster formation and the resulting physicochemical properties of magnetic nanoparticles [37, 38, 124, 113, 125, 40], there is a significant and known lack of details in the understanding of how exactly the particles interact magnetically inside the cluster [42, 41, 126].

As the main focus is on understanding the influence of particle size and structural organization on the magnetic properties of clusters in detail, we employed magnetometry combined with small-angle X-ray scattering (SAXS) and cryogenic transmission electron microscopy (cryo-TEM). Moreover, we utilized small-angle neutron scattering (SANS) to investigate the magnetic structure of the clustered particles within the citrate-coated system. Furthermore, a systematic study of various coating materials and their impact on the core oxidation over time was carried out using Mössbauer spectroscopy combined with magnetometry. Detailed knowledge of the aging processes of the particles is of equally large importance for officially approved quality standards, facilitating the development of more stable nanoparticles that retain their magnetic properties for extended periods of time.

The final part explores the impact of varying inter-particle distances among magnetic particles and how it influences the resultant magnetic properties using micromagnetic simulations. Through a combination of theoretical and experimental analysis, a detailed knowledge of the particle arrangement and its impact on the magnetic properties can help improve the use of clustered particle systems for medical applications by tuning the synthesis route to obtain the desired characteristics of the nanoparticle systems.

4.1. Iron Oxides 64

## 4.1 Iron Oxides

Iron oxide is known as a material with very large application potential, especially when the particle size is below 100 nm [127]. Their interesting proprieties include large saturation magnetization, superparamagnetism, and biocompatibility, making them a promising tool to use for medical applications such as drug delivery [128, 129], cancer treatment by hyperthermia [130, 131], and magnetic particle imaging [132]. Iron oxide is abundant in nature and can be found in rocks, soils, and oceans. On the other hand, producing different iron oxide phases with the control of the synthesis process is often inexpensive and relatively easy. In iron oxides, the iron ion is most commonly either divalent Fe<sup>2+</sup> or trivalent Fe<sup>3+</sup>, or in a ratio of divalent and trivalent. The most common naturally occurring iron oxides are magnetite (Fe<sub>3</sub>O<sub>4</sub>), maghemite ( $\gamma$ -Fe<sub>2</sub>O<sub>3</sub>), hematite ( $\alpha$ -Fe<sub>2</sub>O<sub>3</sub>) and wüstite (Fe<sub>1-x</sub>O), and are briefly introduced below.

Magnetite & Maghemite Magnetite (usually a black substance) possesses cubic inverse spinel structure (Fd3m spacegroup). Its unit cell and ferrimagnetic structure are shown in Fig. 4.1a. The cubic unit cell with a lattice constant of 8.396 Å contains 8 formula units with 8 Fe atoms in a tetrahedral configuration with 4 oxygen next neighbors (A-site) and 16 Fe atoms in an octahedral configuration with 6 oxygen next neighbors (B-site), i.e. a total of 24 Fe atoms. The formula unit can be characterized by  $[Fe^{3+}]_A[Fe^{3+}Fe^{2+}]_BO_4$ . The coexistence of Fe<sup>2+</sup> and Fe<sup>3+</sup> in the B sublattice leads directly to its complex magnetic properties. Since the A and B sublattices are antiferromagnetically coupled, while the Fe<sup>3+</sup> cations on each sublattice have a magnetic moment of  $5\mu_B$  with the electron configuration  $[Ar]3d^5$ , they cancel each other, so that the remaining Fe<sup>2+</sup> cation results in magnetization of  $4\mu_B$  per unit formula with the electron configuration  $[Ar]3d^6$ . Magnetite has a saturation magnetization of 87 Am<sup>2</sup>/kg at room temperature [133].

Maghemite (usually a brown-red substance) has a similar crystallographic structure to magnetite but different magnetic and electronic properties. It contains 21.33 Fe atoms, all  $Fe^{3+}$ , per formula unit, together with cation vacancies (2.67 per unit cell) at the octahedral B-sites [134]. The formula unit can be characterized by  $[Fe^{3+}]_A[Fe^{3+}_{5/3} \square_{1/3}]_BO_4$ . The presence of vacancies and the different electronic configurations are responsible for the differences in magnetic properties. Maghemite has a lower saturation magnetization of  $76 \text{ Am}^2/\text{kg}$  compared to magnetite at room temperature [133].

Hematite Hematite (usually a blood-reddish substance) is stable at ambient conditions, and it is often the end product of all temperature-induced phase transformations of other iron oxides [135]. It has a hexagonal unit cell with a = 5.034 Å and c = 13.75 Å(R-3c space group). The unit cell contains six formula units of  $\gamma$ -Fe<sub>2</sub>O<sub>3</sub> (12 Fe atoms and 18 O atoms), where O<sup>2-</sup> ions form hexagonal close-packed layers and Fe<sup>3+</sup> occupy 2/3 octahedral sites. Upon cooling below the Neel temperature ( $T_N \approx 955$  K), hematite transitions from a paramagnetic (PM) to weak ferromagnetic (FM) spin ordering is observed due to spin canting [136]. At Morin temperature  $T_{\text{Morin}} = 260$  K, hematite displays antiferromagnetic

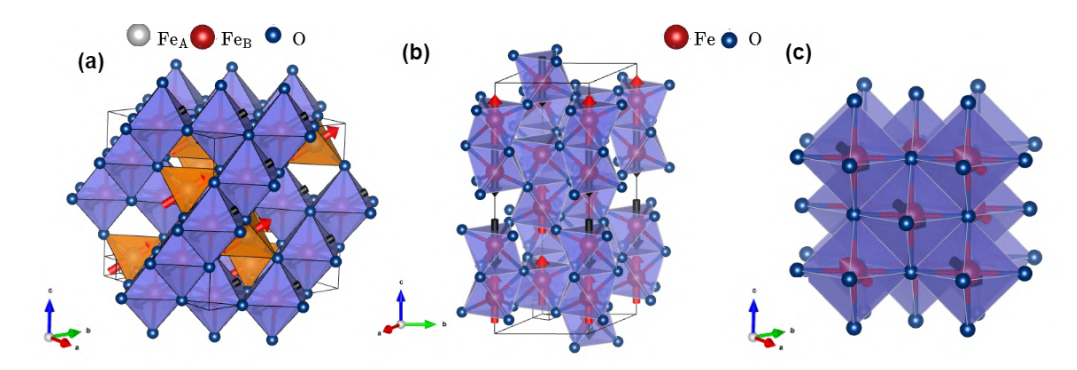


Figure 4.1: Crystalline and magnetic structure of (a) magnetite, (b) hematite, and (c) wüstite. The atomic spins in magnetite and wüstite are drawn along [111] axes.

spin ordering. Below  $T_{\text{Morin}}$ , the antiferromagnetically arranged spins are aligned coaxially to the hexagonal c-axis [137], as shown in Fig. 4.1b.

Wüstite Wüstite (usually a black substance) has a rocksalt crystal structure (group space F3m3). The unit cell consists of 4 formula units of FeO, where all Fe<sup>2+</sup> ions occupy octahedral sites of the FCC O<sup>2-</sup> lattice [27]. However, the real crystal structure is characterized by iron vacancies, which lead to a real stoichiometry of Fe<sub>1-x</sub>O with x between 0.83 and 0.96. The presence of vacancies in the structure causes the diffusion of Fe<sup>2+</sup> cations to the surface and their oxidation to Fe<sup>3+</sup>, leading to the thermodynamically unstable phase which tends to oxidize to Fe<sub>3</sub>O<sub>4</sub> by being exposed to air. Below the Neel temperature ( $T_N = 198$  K), wüstite is antiferromagnetic. The magnetic moments within the (111) plane are aligned parallel, while the neighboring moments to the (111) plane are aligned antiparallel [138], as shown in Fig. 4.1c.

# 4.2 Iron Oxide synthesis

The iron oxide particles used in this study were obtained in collaboration with the University Hospital Erlangen, Germany, and were partially synthesized by me at the University Hospital Erlangen. The route of co-precipitation synthesis was chosen for its simplicity and high yield [139, 140, 141]. Initially, a mixture of  $FeCl_2$  and  $FeCl_3$  with a 1:2 molar ratio is dissolved in distilled water and stirred under an argon atmosphere to prevent oxidation. Subsequently, an ammonia solution (25%) is added for the precipitation reaction of the iron oxide. The reaction is controlled by the temperature. Our stabilization strategy uses the following substances to provide electrostatic or steric repulsion forces: negatively charged citrate, positively charged (3-aminopropyl)triethoxysilan (APTES), and neutral hydrophilic polymer dextran. After preparation, the particles dispersed in water are sealed in containers under  $N_2$  gas for the aging study. Details of these substances are summarized below.

Citrate-coated particles (sample name C71) After the formation of the precipitate of iron oxide particles, a sodium citrate solution is added, and the resulting solution is stirred at 90°C for 30 minutes. The source of the materials used in this preparation is found in Ref. [142]. The excess sodium citrate is removed by washing the resulting particles with acetone, followed by a drying process at room temperature to obtain the nanoparticle powder. The particles are then dissolved in water and filtered through a syringe filter with 0.2  $\mu$ m-pore diameter. The molecules (Fig. 4.2(a)) have a functional carboxyl group with a high affinity for the iron oxide surface providing negative charge stabilization by electrostatic repulsion.

(3-Aminopropyl)triethoxysilan (APTES)-coated particles (sample name B47) APTES solution is added after stirring a suspension of iron oxide particles precipitate at 70°C for 15 minutes. The source of the materials used can be found in Ref. [113]. The suspension is stirred for an additional 3 h before cooling to room temperature. The particles then undergo three washing cycles with water and are then filtered using a syringe filter with 0.8  $\mu$ m-pore diameter. The nanoparticles are then dissolved in water. The pH value is adjusted to 7.4, and the suspension is stored at 4°C. Fig.4.2(b) shows the molecular structure of APTES, with the amino groups serving as anchors for functionalization [113].

Dextran-coated particles (sample name D40) Dextran solution is added to the reaction mixture before the precipitation of iron oxide nanoparticles. The mixture is then cooled  $(0-4^{\circ}C)$ , and the ammonia solution is added, forming a greenish suspension of iron hydroxide. The greenish suspension is heated to 75°C for 40 minutes, transforming to iron oxide and resulting in a change to dark brown. To remove excess ammonia and ion residues, the suspension is transferred to a dialysis bag and dialyzed against 4 L water for 24 h, changing the water five times. Subsequently, the excess dextran from the supernatant is removed by ultrafiltration in a 5430R Eppendorf centrifuge. To achieve better steric stability, the dextran coating of the particles is crosslinked by epichlorohydrin with added 5 M NaOH. The suspension of particles is filtered through a 0.22  $\mu m$  syringe filter and stored at 4°C until further use. Fig.4.2(c) represents the molecular structure of dextran. In the interaction of dextran with the SPION surface, the iron oxides have oxygen atoms or hydroxyl groups at the surface, while there no Fe atoms are in contact with the surface [143]. The interaction between the core particles and the dextran chains is based on hydrogen bonds between their surface oxides or hydroxyl groups and the hydroxyl groups of the dextran. The source of materials used for this route is found in Ref. [124]. The chemical and physical properties such as hydrodynamic diameter, polydispersity index (PDI), and Zeta potential (mV) of the C71, B47 and D40 samples are found in the Table 4.3.

Commercial iron oxide nanoparticles dispersed in water from Ocean NanoTech (SPA10-10, San Diego, USA) were used to compare the structure and magnetic properties of single-core nanoparticles with the multi-core clusters in biocompatible formulations. In the following, the single-core sample will be denoted as **SC**.

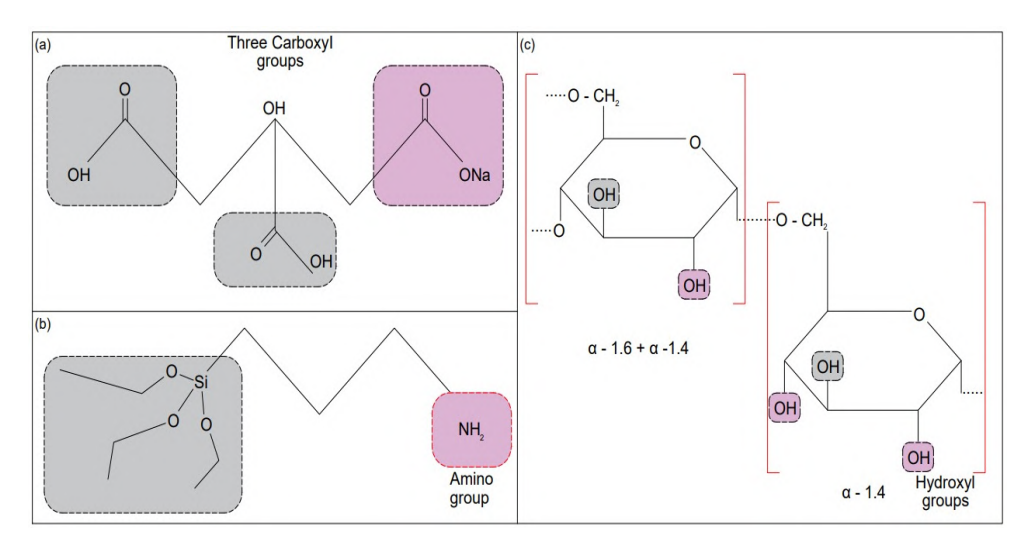


Figure 4.2: Molecular structure of the three types of coatings (a) Citrate, (b) APTES, and (c) Dextran. The gray box represents the functional groups connected to the surface of the iron oxide, while the pink box represents the functional group on the particle surface for functionalization.

Table 4.1: The hydrodynamic diameter, polydispersity index (PDI), and Zeta potential (mV) for the C71, B47, and D40 samples. Physicochemical characterization techniques were performed at the laboratory of the University Hospital Erlangen.

Coating Material	Code	Hydrodynamic Size (nm)	PDI (a.u.)	Zeta Potential (mV)
Citrate	C71	67	0.258	-49
APTES	B47	201	0.251	43
Dextran	D40	37	0.216	-4

Modified synthesis of citrate-coated samples Two citrate-coated samples were produced from iron sulfates, on a small scale (sample name C64) and on a large scale approach (sample name CU5). The chemical and physical properties such as hydrodynamic diameter, polydispersity index (PDI), and Zeta potential (mV) of citrate-coated particles from modified synthesis are presented in the Table 4.2.

# 4.3 Characterization techniques

In order to study the structural and magnetic properties, as well as the oxidation stability of the synthesized iron oxide particles, a combination of analytical techniques was employed

\ /		•		
		Hydrodynamic Size	PDI	Zeta Potential
Property	Code	(nm)	(a.u.)	(mV)
Small scale				
with $FeSO_4$	C64	44	0.219	-48
Large scale				
with FeSO <sub>4</sub>	CU5	57	0.217	-54

Table 4.2: The hydrodynamic diameter, polydispersity index (PDI), and Zeta potential (mV) of the citrate-coated particles C64 and CU5.

(see Table 4.3). Bottles 1 and 2 from the same batch were obtained, with Bottle 2 stored under nitrogen (N<sub>2</sub>) for six months after preparation to investigate the impact of storage conditions on magnetite stability. A bottle labeled A was obtained from a different batch. SANS experiments on the C71 sample were conducted on the QUOKKA instrument at ANSTO, NSW, Australia. Synchrotron X-ray powder diffraction experiments were carried out on samples C71, D40, and B47 at the material science (MS) beamline at the SESAME synchrotron, in Jordan. ASAXS experiments on sample SC were performed at the P62 beamline at PETRA III, DESY, in Hamburg. Cryo-TEM images were conducted on all samples at JCNS-4 (Forschungszentrum Jülich GmbH) with help from Dr. Marie-Sousai Appavou. Mössbauer spectroscopy was performed with the help of Dr. Joachim Landers from the University of Duisburg-Essen on samples C71, D40, B47, and SC. SAXS measurements were also conducted on all samples at the KWS-X beamline at JCNS-MLZ, Garching, Germany. Finally, SQUID magnetometry data was recorded at JCNS-2 (Forschungszentrum Jülich GmbH).

Table 4.3: List of the samples used in this thesis, indicating their storage conditions (air or nitrogen,  $N_2$ ) and the analytical techniques applied.

sample	batch	Env.	SAXS	Cryo- TEM	SQUID	XRD	Mössb.	SANS	ASAXS
	A1							X	
C71	B1	Air	X	X	X	X	X		
	B2	$N_2$					X		
B47	B1	Air	X	X	X	X	X		
D41	B2	$N_2$					X		
D40	B1	Air	X	X	X	X	X		
D40	B2	$N_2$					X		
CU5	A1	Air	X	X	X				
C64	A1	Air	X	X	X				
SC	A1	Air	X	X	X		X		X

## 4.4 Structural characterization

The mean size and size distribution of single-core nanoparticles, crystalline size, and large aggregate structures were characterized by TEM, XRD, and SAXS, respectively. Fig. 4.3 shows transmission electron microscopy images of samples C71, B47, and D40. Samples C71 (Fig. 4.3a) and B47 (Fig. 4.3b) show large aggregates of polydisperse small core nanoparticles forming raspberry-like structures, which in turn form network structures with the C71 system exhibiting less extended objects. On the other hand, the D40 sample (Fig. 4.3c) shows a different morphology with the presence of smaller particles (1-2 nm), where the dextran coating acts as a polymer matrix embedding the NPs and forming elongated aggregates. The diameter of at least 100 nanoparticles was analyzed for each sample by the ImageJ software [144]. Fig. 4.3d shows that the obtained histograms were fitted with a log-normal distribution of the general form [145]:

$$f(x) = \frac{1}{\sqrt{2\pi}\sigma x} \cdot \exp\left(-\frac{(\ln(x) - \mu)^2}{2\sigma^2}\right). \tag{4.1}$$

The fitting provides  $\mu$  and  $\sigma$  parameters of the log-normal size distribution, which can be used to calculate the diameter of the the primary particles according to

$$D_{\text{core}} = \exp\left(\mu + \frac{\sigma^2}{2}\right). \tag{4.2}$$

The crystalline structure among the cores was investigated using the X-ray diffraction (Fig. 4.4). The XRD data showed the typical peaks associated with the  $\gamma$ -Fe<sub>2</sub>O<sub>3</sub>. However, these patterns could potentially be indexed to the Fe<sub>3</sub>O<sub>4</sub> phase. The distinction between the two spinal crystal structures, such as magnetite and maghemite, using the XRD method can be challenging due to the small particle sizes leading to broad reflections. While this phase may be present in the sample, its proportion is likely tiny due to large oxidation during synthesis and preparation for measurement, indicated by Mössbauer spectroscopy (see more details in Sec. 4.6). The crystalline sizes of the building blocks (single core nanoparticles) in the studied samples were determined using the Scherrer formula [146]:

$$L = \frac{K\lambda}{\beta \cdot \cos(\theta)},\tag{4.3}$$

where L is the mean crystallite size, K is a shape factor typically taken as 0.9,  $\lambda$  is the X-ray wavelength,  $\beta$  is the full width at half maximum (FWHM) of the diffraction peak, and  $\theta$  is the Bragg angle. The values of  $\beta$  and  $\theta$  must be in radians.

The broadening of the diffraction peaks reflects the finite size of the iron oxide nanoparticles [147]. Moreover, the instrument resolution and sample inhomogeneity lead to the broadening of the Bragg peaks [148, 149]. In our case, the analysis of the three samples is based on the FWHM of the (400) Bragg peak. This particular peak was chosen because it was not influenced by the antiphase boundaries [150]. Note that the crystal size results summarized in Table 4.4 are larger than the TEM core sizes. The size distribution of

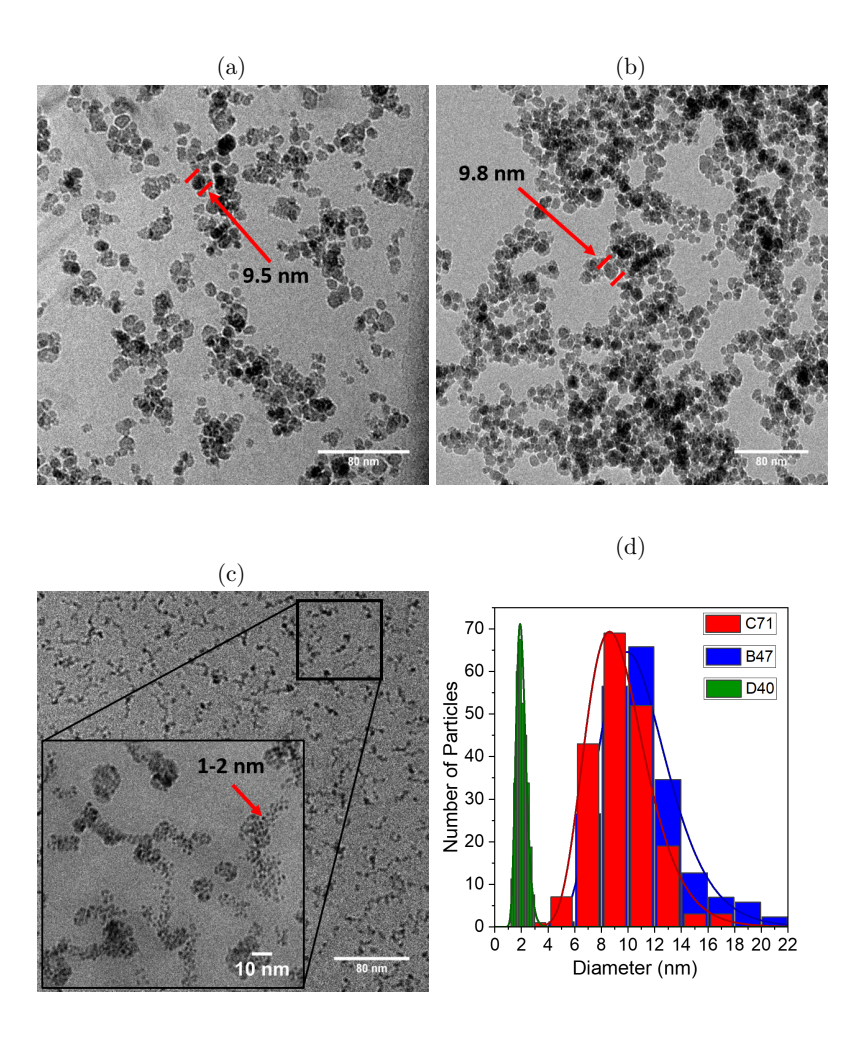


Figure 4.3: Cryo-TEM images for the (a) C71, (b) B47, (c) and D40 samples. Sub-figure (d) represents a histogram of nanoparticle size distribution with the log-normal fit for the three samples.

the nanoparticles is expected to influence the FWHM, as the larger particles of a large single crystal are dominated by scattering, resulting in the size of the crystals becoming larger [151, 152]. It is also worth mentioning that TEM allows the measurement of each individual particle, which is less statistical and more challenging for aggregated particles and a higher degree of polydispersity. Table 4.4 compares the particle size data obtained from TEM  $(D_{\rm core})$ , XRD  $(D_{\rm XRD})$ .

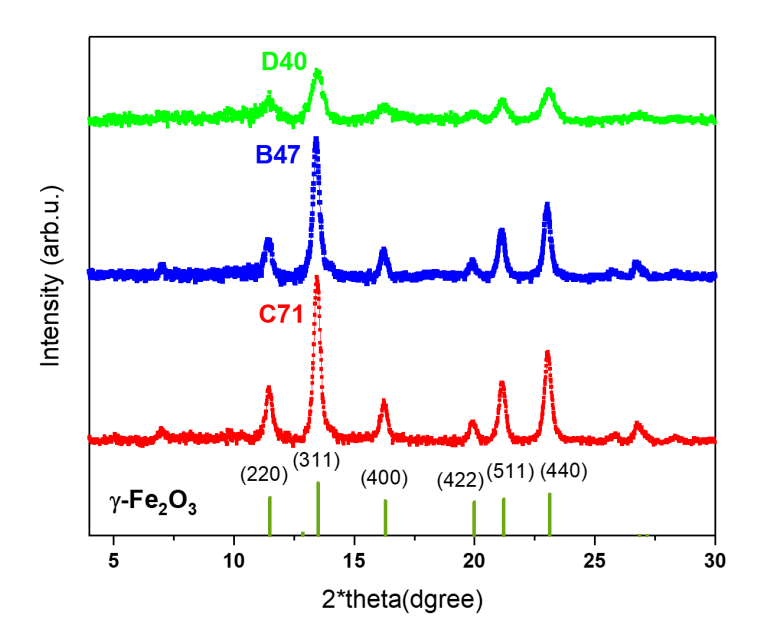


Figure 4.4: XRD pattern for samples C71 (red), B47 (blue), and D40 (green). The vertical lines at the bottom represent the most intense peaks of the cif file  $\gamma$ -Fe<sub>2</sub>O<sub>3</sub> ICSD-79196.

Table 4.4: Diameter of single particles  $D_{\text{core}}$  and  $\sigma$  of the log-normal size distribution of single cores determined by TEM, along with crystalline size  $(D_{\text{XRD}})$  for the C71, B47, and D40 samples.

Coating Material	Code	TEM	XRD	
Coating Material		$D_{\text{core}} \text{ (nm)}$	$\sigma$	$D_{\rm XRD} \ ({\rm nm})$
Citrate molecule	C71	9.5(1)	0.30(6)	10.1(5)
APTES	B47	10.7(4)	0.30(5)	11.3(7)
Dextran	D40	2.0(8)	0.20(1)	3.7(8)

To obtain size and structural information about the aggregation state of particles in the samples, SAXS intensity curves with dilution series were recorded for each sample C71 (Fig. 4.5a), D40 (Fig. 4.5b) and B47 (Fig. 4.5c). The SAXS scattering intensity of the clustered system can be described via

$$I_{\text{cluster}}(Q) = \phi V \Delta \rho^2 \tilde{P}_{\text{cluster}}(Q) S(Q), \tag{4.4}$$

where V is the cluster volume,  $\phi = nV$  is the volume fraction of cluster particles in the sample, with  $n = N/V_{\rm total}$  being the concentration of the cluster particle in the sample, and  $\Delta \rho$  is the difference in the scattering length density between the cluster particle and the solvent (contrast). The term  $\tilde{P}_{\rm cluster}(Q)$  is the normalized form factor, which describes the shape of the cluster particles, and S(Q) is the structure factor that characterizes the correlations between the cluster nanoparticles.

The SAXS curve for C71 and B47 at an initial concentration of 5.5 mg<sub>Fe</sub>/ml and for D40 at a concentration of 8 mg<sub>Fe</sub>/ml showed increased intensities in the low Q ( $Q < 0.03 \text{ Å}^{-1}$ ) indicating the presence of large objects. The dilution series is used to remove inter-cluster interactions and thus allow the appearance of the Guinier plateau, (pure form factor contribution). The structure factor, S(Q), is determined using the expression  $S(Q) = \frac{I(Q)}{P(Q)}$ , P(Q) was taken as the scattering curve for the lowest concentration. The resulting structure factor  $S(Q) \approx 1$  of the C71 and B47 sample at their initial concentrations indicate negligible inter-particle interaction. Simultaneously, the D40 sample indicates a non-negligible inter-particle interaction in the as-prepared sample (see inset in Fig. 4.5b). Simultaneously, the scattering curve of sample B47 in low Q follows a power-law intensity of  $I \simeq Q^{-2.2}$ . The power-law behaviour is consistent with the presence of larger scattering objects arising from clusters aggregation to a fractal-like structure which has been introduced in section 2.2.4 [153]. For all samples, the absence of any form factor oscillation in the high Q scattering profile ( $Q > 0.01 \text{ Å}^{-1}$ ) indicates a polydisperse particle ensemble with size and shape variation.

Since the Guinier region is accessible for scattering intensities in the diluted samples, one can make a conclusion about the dimension of the scattering particles in samples C71 and D40. For that the pair distance distribution function, P(r), was obtained using the GNOM software through the indirect Fourier transform (IFT) of the scattering intensity [154]. Fig.4.5d displays the P(r) profile for both the C71 and D40 samples (due to the stronger aggregation in the B47 sample, the corresponding IFT calculation was not possible). The P(r) represents the overall particle shape and dimension, where  $P(r = D_{max}) = 0$ . The P(r) from C71 exhibits a shape more reminiscent of spherical particles; in contrast, the P(r) of the D40 sample is closer to elongated objects.

Single-core SPIONs The TEM image of the SC sample (see Fig. 4.6a) shows no formation of agglomeration, and the particles exhibit highly monodisperse nanoparticles with a spherical shape. The particle size and size distribution were obtained by fitting the TEM histogram to a log-normal distribution function as shown in Fig. 4.6b. The fitting to the log-normal size distribution provides the particle size of the SC sample is 12.1(6) nm and the polydispersity below 20 %.

Fig. 4.7 represents the scattering intensity of the SC sample with a concentration of 5.5  $\rm mg_{Fe}/ml$  and two dilution series. The scattering curves are shifted to higher Q values compared to the curves of nanoclusters (see Fig 4.5). This indicates that the single-core structures are smaller in size. The oscillation patterns observed at higher Q are related to the small size distribution of the particles. The scattering curve of the original concentration (5.5  $\rm mg_{Fe}/ml$ ) indicates a non-negligible inter-particle interaction, as evidenced by a

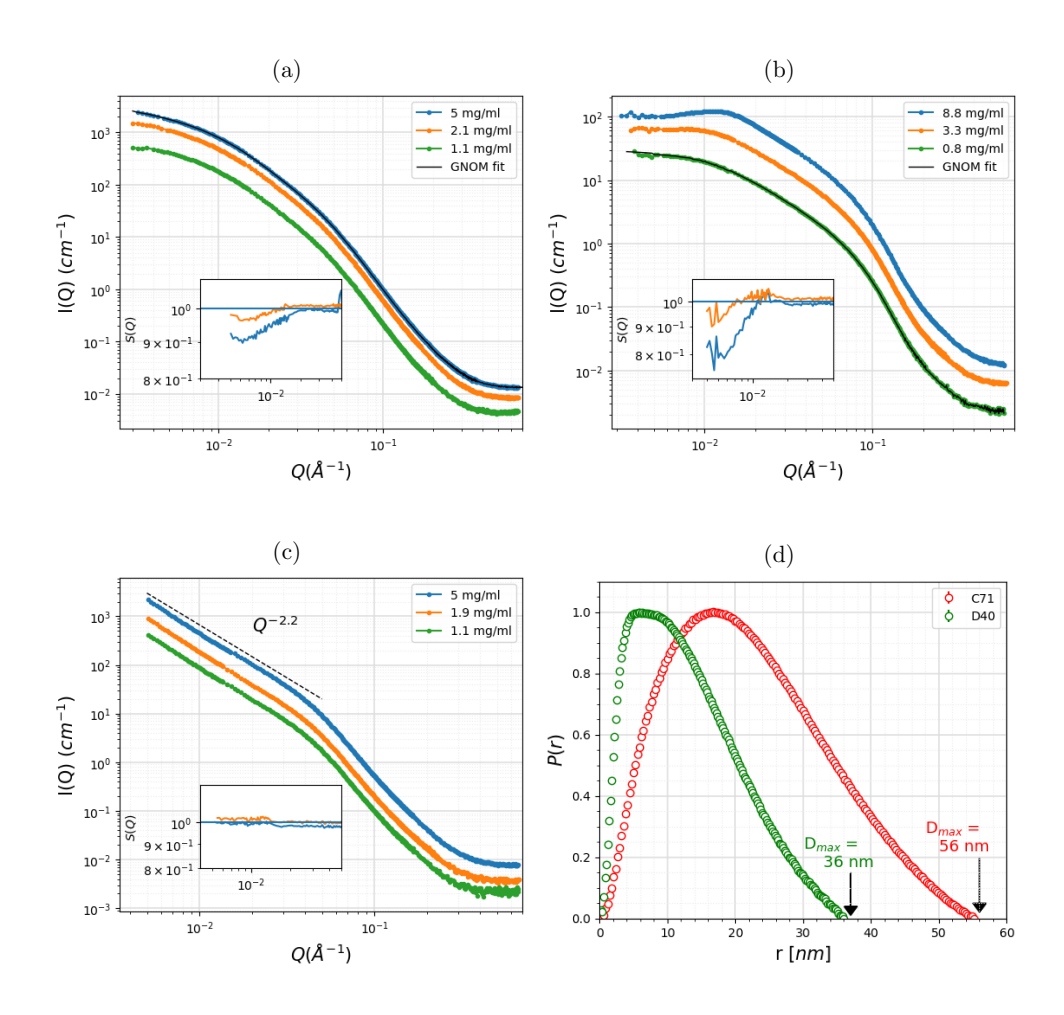


Figure 4.5: SAXS curves in dilution series for samples (a) C71, (b) D40, and (c) B47. The inset represents the structure factor, S(Q). (d) represents pair-distance distribution functions, P(r), for C71 and D40, indicating the sizes of clusters formed by the single-core nanoparticles.

peak at low Q. For single nanoparticles dispersed in water, the S(Q) could be a simple model with a hard sphere structure factor model. However, the scattering curves were fitted in the Q-range of 0.02-0.9 Å<sup>-1</sup>, where effects of the structure factor are negligible, just with a form factor of a core-shell sphere with a log-normal size distribution. The fitting yielded parameters: core radius (R=6.6 nm), standard deviation ( $\sigma=0.067$ ), and shell thickness ( $\delta R=1.66$  nm).

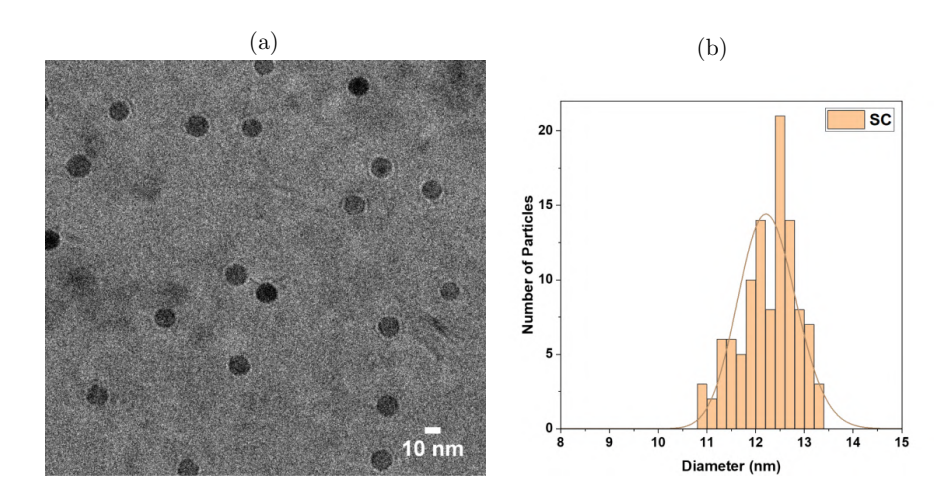


Figure 4.6: (a) A Cryo-TEM image, and (b) Size distribution fitted to a log-normal function of the SC sample.

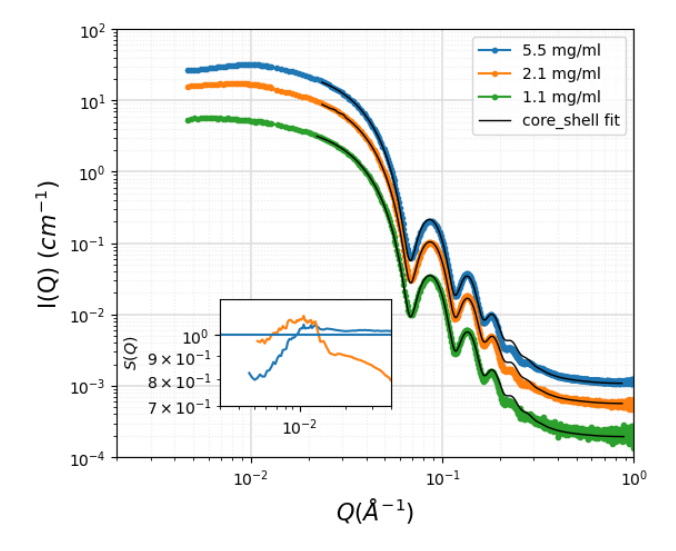


Figure 4.7: Dilution series SAXS curves for the SC sample. The inset represents the structure factor, S(Q).

Modified synthesis of citrate-coated sample Fig. 4.8a shows the SAXS curves for the C71, C64, and CU5 samples for the nanoparticle concentration of 5.5  $\rm mg_{Fe}/ml$ . The Guinier region of C64 is shifted to higher Q compared to the other samples. This indicates that the C64 sample has the smallest aggregate sizes. In the case of the CU5 sample, it exhibits a similar SAXS pattern as the C71 sample but with larger aggregate

sizes due to the Guinier region being shifted to lower Q.

It is possible to calculate the indirect Fourier transform (IFT) of the scattering intensity of the three samples due to the appearance of the Guinier plateau (Fig. 4.8b). The shape of the P(r) function with a long tail shows that the C64 sample closely resembles the one of an elongated object. The P(r) function of the he CU5 sample shows a similar shape as the C64 sample but exhibits larger aggregates. This similarity in cluster shapes but difference in size is also evident from TEM images (Fig. 4.9). Overall, the modifications in the synthesis process have led to notable changes in the particle organization among the three samples. The difference in the scale of synthesis using the same iron sulfate sources results in similar cluster shapes, with the main difference being the size of the clusters. In particular, synthesis at a larger scale (CU5 sample) results in larger clusters, while synthesis at a smaller scale (C64 sample) results in smaller clusters. The use of an iron chloride source, on the other hand, leads to more spherical objects.

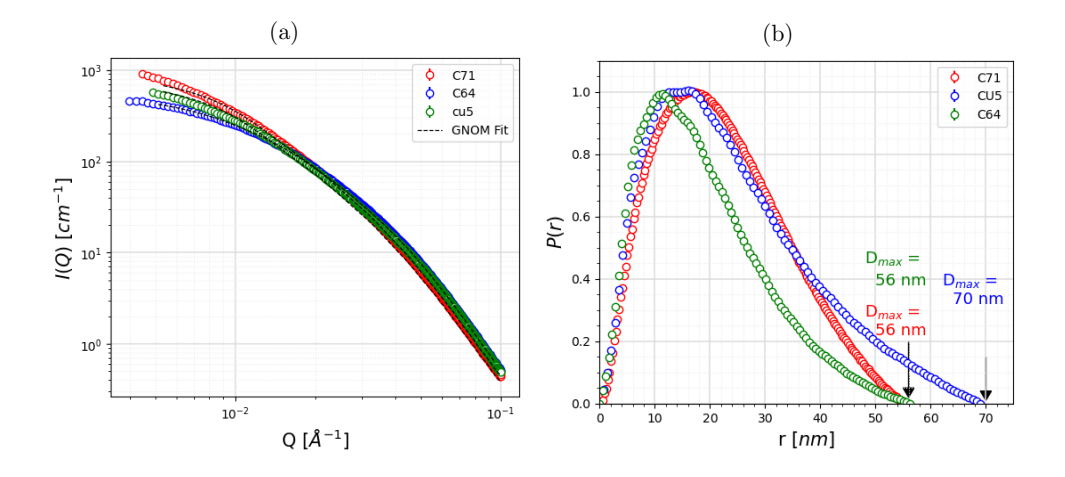


Figure 4.8: (a) SAXS curves and (b) pair-distance distribution functions P(r) for the samples C64, CU5, and C71, which is the standard sample.

#### Summary

The SAXS analysis of nanoparticles with different coatings reveals distinct structural behaviour. From SAXS, we identified the presence of clusters in each analyzed sample and determined their size and shape. Both the C71 and D40 samples are characterized by the appearance of the Guinier region at low Q values, indicating the presence of large clusters. In addition, the existence of inter-cluster interactions is observed in the B47 sample. These interactions lead to the formation of fractal-like structures. This is evidenced by the fact that the scattering intensity at low Q follows a power-law behaviour of  $I(Q) \propto Q^{-Df}$ , where Df is the fractal dimension. Additionally, the modifications in the synthesis process

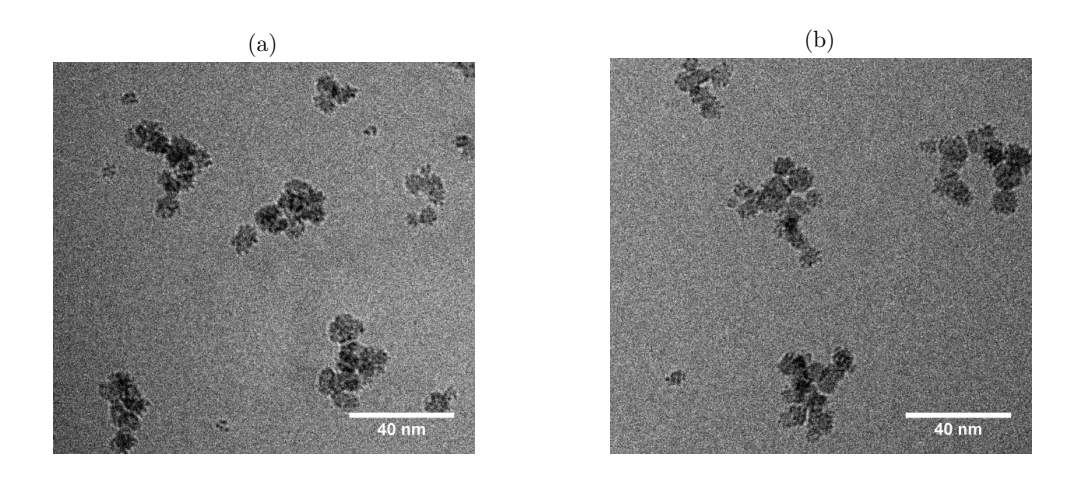


Figure 4.9: Cryo-TEM images for (a) C64 and (b) CU5 samples.

when using the same citrate coating resulted in notable differences in particle organization, with the CU5 and C64 samples exhibiting similar cluster shapes but differing in size due to the respective scale of iron sulfate synthesis. The structural information obtained from SAXS analysis is crucial for optimizing the design and synthesis of nanoparticles to achieve desired properties for future medical applications. By understanding the size, shape, distribution, and inter-particle interactions of nanoparticles, researchers can tailor their design and synthesis processes to produce nanoparticles with specific characteristics that are best suited for their intended medical applications.

# 4.5 Magnetic characterization

#### 4.5.1 Macroscopic magnetic properties

To investigate the magnetic properties of the clustered particles, field- and temperature-dependent magnetization studies were done. Isothermal magnetization data was collected in the field range of  $\pm 1.5$  T for temperatures of 5 K and 300 K. Zero field cooled (ZFC) and field cooled (FC) DC magnetization data was collected for a 5 mT magnetic field in the temperature range 5 – 225 K to avoid water melting described in section 3.2.1. The hysteresis loops at 5 K and 300 K for all samples are shown in Fig. 4.10. The hysteresis loops for the three samples are similar, with a negligible coercive field ( $\mu_0 H_c \approx 0$  T) at room temperatures, despite the large size of the aggregates, which, as expected, have a large magnetic anisotropy barrier due to the large volume of the particles. Therefore a large coercive field would be required to reverse the magnetization. When the temperature

decreases from room temperature to 5 K, the hysteresis curve opens. However, the  $H_c$  remains small with  $H_c = 300$  mT for B47,  $H_c = 29$  mT for C71, and  $H_c = 15$  mT for D40. These values suggest superparamagnetic behaviour but without the occurrence

of a single-domain state. We therefore infer collective inter-particle behaviour. The first attempt is to apply the Langevin function, including a lognormal size distribution. However, it is not possible to obtain a good fit to the experimental data using this approach. The Langevin model does not take into account the anisotropy energy of the magnetic nanoparticles. Therefore, this model is only valid for small, isotropic, and non-interacting MNP ensembles exposed to DC and slowly alternating AC fields [155]. The reduction in saturation magnetization at 300 K compared to 5 K is expected and thus due to the dominance of thermal fluctuations over the anisotropy energy. This causes fluctuations in the superspin direction, preventing them from aligning with an external magnetic field. At low temperatures, the *M-H*-loop shows the presence of either superparamagnetic blocked or ferromagnetic components discussed in section 2.1.6.2.

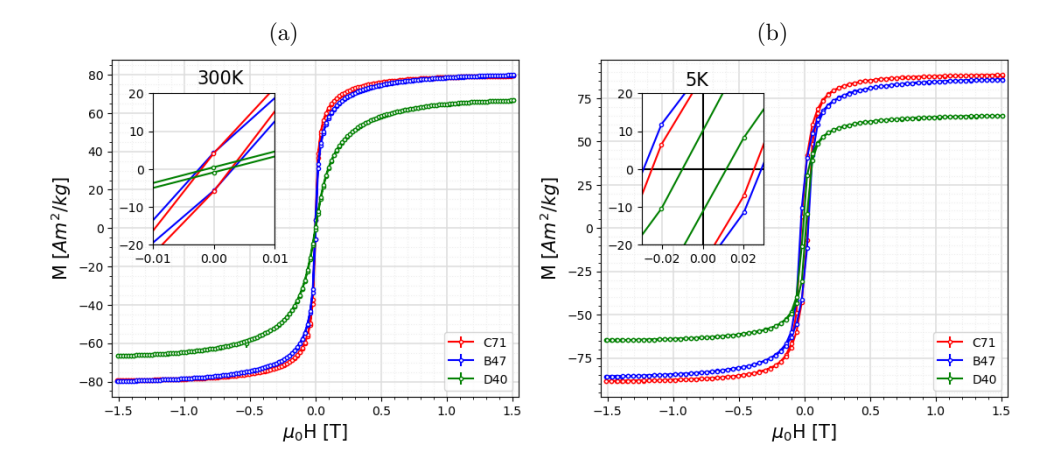


Figure 4.10: Hysteresis loops for all types of samples in the range of  $\pm 1.5$  T at (a) 300 K and (b) 5 K. The inset shows a detailed region of the hysteresis loops in the range of 0.03 T.

A detailed assessment of the magnetic properties of the clusters was conducted using ZFC/FC curves as shown in Fig. 4.11. The blocking temperature,  $T_B$ , is the temperature at which the transition occurs from the unblocked superparamagnetic to the blocked state. This transition is affected by several factors, such as particle size distribution and magnetic interparticle interactions [19, 156, 157]. Here, samples C71 and B47 have similar single-core particle sizes but differ in the organization formed by these particles. The two samples have different  $T_B$  values, with C71 having a  $T_B$  of 180 K and B47 having a  $T_B$  of 214 K. The determination of  $T_B$  is based on the highest value found in the ZFC curve. The broadening of the peaks in the ZFC curves can be attributed either to a variation of the particle volume or to strong magnetic interactions [158]. The SAXS results confirm that magnetic interaction is the main reason for the broadening featured in strongly aggregated

single-core nanoparticles. Also, the flattened shape of the FC curve provides evidence for the existence of magnetic inter-particle interactions. Sample D40 displays a  $T_B$  of about 30 K, which corresponds to the small particle sizes confirmed in TEM measurements.

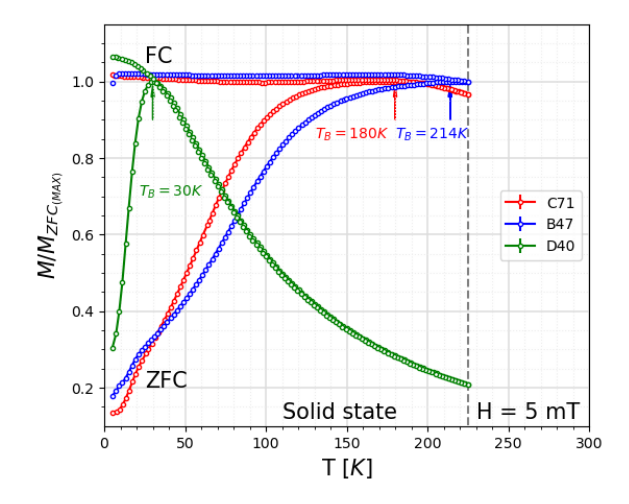


Figure 4.11: (a) Normalized ZFC/FC curves performed in the temperature range of 5-225 K and a magnetic field of 5 mT for samples C71, B47, and D40. An upper limit for the temperature is set at 225 K to avoid traversing the melting temperature of water.

A qualitative assessment of the particle size distribution can be found from the difference in temperatures between the peak position of the ZFC curve and the splitting temperature between the ZFC and FC curves. The size distribution from ZFC/FC curves inconsistent with TEM for Sample C71. The TEM image shows that the particles have a large polydispersity and also a large tendency to form aggregates. Such systems usually display the following clear signatures in ZFC/FC magnetometry curves. Firstly, the peak in the ZFC curve would be very broad. Secondly, the temperature at which a splitting between the ZFC and FC curve occurs is found at much larger temperatures than the ZFC peak temperature. The larger the difference between the ZFC peak position and the ZFC/FC splitting position is, the larger the polydispersity. Or, conversely, if the ZFC peak position and ZFC/FC splitting position match, then a highly monodisperse system can be assumed. This empirical knowledge is regularly found both in experiments and numerical simulations [18]. Based on this assessment, the SC sample exhibits a highly monodisperse behaviour and thus confirms the TEM and SAXS data (Fig. 4.12). In addition, the blocking temperature  $T_B$  of 180 K from the ZFC curve of the C71 sample would correspond to a particle size of 10 – 15 nm, which is a much smaller size of particles than obtained in SAXS. Therefore, further studies with small-angle neutron scattering are necessary to obtain the coherent magnetic size of the clusters and clarify the ZFC/FC results. The determination of the magnetic size also provides details about the magnetic structure within the clusters.

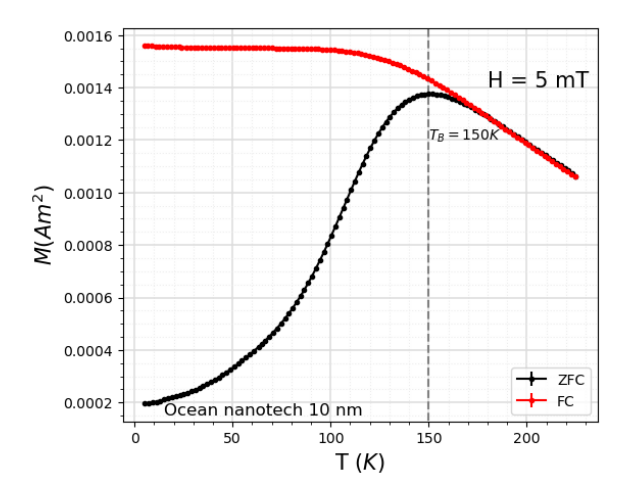


Figure 4.12: ZFC (black) and FC (red) curves as a function of temperature in the range of 5 - 225 K in the applied magnetic field of 5 mT for SC sample.

ZFC and FC curves measured at various magnetic fields are shown in Fig. 4.13. As expected, both the magnetization increases and  $T_B$  shifts to lower temperatures with increasing field strength. As a small magnetic field is applied, the magnetic moments align along the field direction, and this leads to an increase in the magnetization with increasing temperature below  $T_B$ . However, the thermal energy is enough to overcome the effective barrier height, leading to the reduction of the alignments, and thus a peak appears in the ZFC curve at  $T_B$ . As the magnetic field further increases, it leads to shifting the  $T_B$  to lower temperatures. This shift indicates that the blocking temperature depends on the applied field since the effective barrier height is reduced [61]. The thermal energy is then able to destroy the alignments at lower temperatures, effectively lowering the  $T_B$ . In the D40 sample, the peak of the ZFC curve disappears at a field of 100 mT. The Zeeman energy is therefore strong enough to overcome the anisotropy barrier. Such a pronounced dependence of the peak temperature upon the applied field in the ZFC curve is characteristic of an SPM or superspin glass (SSG) system [27].

Modified synthesis of citrate-coated samples The degree of the inter-particle interaction for the three samples was studied in temperature-dependent magnetization measurements according to ZFC-FC protocols at  $\mu_0H=5$  mT (see Fig. 4.14a). Although these samples exhibit similar single-core particle sizes as seen by TEM, they differ significantly in their structural organization. The three samples have different blocking temperatures,  $T_B$ , with C71 showing a  $T_B$  of 180 K, CU5 of 118 K, and C64 of 138 K. However, the C64 sample has a larger  $T_B$  compared to the CU5, even though C64 exhibits a smaller cluster size (56 nm) than CU5 (70 nm). This indicates that the CU5 sample demonstrates less inter-particle interaction, as evidenced by the increasing magnetization with reduced temperature in the FC curve. Furthermore, the C71 sample shows a larger

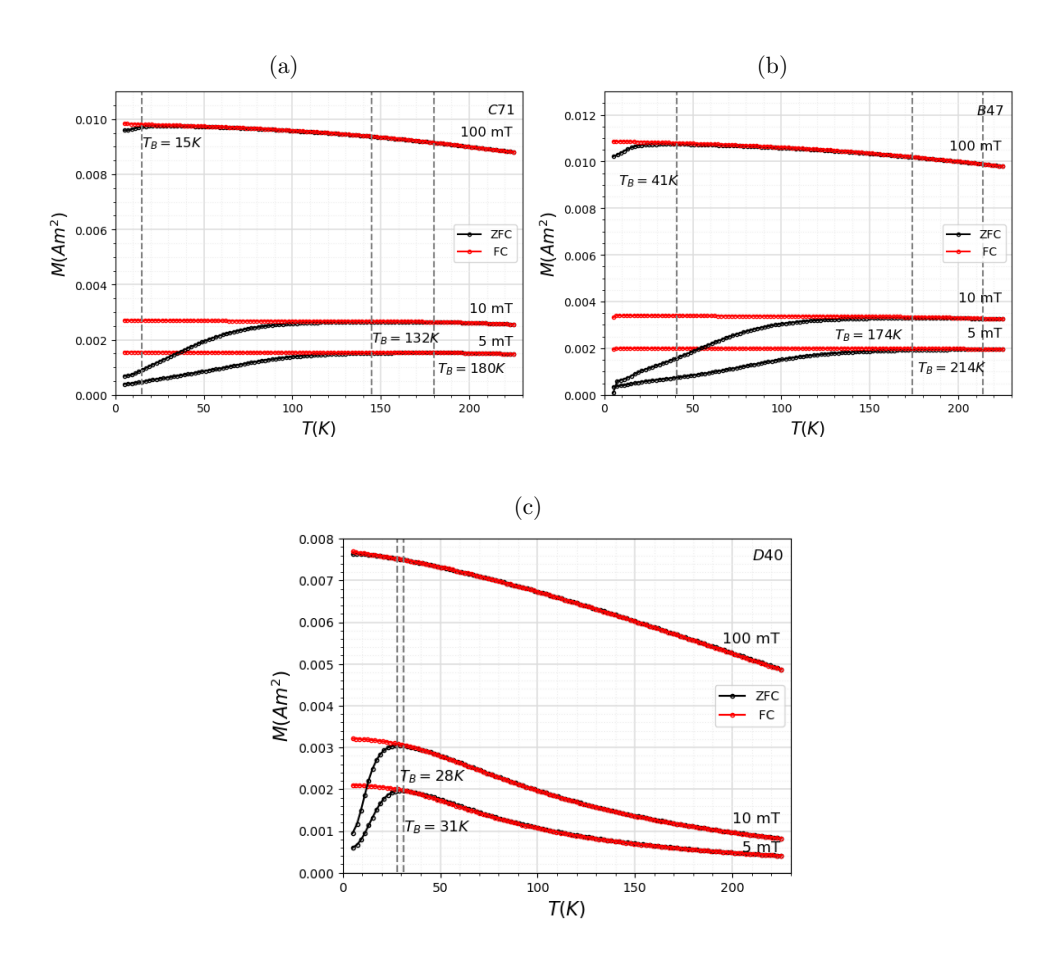


Figure 4.13: ZFC/FC curves measured at different magnetic fields 5 mT, 10 mT, and  $100~\rm mT$  for samples (a) C71 and (b) B47, and (C) D40.

blocking temperature in the ZFC curve, which suggests stronger inter-particle interactions compared to both CU5 and C64. This is further supported by more flat magnetization curves observed at lower temperatures in the FC curve. The differences in cluster size and blocking temperature among the samples indicate the importance of particle organization in determining their magnetic properties.

Magnetization curves, M(H), normalized to the Fe mass obtained from separate ICP-OES measurements and multiplied by 0.699 for maghmeite are presented in Fig. 4.14b. All samples exhibit superparamagnetic behaviour with negligible coercivity. They all show large values of  $M_s$  close to the bulk  $\gamma$ -Fe<sub>2</sub>O<sub>3</sub> (with approx. 83 emu/g at 300 K). This indicates a high degree of crystallinity in the three samples.

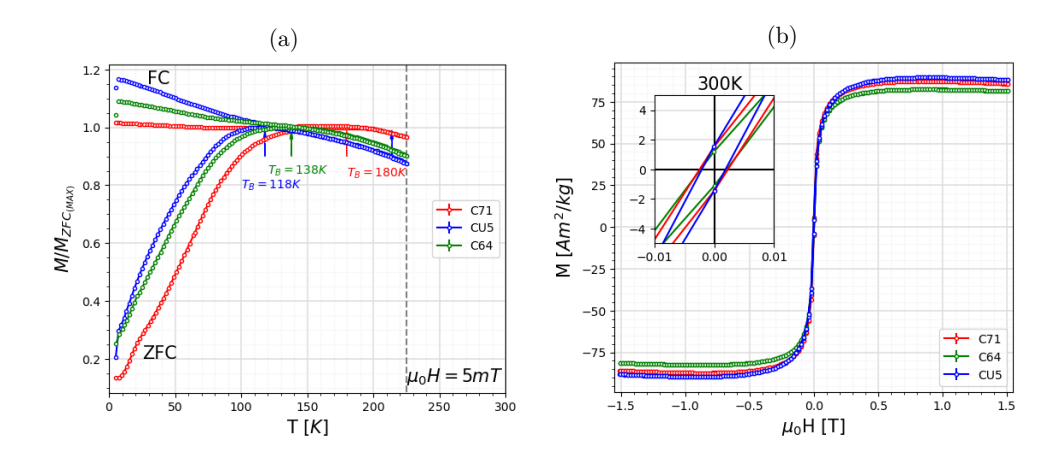


Figure 4.14: (a) M(T) curves taken in the 5 – 225 K temperature range and a magnetic field of 5 mT. (b) M(H) curves at 300 K, normalized to the amount of iron oxide present in the sample.

#### 4.5.2 Magnetic cluster size

In this section, contrast variation SANS measurements were performed to obtain additional information on the structural organization of the clustered particles. Furthermore, magnetic SANS measurements were performed to determine the magnetic size and explore the clustered particle assemblies.

#### 4.5.2.1 SANS at a zero field

The contrast variation SANS measurements in zero magnetic fields were performed to characterize the structural organization of the clustered particles, particularly in determining the average scattering length density (SLD) of clustered particles [159]. The C71 sample (citrate coating) was chosen because we found a contradiction between magnetometry and SAXS/TEM results. The SAXS results show large particles with a size of 56 nm, while the blocking temperature is  $T_B = 170$  K corresponding to the 10-15 nm. Table 4.5 represents the neutron scattering length density ( $\rho$ ) and the magnetic scattering length density ( $\rho_{mag}$ ) for the investigated components and solvents as well as their contrast,  $\Delta \rho$ , which is defined as the difference between the scattering length densities of the solvent and the component.

Fig. 4.15 displays the SANS of C71 dispersed in water with various  $D_2O$  content: from 0 to 100%. The scattering intensity is proportional to the scattering contrast. By dispersion of the particles in  $H_2O$ , due to the contrast the nuclear scattering is dominant over magnetic one. The SANS curves point to an advanced aggregation in the sample, which occurred during the period between the preparation of the contrast variation samples

Component	Density g cm <sup>-3</sup>	ρ	$ ho_{mag}$	$\Delta \rho^2 \sim \text{in H}_2 0$	$\Delta \rho^2 \sim \text{in } D_2 0$
$\gamma$ -Fe $_x$ O $_y$	4.86	6.91	0.94(2)*	55.80(1)	0.32(4)
Citrate	1.70	1.50	-	4.24(3)	23.42(5)
H <sub>2</sub> O	1.00	-0.56	-	-	-
$D_2O$	1.10	6.34	-	-	-

Table 4.5:  $\rho$  and  $\rho_{mag}$  in the unit of  $10^{-6}$  Å<sup>-2</sup> for the investigated components and solvents and their contrast  $\Delta \rho^2$  in unit of  $10^{-12}$  Å<sup>-4</sup>.

and the measurement (approximately 6 months). The SAXS curves of the fresh sample and after 6 months of preparation of the C71 sample do not show significant structural changes over time (Fig.4.16a). This is also confirmed by the similarity of the ZFC/FC curves for fresh and aged samples (Fig. 4.16b). Changing the composition from  $Fe^{2+}$  to  $Fe^{3+}$  should not significantly change the inter-particle interaction as the saturation magnetization of the samples only decreased by 8%. Therefore, we believe that the SANS data, even after 6 months of sample preparation, generally reflect the magnetic properties of the clustered particles in the C71 sample.

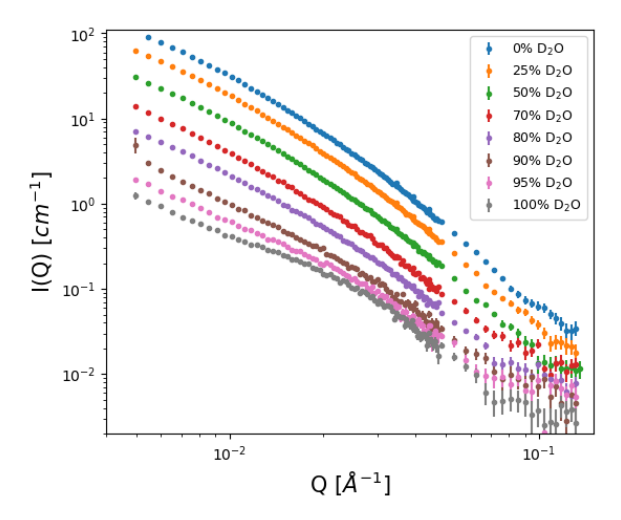


Figure 4.15: SANS intensity curves of C71 for various  $H_2O/D_2O$  mixtures.

<sup>\*</sup>The magnetic scattering length density ( $\rho_{mag}$ ) of single iron oxide core is taken from [160]. It is assumed that the value of  $\rho_{mag}$  for the cluster particles is comparable to that of the single cores.

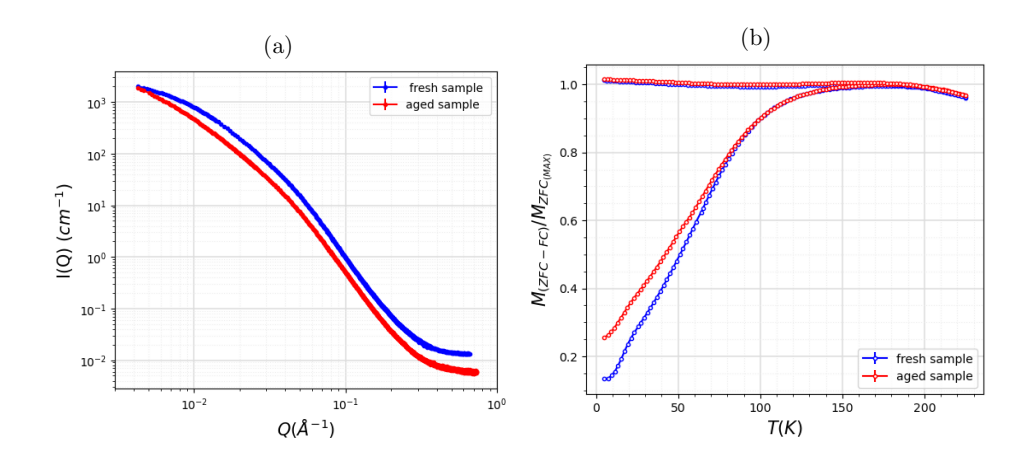


Figure 4.16: (a) SAXS curves, and (b) normalized ZFC/FC curves of the fresh sample and after 6 months from preparation for the C71 sample.

The nuclear scattering decreases gradually with increasing D<sub>2</sub>O content and reaches its minimum at 100% D<sub>2</sub>O. The scattering intensity has a quadratic dependence on the contrast and its minimum at  $Q \to 0$  called the contrast match point, gives an average particle SLD. The scattering curves of the sample with high D<sub>2</sub>O content between 0% and 80% indicate the presence of large structures, which prevents a simple Guinier analysis. Thus, we can not use the usual method of Guinier approximation and obtain the contrast dependence of  $I(Q \to 0)$ . Therefore, we determined the contrast match point at the minimum experimentally achieved Q value (see Fig. 4.17a). The curve shows the quadratic dependence of the scattering intensity as a function of the solvent contrast. The mean contrast point of the large cluster is found at  $106.31 \pm 2.5 \%$  of  $D_2O$  content, which corresponds to the neutron scattering length density ( $\rho$ ) of 6.74  $\pm$  0.16 10<sup>-6</sup> Å<sup>-2</sup>. This value is close to the SLD of iron oxide (see Table 4.5). Therefore, one can conclude that the contribution of the small citrate shell is negligible. Fig. 4.17b shows the dependence of the match point as a function of Q. The constant behaviour indicates that the cluster particles can be considered homogeneous and that the scattering length density is largely independent in the experimental low-Q range.

A clearly observable feature in the curves for a large  $D_2O$  content (above 95%) is present in the mid-Q range,  $0.02 < Q < 0.06 \,\text{Å}^{-1}$  (Fig. 4.15). Although it was not possible to fully compensate for the nuclear signal, this feature is primarily a result of the magnetic scattering associated with individual particles (or magnetic correlations between particles in the ensemble) constituting the large clusters. The scattering intensity in a zero magnetic field close to match point can be described by [161]

$$I(Q)_{H=0} = I_N(Q)|_{\Delta\rho \approx 0} + \frac{2}{3}I_M(Q).$$
 (4.5)

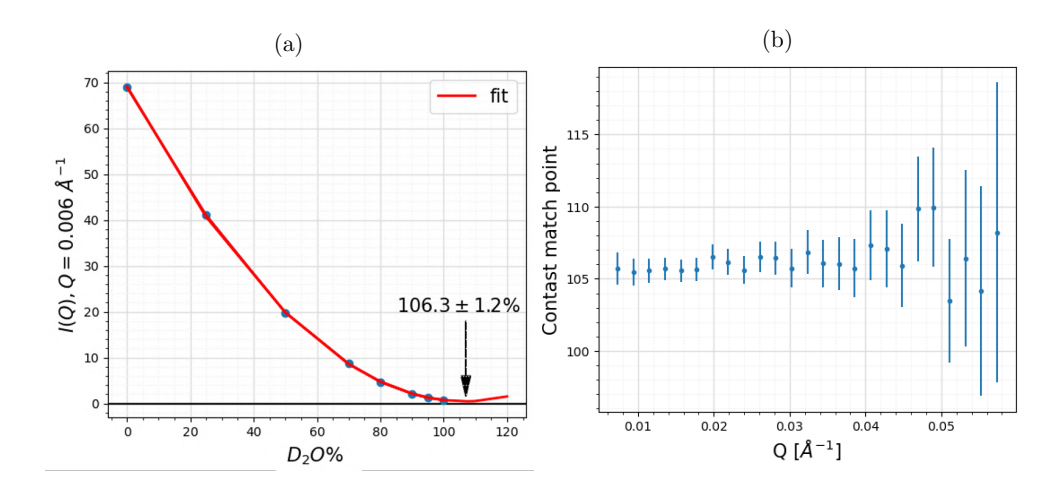


Figure 4.17: (a) The scattering intensity as a function of the  $D_2O$  content at a Q value of 0.06 Å<sup>-1</sup>. It is fitted with a parabolic curve to obtain the nuclear contrast match point. (b) The determined contrast match points as a function of Q.

It is important to note that the magnetic scattering contribution is independent of the nuclear contrast between the particle and the solvent. The use of pure H<sub>2</sub>O as solvent leads to a significant contrast between the iron oxide nanoparticles and the water. Therefore, the scattering intensity in this case results mainly from the nuclear signal, while the magnetic contribution is negligible. However, the dispersion of particles in D<sub>2</sub>O leads to a low nuclear contrast  $\Delta \rho$  (see Table 4.5). This leads to a reduction in the intensity of nuclear scattering from the cluster particles, allowing the magnetic scattering contribution to be highlighted. To separate the magnetic scattering from the residual nuclear scattering in D<sub>2</sub>O, the H<sub>2</sub>O curve was scaled down (by a factor of 131) and subtracted from the 100% D<sub>2</sub>O curve. The scaling factor is determined manually and corresponds approximately to the ratio of the particle contrasts,  $\Delta \rho^2$ , in the solvents H<sub>2</sub>O and D<sub>2</sub>O (Fig. 4.18a). Its exact determination is difficult due to uncertainties in the determination of the average SLD of the particles, as we could not observe the zero-angle scattering intensity I(0). A Guinier region in the difference curve appears as shown in Fig. 4.18b and can be attributed to magnetic spherical objects with a  $D=2\sqrt{5/3}R_q\approx 16.8\pm 0.4$  nm. This size is in agreement with the  $T_B$  obtained from the ZFC data, which corresponds to a contribution of single nanoparticles (or their magnetic correlations) in the clusters. Here, the magnetic scattering is dominated by the magnetostatic contributions [162].

In summary, we have successfully separated the magnetic scattering contribution from the nuclear scattering contribution in a zero magnetic field. The obtained magnetic scattering indicates the presence of strong magnetic interactions among the individual iron oxide nanoparticles, resulting in a larger magnetic size that is slightly greater than the size of a single nanoparticle as determined through TEM and XRD analyses.

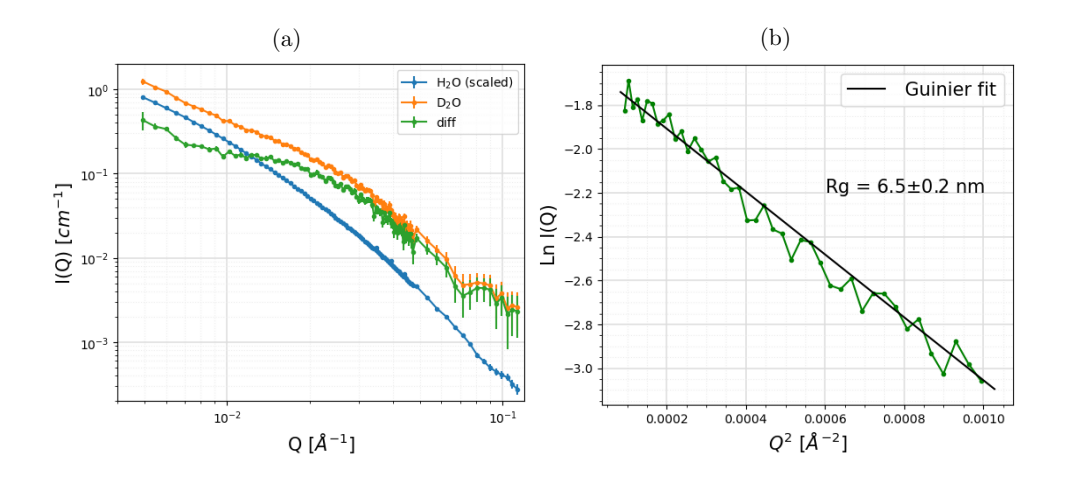


Figure 4.18: (a) Pure magnetic scattering in the  $D_2O$  sample (at zero magnetic field) as extracted by scaling the  $H_2O$  data down by a factor of 131 and then subtracting from the 100%  $D_2O$  curve. (b) The Guinier fit of the purely magnetic contribution.

#### 4.5.2.2 SANS with applied magnetic fields

Fig. 4.19 shows the two-dimensional neutron scattering patterns obtained for C71 dispersed in D<sub>2</sub>O without and with the application of external magnetic field up to 1.1 T. The aim is to determine the evolution of magnetic size with the application of external magnetic fields. At zero field, one can see the isotropic pattern and thus relate that the nuclear and magnetic scattering are isotropic. Upon application of a magnetic field above 0.11 T, the 2D SANS patterns exhibit a predictable anisotropy. This anisotropy originates from an anisotropic magnetic scattering distribution [159]. Here the nuclear scattering is much smaller compared to the magnetic scattering, as it is dependent on the contrast and the magnetic scattering is dominated by the anisotropic field-related scattering. The scattering intensity with field dependence can be expressed as [163]

$$I(Q,\theta)_{H\neq 0} = I_N(Q)|_{\Delta\rho\approx 0} + I_M(Q)\sin^2\theta, \tag{4.6}$$

$$I_M(Q) = \frac{8\pi^3}{V} b_H^2 \left| \tilde{M}_z \right|^2. \tag{4.7}$$

The quantities V,  $b_H$ ,  $\dot{M}_z$  and  $\theta$  refer to the scattering volume, a constant parameter, the Fourier transform of the z-components of the magnetization vector field and the azimuthal angle between the applied magnetic field H and the scattering vector Q, respectively. Fig. 4.20a presents the purely nuclear scattering contribution, which was obtained from the 2D scattering pattern in the sector of  $\pm 10^{\circ}$  for  $\vec{Q} \parallel \vec{H} (\sin^2 \theta \approx 0)$ , and the field-dependent

magnetic scattering contribution, which is accessible from the 2D scattering pattern in a sector of  $\pm 10^{\circ}$  for  $\vec{Q} \perp \vec{H}$  (sin<sup>2</sup>  $\theta \approx 1$ ). In the range of magnetic fields from 0 to 0.11 T, the scattering intensity is comparable for both the parallel and perpendicular sectors. However, for magnetic fields above 0.11 T, the scattering intensity decreases in the parallel sector and increases in the perpendicular sector, which is due to the redistribution of magnetic scattering during progressive sample magnetization. The pure magnetic scattering is obtained by subtracting the intensity of the perpendicular scattering (which consists of both nuclear and magnetic components) from the intensity of the parallel scattering (which consists only of nuclear components) in fields close to the saturation (see Fig. 4.20b). The appearance of a Guinier region indicates the presence of the form factor of the magnetic clusters and a negligible structure factor. Therefore, we infer no correlation between the collective magnetic moments of clusters. A Guinier fit of the magnetic scattering at 1.1 T results in a radius of gyration  $R_q \approx 13.5 \pm 0.3$  nm (diameter of the magnetic sphere  $34.8 \pm 0.8$  nm). The observed results can be attributed to the significant magnetic inter-particle interaction within the clusters, which leads to a large net magnetic size that is approximately half of the cluster size. The obtained magnetic size exhibits a multi-domain structure even in saturation. The latter result is important in obtaining nanoparticles with large magnetic susceptibility, where coherent rotation of the superspin of the primary particles within the cluster is desirable, i.e. where the superspin of the primary particles rotates in unison.

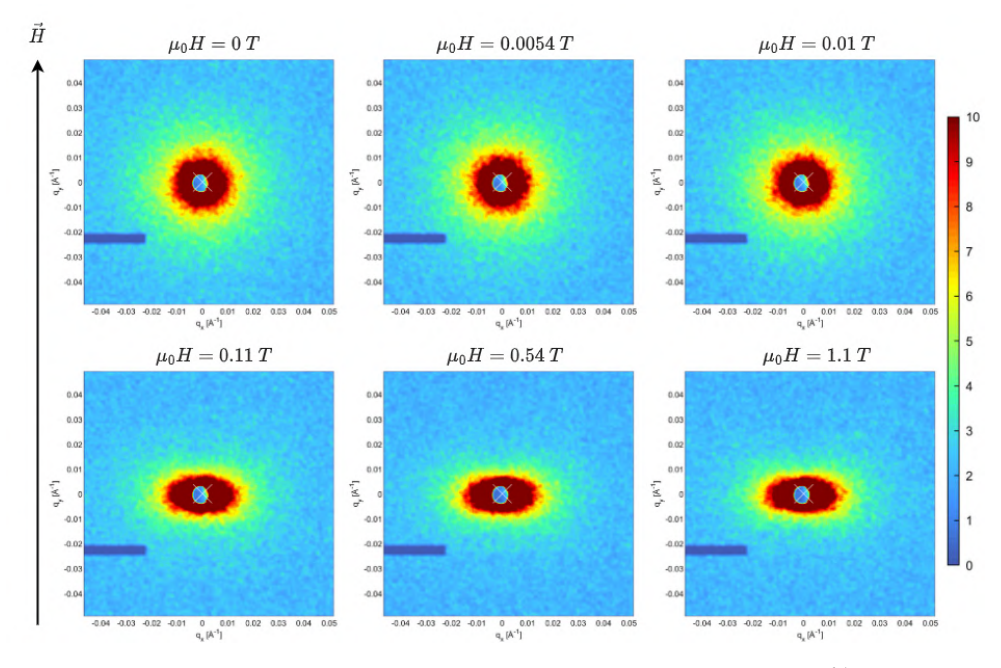


Figure 4.19: Two-dimensional unpolarized SANS patterns at small Q, for 100% D<sub>2</sub>O sample at selected applied magnetic fields from 0 up to 1.1 T applied vertically.

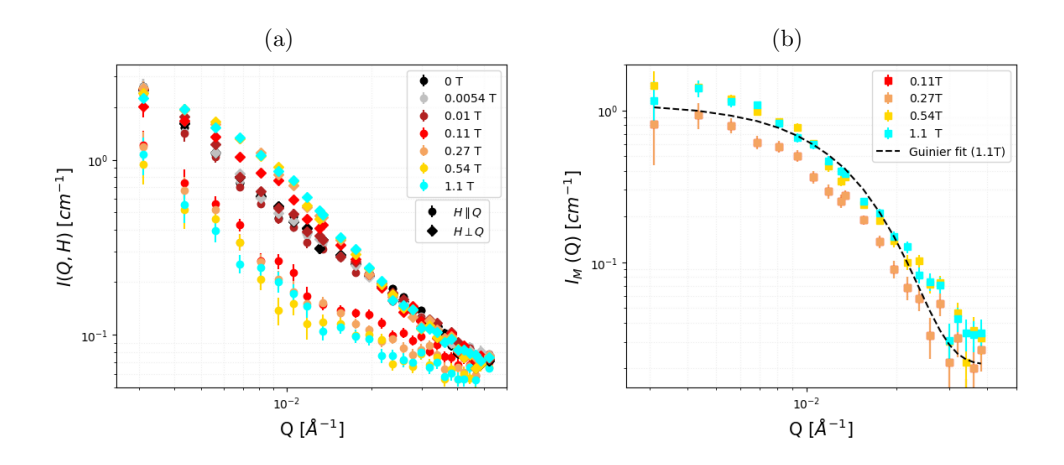


Figure 4.20: (a) Scattering intensity of sample C71 dispersion in D<sub>2</sub>O solvent in the parallel sector  $(\vec{H} \parallel \vec{Q})$  and perpendicular sector  $(\vec{H} \perp \vec{Q})$ , (b) pure magnetic scattering is determined by subtracting the intensity of the perpendicular scattering, which contains both nuclear and magnetic components, from the intensity of the parallel scattering, which contains only nuclear components, at large fields close to saturation. A Guinier fit to the magnetic scattering at 1.1 T yields a radius of gyration,  $R_q \approx 13.5 \pm 0.3$  nm.

To investigate the behaviour of cluster ensembles in the presence of an external magnetic field, field-dependent SANS measurements were performed on the particle dispersion in  $H_2O$  to highlight nuclear features. Fig. 4.21 shows the two-dimensional neutron scattering patterns obtained for C71 dispersed in  $H_2O$  in external magnetic fields range from 0 to 1.1 T. Upon applied 0.11 T, the 2D SANS patterns exhibit an elongation along the direction perpendicular to the magnetic field direction, which suggests the presence of a large orientation of the aggregates along the field or a large anisotropic magnetic scattering contribution.

Fig. 4.22a shows the sector differences for the C71 sample dispersed in  $\rm H_2O$  in an external magnetic field from 0 to 1.1 T. Without a magnetic field, the scattering intensity exhibits power-law-like scattering, indicating the presence of long-range order between the primary cluster particles. Increasing the applied field by 0.11 T leads to a decrease in intensity along the direction parallel to the magnetic field direction, and the power-law-like scattering transforms into Guinier-like scattering in parallel and perpendicular sectors. The sector difference then remains constant up to 1.1 T. This may indicate that the magnetic field has no effect on distributed cluster structure due to the field independent behaviour of the magnetic scattering at a low Q.

Fig. 4.22b shows the sector differences for selected fields close to the saturation. A Guinier fit to the magnetic scattering at 1.1 T yields a radius of gyration  $R_g \approx 11.5 \pm 0.4$  nm similar to the one obtained for D<sub>2</sub>O sample. The appearance of a Guinier region also indicates

a negligible structure factor. A possible explanation might be that cluster properties do not depend on  $\rm H_2O/D_2O$  substitution. The fact that the magnetic scattering intensity is approximately 37 times higher than that obtained in the  $\rm D_2O$  sample might indicate that during the experiment, the  $\rm D_2O$ -based sample showed more pronounced sedimentation, and thus, there was less amount of material in the beam.

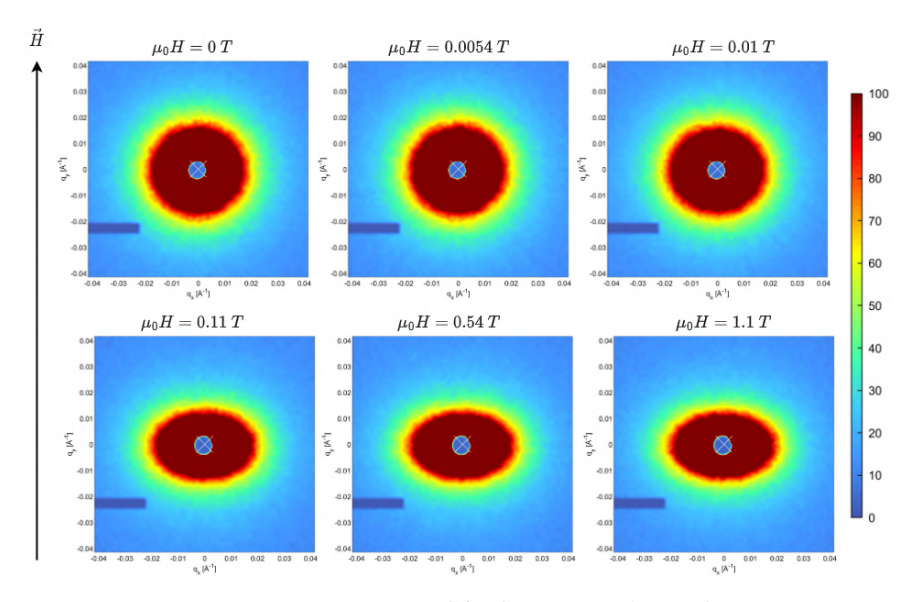


Figure 4.21: Two-dimensional unpolarized SANS patterns for  $H_2O$  sample at selected applied magnetic fields from 0 up to 1.1 T along the vertical direction.

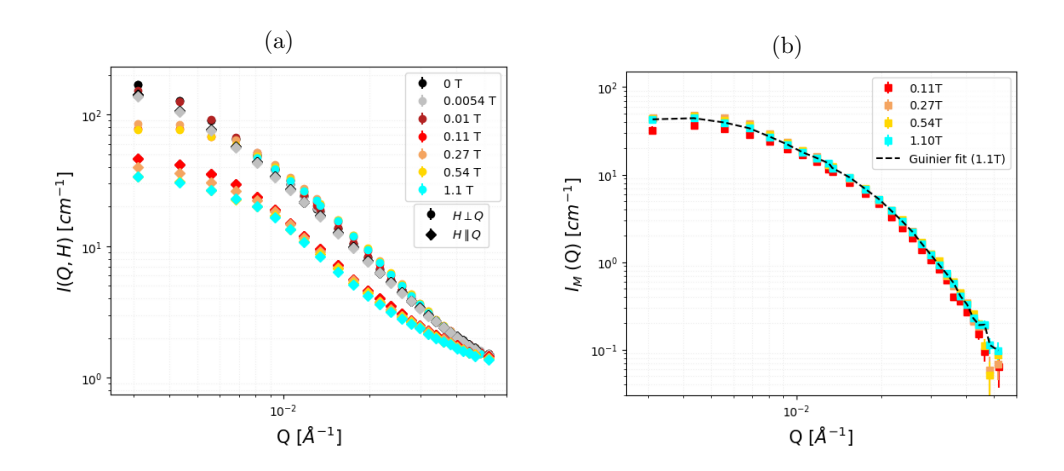


Figure 4.22: (a) Scattering intensity of sample C71 dispersion in H<sub>2</sub>O solvent in the parallel sector  $(\vec{H} \parallel \vec{Q})$  and perpendicular sector  $(\vec{H} \perp \vec{Q})$ , (b) The pure magnetic scattering at large fields close to saturation.

# 4.6 Oxidation stability

To study the aging behaviour of the nanoparticles as a function of time, Mössbauer spectroscopy and magnetometry measurements were performed on particle dispersions in water repeatedly over a time span of several weeks. The advantage of Mössbauer spectroscopy is its ability to obtain information about the nanoparticle composition with respect to the ratio of  ${\rm Fe^{3+}}$  and  ${\rm Fe^{2+}}$ , while magnetometry measurements provide macroscopic information about the net magnetic properties, which are different for different phases of iron oxides. Additionally, ASAXS was employed to study the iron oxide phases in the core/shell structure.

#### 4.6.1 Mössbauer spectroscopy

Mössbauer spectra upon aging of C71, B47, and D40 recorded at 5 K in an external magnetic field of 8 T along the propagation direction of the  $\gamma$ -rays are shown in Fig. 4.23. The Mössbauer spectra span a time interval since the synthesis and up to 37 days, with the assumption that the maximum time the particles were under ambient atmosphere between the synthesis and the first measurement is ca. 0.1 day.

As the studied material is ferrimagnetic, the dominant magnetic sublattice at the B-site will align with the applied magnetic field, while the A-site sublattice will align antiparallel to it. Consequently, the Zeeman splitting (or sextet splitting), which is similar without an applied field, will widen for the A-site and become narrower for the B-site. This change allows us to identify the fractions of A-site and B-site contributions in the Mössbauer spectra. This is one of the main reasons we apply the magnetic field during the analysis. The

spectra were reproduced via three sextet subspectra, based on their hyperfine parameters being assigned to Fe<sup>3+</sup> in tetrahedral coordination (A-site, green), Fe<sup>3+</sup> in octahedral coordination (B-site, blue) and Fe<sup>2+</sup> in octahedral coordination (B-site, violet). The ferrimagnetic structure of the particles is apparent from the resolution of the A- and B-site sublattice contributions after applying the magnetic field. Upon aging, the spectra of C71 (Fig. 4.23a) and B47 (Fig. 4.23b) show a decrease in intensity of the B-site Fe<sup>2+</sup> subspectrum, while the intensity of the corresponding Fe<sup>3+</sup> subspectrum increases, leading to more symmetrical B-site absorption lines over aging time. This is due to the shoulder formed by the B-site Fe<sup>2+</sup> subspectrum becoming less pronounced, making the oxidation from magnetite to maghemite visible to the naked eye. Notably, the initial spectra of sample D40 (Fig. 4.23c) appear to oxidize much faster to maghemite compared to the other samples since the shoulder associated with B-site Fe<sup>2+</sup> was not clearly observed. This may be attributed to smaller nanoparticle core sizes in the D40 sample.

Based on a non-zero intensity of absorption lines 2 and 5 in sample C71 (indicated with arrows in Fig. 4.23a), a canted structure for Fe<sup>3+</sup> magnetic moments with respect to the applied field can be evidenced [165]. The canting angle is defined as the angle between the direction of magnetic moment and incident  $\gamma$ -rays, with the latter here being identical to the magnetic field direction. The particles display a moderate average spin canting angle of  $\theta \simeq 14^{\circ}$ , which is determined from line intensity ratio  $A_{25}$  (see section 2.3). The C71 saturation magnetization, calculated according to the equation  $M = M_s \cos(\theta)$ , gives 93% of the saturation magnetization of 60% magnetite and 40% maghemite at 5 T after 1.1 days of aging. As discussed in section 4.1, magnetite exhibits a higher saturation magnetization of 96 Am<sup>2</sup>/kg at 0 K, whereas maghemite has a saturation magnetization of 87 Am<sup>2</sup>/kg [166].

The magnetite content can be determined for each spectrum by determining the  $Fe^{2+}$  fraction in the overall absorption spectrum (in pure magnetite it would constitute 33.3% and is 0% in pure magnetite). The magnetite content in samples C71, B47, and D40 is presented in Table 4.6.

Table 4.6: Magnetite fraction as a function of oxidation time determined from Mössbauer spectroscopy analysis. The initial state is shown after 0.1 days of exposure to the ambient atmosphere after synthesis and before the first experiment.

C71		B4	7	D40		
Aging Time	Magnetite	Aging Time	Magnetite	Aging Time	Magnetite	
(Day) (in air)	Fraction(%)	(Day) (in air)	Fraction(%)	(Day) (in air)	Fraction(%)	
0.1	$60 \pm 6$	0.1	$62.7 \pm 9.3$	0.1	$2.7 \pm 3.3$	
1.1	$41.1 \pm 6.9$	1.1	-	1.1	-	
10.1	$24.1 \pm 7.2$	9.1	$24.3 \pm 5.4$	9.1	$4.5 \pm 7.8$	
37.1	$15.3 \pm 5.4$	33.1	$17.1 \pm 7.5$	35.1	$0 \pm 2$	
114.1	-	114.1	$0.9 \pm 1.2$	114.1	-	
$252 \text{ (in N}_2\text{)}$	$16 \pm 4$	$242 \text{ (in N}_2)$	$27.7 \pm 4.5$	$249 \text{ (in N}_2)$	$0 \pm 2$	

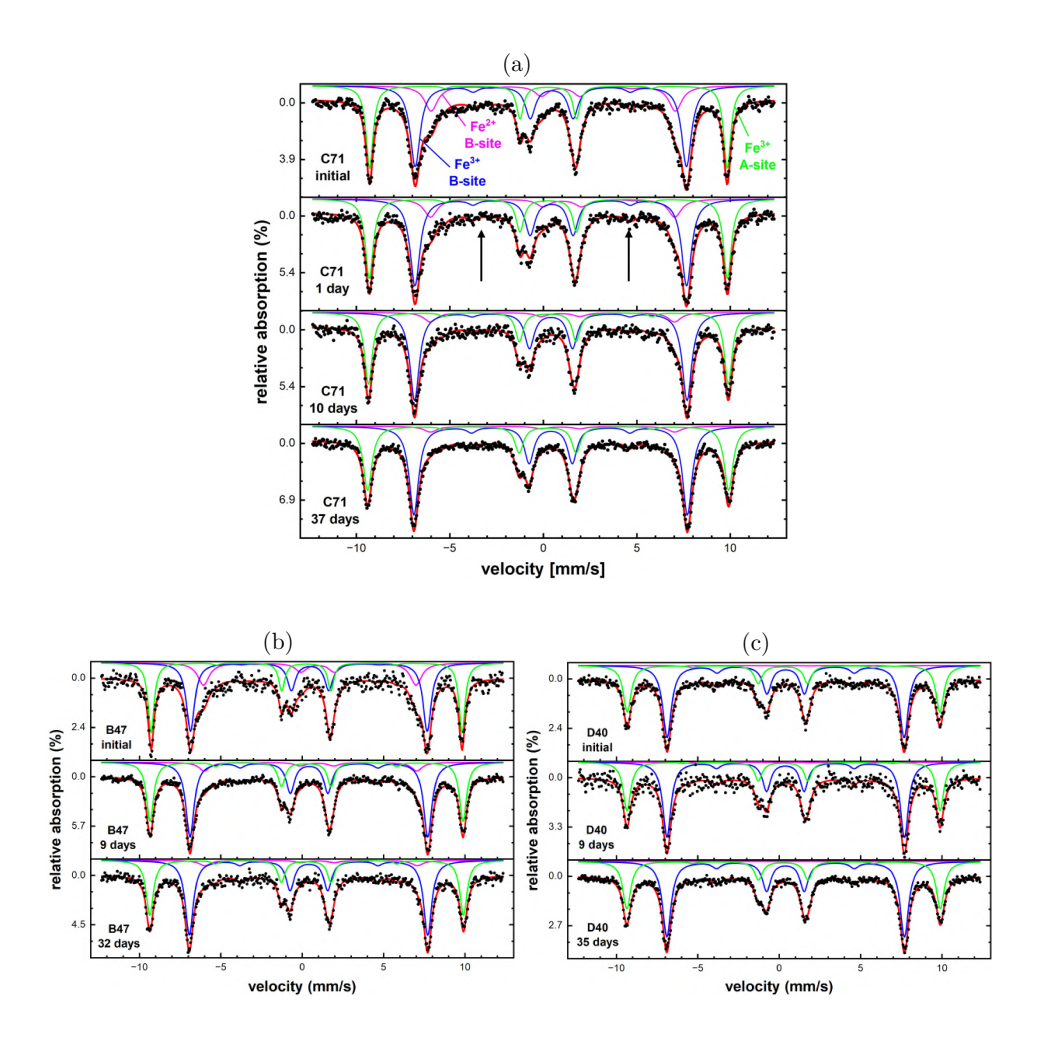


Figure 4.23: Mössbauer spectra for sample (a) C71, (b) B47, and (c) D40 after various aging times of exposure to air, recorded at 5 K and an applied magnetic field of 8 T. In the C71 1-day spectrum, the vertical arrows mark Mössbauer lines 2 and 5, whose relative intensity indicates the degree of spin canting [164]. The colors represent Fe<sup>3+</sup> in tetrahedral coordination (A-site, green), Fe<sup>3+</sup> in octahedral coordination (B-site, blue), and Fe<sup>2+</sup> in octahedral coordination (B-site, violet).

The SC sample, similar to the other samples, was studied at 5 K under an external field of 8 T (Fig. 4.24). We found that it is not easy to directly compare the spectrum to those of the three previous samples, as this sample exhibits a higher spin frustration (higher intensity of lines 2 and 5 of each subspectrum) and broadened lines. This may

originate from a poorer crystallinity, resulting in slightly different local Fe surroundings. The magnetite fraction obtained is  $\simeq 12\%$  but with a larger error margin than the three fluids in the aging study. A high-spin frustration is evident, with average spin canting angles of approximately 37°, which is translated to approximately 80% of saturation magnetization of maghine ite nanoparticles.

The 10 nm particles were prepared by the thermal decomposition method, while the previous samples were synthesized via co-precipitation methods. The observed higher spin frustration (approximately  $37^{\circ}$ ) suggests that poorer crystallinity contributes to the lower saturation magnetization ( $M_s$ ). In contrast, the particles prepared by co-precipitation methods exhibit a spin canting angle of approximately  $14^{\circ}$ . It seems that thermal decomposition is an effective technique for controlling particle size and polydispersity; however, it may lead to poorer crystallinity (or other internal defects, like antiphase boundaries) when compared to co-precipitation methods.

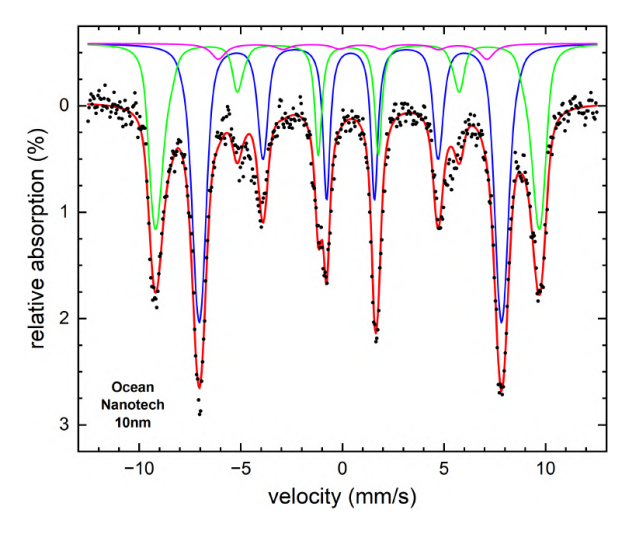


Figure 4.24: Mössbauer spectra for SC sample recorded at 5 K and an applied magnetic field of 8 T. Subspectra include A-site Fe<sup>3+</sup> (green), B-site Fe<sup>3+</sup> (blue), and B-site Fe<sup>2+</sup> (violet).

#### 4.6.2 SQUID magnetometry

A complementary approach was used to determine the net magnetic properties and confirm the oxidation kinetics. This involved analyzing the time-dependent change in saturation magnetization  $M_{sat}$ . The determined values of  $M_{sat}$  at room temperature are presented in Table 4.7. To obtain this value,  $M_{sat}$  was extrapolated from high-field magnetization data using the law of approach to saturation as described by  $M(H) = M_{sat}(1 - a/H - b/H^2)$ . The magnetite fraction is then estimated by normalizing the net magnetization to the total Fe mass and comparing it to  $M_{sat}$  for bulk magnetite, 121 Am<sup>2</sup>/kg<sub>Fe</sub>, and maghemite,

108 Am<sup>2</sup>/kg<sub>Fe</sub> [167]. In magnetite, Fe<sub>3</sub>O<sub>4</sub>, Fe constitutes 72% by molecular weight, which is larger than in maghemite,  $\gamma$ -Fe<sub>2</sub>O<sub>3</sub>, where it constitutes 70% [168]. To calculate the saturation magnetization  $M_s$  (Am<sup>2</sup>/kg), the saturation magnetization given in Am<sup>2</sup> is divided by the Fe mass obtained from separate ICP-OES measurements and multiplied by 0.72 and 0.70 for magnetite and maghemite, respectively.

Fig. 4.25 shows the magnetite fractions obtained from Mössbauer spectroscopy and magnetometry, which are in good agreement. For samples C71 and B47, the initial measurements already indicate around 40% of the particles mass oxidized immediately after a limited exposure time of less than ca. 2 hours, which corresponds to a maghemite shell thickness of ca. 0.8-1 nm around the core of nanoparticles. This would match the expectation of fast formation of a maghemite surface layer, followed by decelerated further oxidation, resulting in a remaining magnetite fraction of ca. 10–20% in both samples after one month of storage under ambient conditions. After 114 days for sample B47 only a small amount of Fe<sup>2+</sup> is detected in Mössbauer spectroscopy (see Table 4.6), indicating complete conversion to maghemite within the error margin. In contrast, sample D40 oxidized faster than the other samples, showing no considerable Fe<sup>2+</sup> component already in the initial spectrum, which is also reflected in magnetometry data. For comparison, a second batch of samples C71 and B47 was stored for six months after preparation under N<sub>2</sub>. This batch exhibited a higher stability against oxidation by preserving a magnetite fraction at the level of around 20 - 30%, which is comparable to the fraction observed after 10-30 days of exposure to air. Thus, one can conclude that sealing samples after synthesis and after flushing with N<sub>2</sub> preserves the sample saturation magnetization for a significantly longer period of time.

Table 4.7: Magnetite fraction and saturation magnetization as a function of oxidation time obtained from magnetometry.

Aging Time	C71		B47		D40	
(Day) (in air)	Magnetite	Ms	Magnetite	Ms	Magnetite	Ms
	Fraction (%)	$(Am^2/kg)$	Fraction (%)	$(\mathrm{Am^2/kg})$	Fraction (%)	$(\mathrm{Am^2/kg})$
0.1	$64 \pm 8$	$81.4 \pm 0.8$	$54 \pm 9$	$80.6 \pm 1.6$	0	$70 \pm 1$
1.1	$44 \pm 9$	$79.2 \pm 0.9$	$33 \pm 2$	$78.3 \pm 1.3$	0	$69.7 \pm 0.6$
10.1	-	-	$28 \pm 2$	$77.8 \pm 1.3$	0	$69.9 \pm 0.3$
33.1	$17 \pm 10$	$76.3 \pm 1.1$	$10 \pm 6$	$75.7 \pm 0.6$	0	$70 \pm 1$
180	$3.8 \pm 5.3$	$75.0 \pm 0.5$	0	$73.5 \pm 0.6$	0	$70 \pm 1$

The saturation magnetization determined for samples C71 and B47 is comparable to the maghemite bulk value after 180 days of aging. However, in the case of sample D40, the maximum saturation magnetization value is  $6.6 \pm 0.9\%$  lower than for bulk maghemite. This decrease in saturation magnetization may have several causes, among which are minor fitting uncertainties in the extrapolation of  $M_s$  due to the non-saturating tendency of the M(H) curve or crystal defects such as the presence of antiphase boundaries, modified atomic coordination, and an increased number of Fe vacancies [169, 160, 170, 171]. The relatively large error in the saturation magnetization is due to an inaccurate determination

of the Fe mass using ICP-OES. Treating the entire sample together with the holder might result in significant errors when determining the Fe mass.

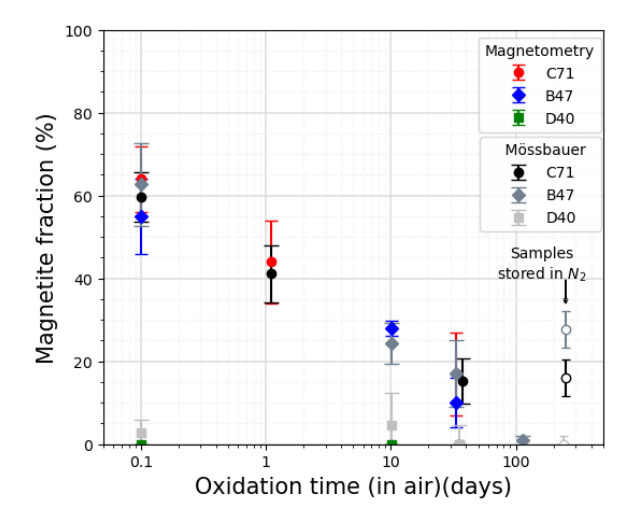


Figure 4.25: Magnetite fraction dependence on time as obtained from Mössbauer spectroscopy and magnetometry. The samples stored under  $N_2$  (empty symbols) are included for comparison.

#### 4.6.3 ASAXS

ASAXS in combination with XANES was used during annealing both in vacuum and air to provide insights into the reduction and oxidation states and to study the iron oxide phases in the core/shell structure. The magnetite nanoparticles contain both  $Fe^{2+}$  and  $Fe^{3+}$  oxidation states. As the oxidation occurs, an increasing ratio of  $Fe^{3+}$  leads to the formation of a magnetite-maghemite core-shell structure. However, during the reduction process, the amount of  $Fe^{2+}$  at the surface increases as  $Fe^{3+}$  is reduced to  $Fe^{2+}$ . The reduction first occurs at the surface and then may later lead to the migration of Fe ions into the inner part of the particles [172].

ASAXS measurements were performed on SC samples at six energies near the Fe K edge of 7112 eV, as shown in Fig. 4.26. The difference between the absorption peak for pure Fe<sup>2+</sup> and Fe<sup>3+</sup> is 1.5 eV [173]. For the Sc sample, the Mössbauer analysis indicates that the nanoparticles contain 12% of magnetite. The data show a decrease in intensity and a clear shift of the main peak to higher Q values as the energy is increased towards the Fe adsorption edge. The shift to higher Q values indicates a decrease in particle size. It is not straightforward to fit the SAXS curves due to the structure factor contribution apparent in the scattering curve. Therefore, without considering a magnetite-maghemite core-shell fitting model, the precise reasons for the observed reduction in particle sizes remain nonevidence.

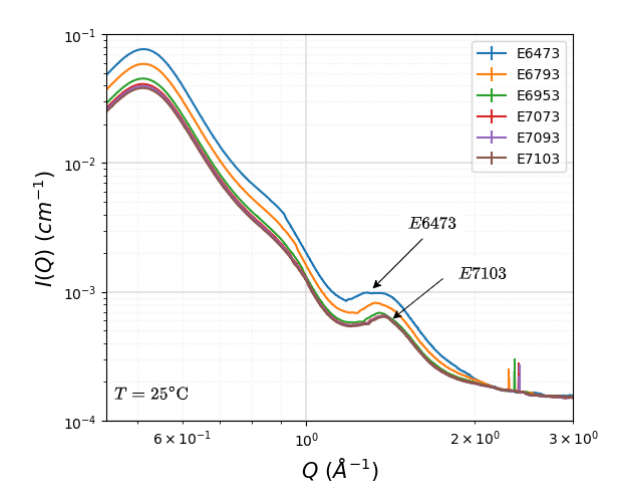


Figure 4.26: ASAXS curves were measured at six different energies around Fe K edge of 7112 eV (all below the edge) at ambient temperatures for the SC sample.

Series of SAXS data were obtained for SC samples during annealing in vacuum at two different temperatures 120°C (Fig. 4.27), and 170°C (Fig. 4.28). These SAXS data were taken at the energy 6473 eV, far from the Fe K edge. Thus, the contribution of the energy-dependent real and imaginary parts, f' and f'' can be ignored in the regular SAXS measurements. In Fig. 4.27a, the SAXS data during heating up to 120° show a clear shift of the peak corresponds to a change in the size by ca. 5 Å. It indicates changes in the structure factor i.e. we assume that at this temperature the carboxyl shell starts to melt and the particles start to mechanically reorient. Thus, it is impossible to see changes in the sizes of small particles. Also, no differences in the curves after the continuation of annealing in vacuum for 4.5 h were observed (Fig. 4.27b). The SAXS curves during heating to 170°C show that the peak shifts to higher Q. Also, a drop in intensity was found during heating up and is shown in Fig. 4.28a. This suggests that some particles were lost during the reduction process, possibly because the temperature was too large so that the carboxyl molecules were partially destroyed. A continuous reduction in intensity was also observed during the 4.5 h annealing process (Fig. 4.28b).

Fig. 4.29 shows the XANES spectra (Fe K edge) measured in transmission mode during heating and annealing of the sample in vacuum at 170°C. After heating the sample for 6 h, the absorption edge position shifts slightly to lower energies. The absorption peak for pure Fe<sup>2+</sup> differs from that of Fe<sup>3+</sup> by 1.5 eV. This shifts indicates that Fe<sup>3+</sup> is reduced towards Fe<sup>2+</sup>, i.e. maghemite is reduced towards magnetite.

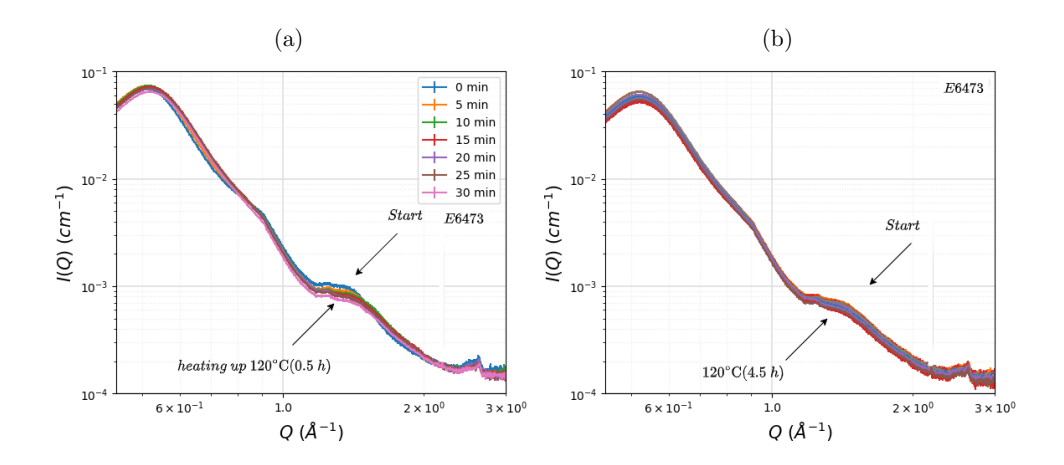


Figure 4.27: In situ SAXS curves measured (a) during heating up, and (b) during annealing in vacuum for 4.5 h at 120°C. The arrows indicate the starting of the annealing process at certain temperatures and the final measurement after 4.5 h of annealing in a vacuum.

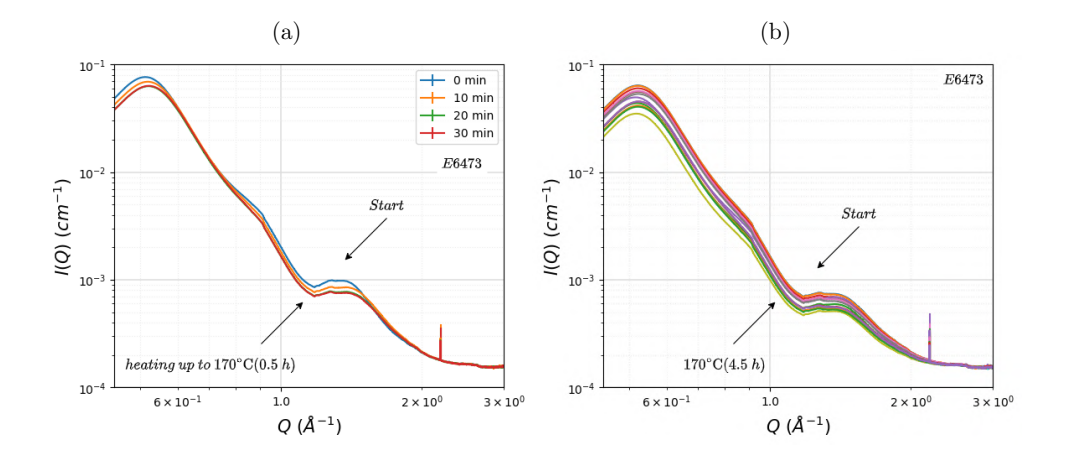


Figure 4.28: In situ SAXS curves measured (a) during heating up, and (b) during annealing in vacuum for 4.5 h at 170°C.

Fig. 4.30 represents the in situ SAXS curves obtained during annealing in air at different temperatures: (a) 80°C and (b) 120°C. At 80°C (Fig. 4.30a), the SAXS curves do not show any changes, indicating a stable structure of the nanoparticles during oxidation at this lower temperature. In contrast, at 120°C (Fig. 4.30b), the features at 0.5 and 1.5  $\text{Å}^{-1}$  in the SAXS data are shifted to lower Q. This shift is minimal, suggesting that the

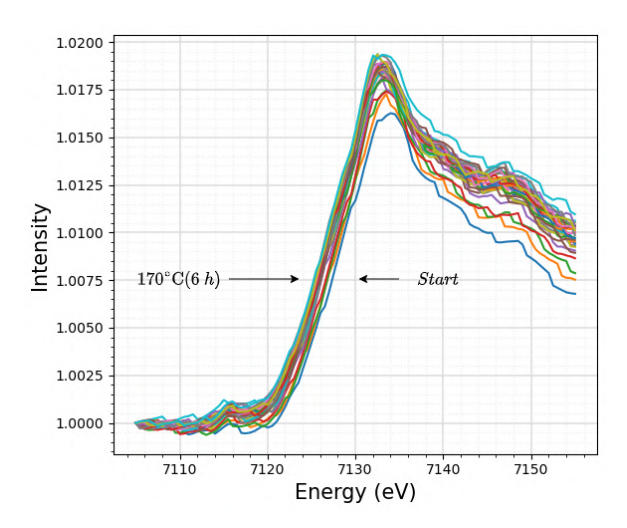


Figure 4.29: XANES data (Fe K-edge) during heating and annealing in vacuum at 170°C.

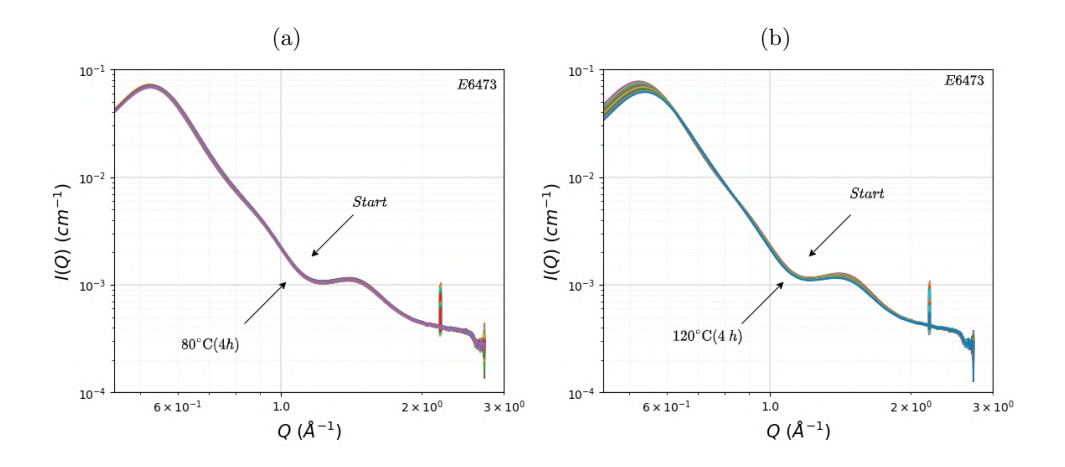


Figure 4.30: In situ SAXS curves measured at (a) 80°C and (b) 120°C.

increase in particle size is very small, i.e. approximately few Å. This change cannot be attributed to agglomeration, as the particles would be much larger in this case. It could be due to the oxidation of magnetite, where Fe ions migrate to the surface and then combine with oxygen to form a film of maghemite, leading to an overall increase in particle size. It could also be due to changes related to the expansion of the lattice under high temperature [174].

The XANES data (Fig. 4.31) show no obvious changes in the absorption edge. A small shift of about 0.5-1 eV was found when the last XANES from the vacuum was compared

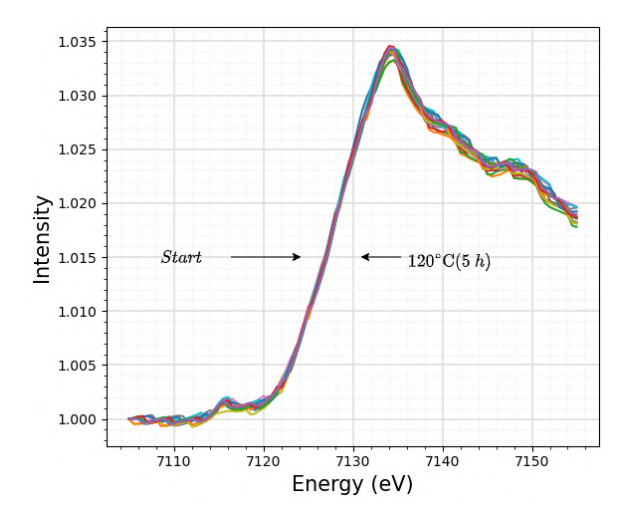


Figure 4.31: XANES data (Fe K-edge) during annealing in air at 120°.

with the first from the air. It appears that the oxidation kinetics were missed in this high temperature.

### 4.7 Micromagnetic simulations

To gain a deeper understanding of the internal magnetic structure of the iron oxide nanoparticle clusters, micromagnetic simulations first on spherical single iron oxide nanoparticles were performed. This involves studying the hysteresis curves as well as the temperature dependence of magnetization according to the zero-field-cooled (ZFC) and field-cooled (FC) protocols. The next step was to investigate the effect of exchange and dipole inter-particle interactions onto the magnetic properties of pairs of spherical nanoparticles. Then, finally simulations of clusters of several spherical particles, which are randomly connected and randomly arranged, and hence resembling the clusters in sample C71 were performed. Micromagnetic simulations were carried out using the object-oriented micromagnetic framework (OOMMF) software from NIST [102].

#### 4.7.1 Single Iron Oxide nanospheres

#### Domain structure

The magnetization structure of magnetite nanoparticles was investigated. We used a spherical model with diameters ranging from 50 nm to 100 nm. The material parameters of Fe<sub>3</sub>O<sub>4</sub> used in the simulation, including the saturation magnetization,  $M_s$ , the exchange stiffness, A, and the anisotropy constant, K are found in Table 4.8 [175, 176]. The cell sizes used in this simulation are  $2.5 \times 2.5 \times 2.5 \text{ nm}^3$ , which is smaller than the exchange length in this material,  $l_{\text{exc}} = \sqrt{A}/M_s = 8 \text{ nm}$  to ensure a correct simulation approach. For

a quantitatively correct numerical simulation, the cell size should always be smaller than the characteristic physical length scales, in this case, the exchange length. The damping parameter  $\alpha$  is set to a relatively large, but usually used, value of 0.5 because no dynamical behaviour is of interest in this study. A random initial magnetization alignment was applied without an external magnetic field. After reaching the ground state, the resulting magnetization structures were observed, which can appear as either single-domain (SD) or multi-domain (MD) configurations.

Fig. 4.32 shows a 3D representation of the domain structure in a spherical particle with a diameter ranging from D=55 nm to D=100 nm. Up to D=65 nm, the magnetization distribution is uniform and exhibits a single domain (SD) structure. However, at D=70 nm, the magnetization becomes inhomogeneous, resulting in a multi-domain (MD) structure. It displays a complex structure with a curling arrangement with in-plane (x–z plane) and out-of-plane (y-axis) configurations. The domain structure at D=100 nm shows a multi-domain structure, but with a vortex micromagnetic state, a circular magnetization arrangement [177]. The orientation of the vortex core with low anisotropy is perpendicular to the y-axis (easy-axis) with in-plane curling, which is normally found in the case of uniaxial anisotropy [178].

For each diameter, the exchange and demagnetization energies are shown in Fig. 4.33. In the SD region, the demagnetization energy is dominant, while in the MD region, this is the exchange energy that prevails the demagnetization one. It is observed that the transition from SD to MD structure is marked by a decrease in the demagnetization energy with a simultaneous increase in the exchange energy. As discussed in section 2.1.6.1, the gain of demagnetization energy has to be compensated by additional exchange energy of the extra domain wall. This transition occurs approximately at critical diameter  $D_c = 67 - 69$  nm. The demagnetization energy in the vortex state is very small, as expected, for this nearly completely demagnetized and hence flux-closed magnetization structure.

Table 4.8:  $M_s$ , A, and K simulation parameters for Fe<sub>3</sub>O<sub>4</sub> materials with single-domain (SD), multi-domain (MD), and transition to MD state at critical diameter  $D_c$ .

	$M_s$	K	A	$l_{ m exc}$	SD	MD	$D_c$
Material Type	(A/m)	$(J/m^3)$	(J/m)	(nm)	(nm)	(nm)	(nm)
Fe <sub>3</sub> O <sub>4</sub>	$5 \times 10^{5}$	$1.3 \times 10^{4}$	$12 \times 10^{-12}$	8	$\leq 65$	$\geq 70$	67-69

#### Hysteresis curves

A single sphere of iron oxide was simulated, consisting of 90% of maghemite and 10% of magnetite. This iron oxide composition was chosen to match the phases present in the C71 sample after one month of aging, as confirmed by Mössbauer spectroscopy and magnetometry. The simulation parameters were fixed to saturation magnetization,  $M_s = 4.3 \times 10^5 \text{ J/m}$ , exchange constant,  $A = 7 \times 10^{-12} \text{ A/m}$  and average anisotropy constant,  $K = 0.8 \times 10^4 \text{ J/m}^3$ . The selected cell size lengths for the simulation were

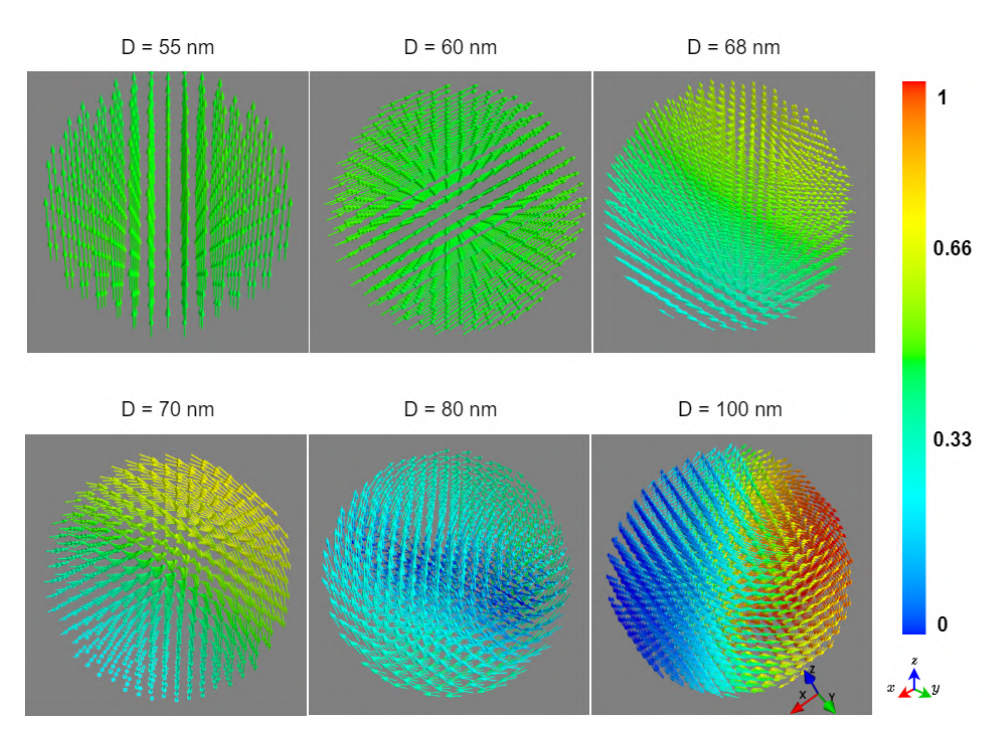


Figure 4.32: 3D representation of magnetization distribution in the ground state of Fe<sub>3</sub>O<sub>4</sub> nanoparticles with diameters range from D=55 nm to D=100 nm. The color bar indicates the  $M_{\nu}$  component of the magnetization.

 $1 \times 1 \times 1$  nm<sup>3</sup> to resolve geometry better. It was found that calculated properties such as average magnetization and relaxation time are independent of cell size when the cell size is smaller than the thermal exchange length [179].

Fig. 4.34 represents the hysteresis loop in the field range of  $\pm 100$  mT in 4 mT steps, simulated for spherical nanoparticles with diameter 10 nm in various orientations of the easy axis relative to the external magnetic field applied along the y-axis. Directional averaging was performed by simulating the same nanoparticle with 15 random orientations of the anisotropy easy axes, spanning between  $\theta=0$  and  $\theta=90^\circ$  relative to the direction of the magnetic field. The average magnetization,  $\langle M(H) \rangle$ , was then calculated. This approach allows the results to be comparable to experimental measurements, as only randomly oriented particles were studied.

For  $\theta = 0^{\circ}$ , starting from positive saturation, the magnetization is trapped along the easy axes until a large reverse field is applied,  $-H_c = -(2K/M_s)$ . In this case, the coercivity equals the anisotropy field  $H_c$ , and the magnetization will then reverse by a coherent rotation in the opposite direction. This process leads to a square-shaped hysteresis with large coercivity and completely irreversible magnetization switching.

For the hard axis ( $\theta = 90^{\circ}$ ), the complete alignment of the magnetization parallel to the

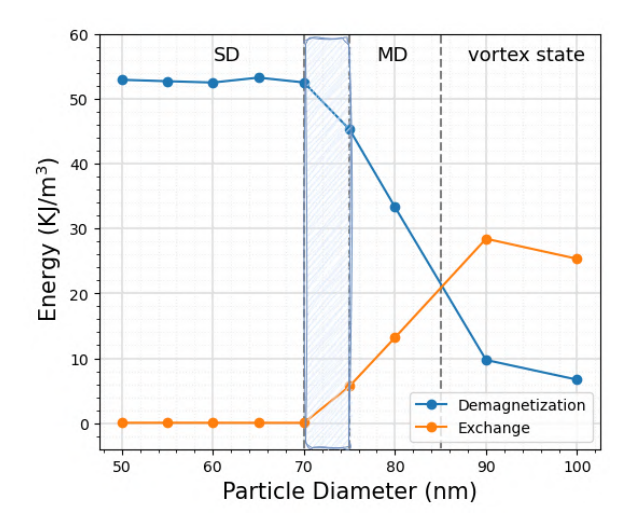


Figure 4.33: Competition between the energy of the demagnetization field and the energy of the exchange interaction for a spherical  $Fe_3O_4$  nanoparticle as a function of particle diameter at different domain structures. The gray area represents the transition of domain structure from SD to MD, which occurs approximately between 67-79 nm.

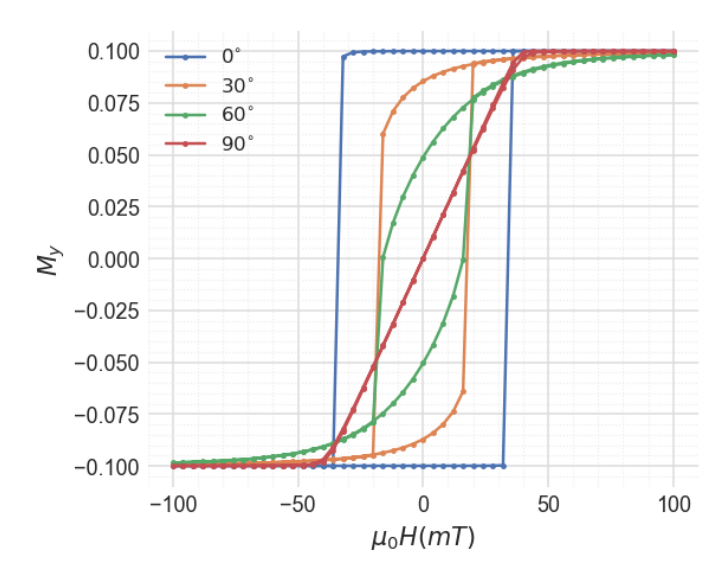


Figure 4.34: Field-dependent magnetization curves in the field range of  $\pm 100$  mT, at different angles of the easy axis relative to the applied magnetic field direction (y-axis).

field is achieved only when the applied field is larger than the anisotropy field. In smaller fields, the magnetization component parallel to the applied field,  $M_{\parallel}$ , increases linearly from 0 to  $M_s$ . It indicates that the magnetization only rotates with the applied field. Under these conditions, a hysteresis loop opening is not observed, and the magnetization behaviour is completely reversible.

For  $\theta=30^\circ$  the orientation of the easy axes is toward an arbitrary direction to the magnetic field. In this case, the magnetization reversal process consists of both reversible and irreversible processes. The magnetization at the saturation field aligns fully with the saturation field. As the field is reduced to zero, the magnetization exhibits both irreversible and reversible rotations away from the field direction and aligns towards the easy axes. Quantitatively similar behaviour is observed for larger  $\theta$ , such as in the case of  $\theta=60^\circ$ , with a decrease in remanence from 0.087 to 0.05.

Fig. 4.35 represents the resulting average magnetization,  $\langle M(H) \rangle$ , of randomly oriented MNPs. Here, the shape of the hysteresis loop is determined by the magnetic anisotropy energy i.e. it follows the classical Stoner-Wohlfarth model with uniaxial anisotropy [180]. The hysteresis has a rectangular loop with a coercivity  $H_c = 25$  mT and remanence  $M_r/M_s = 0.62$  for nanoparticles with random orientation of the easy axes.

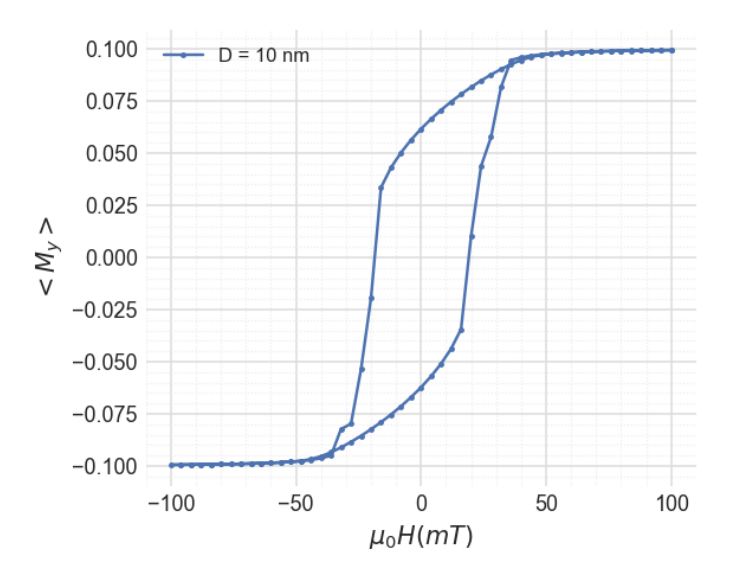


Figure 4.35: Average field-dependent magnetization curve,  $\langle M(H) \rangle$  simulated for a spherical iron oxide nanoparticles with a diameter of 10 nm.

#### Magnetic superspin blocking

ZFC and FC curves of a single iron oxide nanoparticles with 12 easy axis orientation were simulated. The simulation time used was  $3\times10^{-11}$  s with a time step of  $1\times10^{-15}$  s. For the simulation, a random magnetization orientation was first set in the absence of an

external magnetic field ( $\mu_0 H = 0$  mT). Next, a sweep over the temperature range from 0 K to 300 K was simulated in steps of 10 K while applying an external magnetic field  $\mu_0 H = 5$  mT. This enables the simulation of a ZFC curve. Without changing the applied field, the sample was subsequently cooled from 300 K to 0 K in 10 K steps to simulate a FC curve.

Fig. 4.36 represents the average ZFC and FC magnetization curves of a single nanoparticle at  $\mu_0 H = 5$  mT. Both the ZFC and FC curves show similar behaviour typical of single-core nanoparticles. The peak temperature at  $\approx 130$  K in the ZFC curve indicates the point above which the nanoparticles are in the unblocked superparamagnetic state. Above the peak temperature, the ZFC and FC magnetization curves split. The close vicinity of the positions of the ZFC peak and the splitting between the ZFC and FC curves suggests a monodisperse system as expected. However, a significant decrease in the magnetization above  $T_B$  was not observed. In the next section, the effect of interparticle interaction on magnetic blocking will be studied.

Fig. 4.37 presents the snapshot of magnetic moments direction below and above the blocking temperature,  $T_B$ , in an external magnetic field of 5 mT applied along the y-axis. For  $T < T_B$ , the magnetic moments appear blocked (or frozen) in a certain direction, resulting in no net alignment along the field direction at T=0 K. However, at T=50 K, temperature is gradually destroying the alignment of magnetic moments, and thus, the applied magnetic field can induce some net alignment of the moments in its direction. For  $T>T_B$ , the thermal energy overcomes the effective energy barrier leading to a crossover to an unblocked superparamagnetic state.

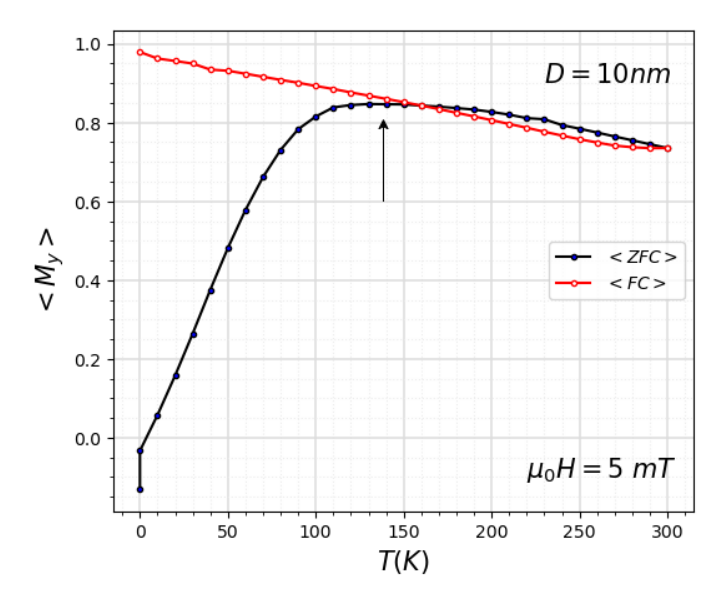


Figure 4.36: Temperature-dependent magnetization curves simulated for spherical iron oxide nanoparticles with a diameter of 10 nm.

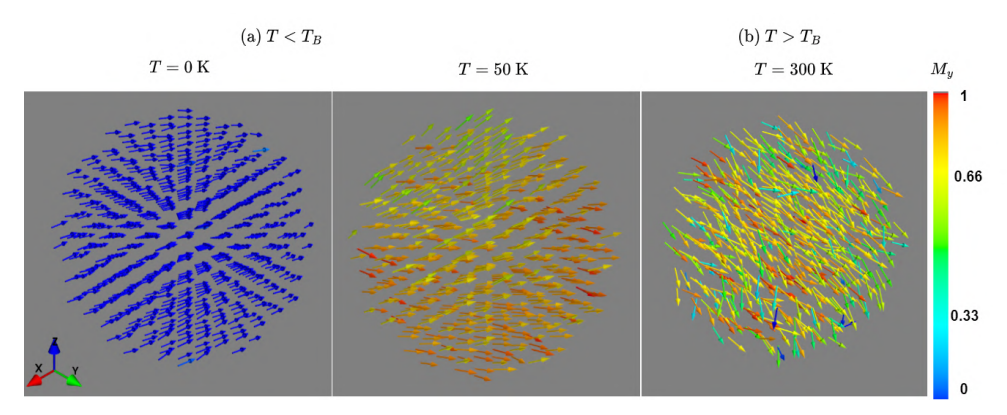


Figure 4.37: Snapshot of the magnetic moments direction for a 10 nm iron oxide nanoparticles subjected to an external magnetic field of 5 mT along the easy axis (y-axis), at selected temperatures (a) below, and (b) above the  $T_B$ .

# 4.7.2 Influence of inter-particle interactions onto the magnetic behaviour of magnetic nanoparticle systems

Dipole interactions are always present between magnetic moments. The magnitude depends on the total magnetic moment of the nanoparticles and is proportional to  $1/d_{ij}^3$ , where  $d_{ij}$  is the distance between the particles. In the case where nanoparticles are in close contact, exchange interactions can exist. The existence of magnetic interaction between nanoparticles leads to a modified magnetic behaviour, which differs from that of non-interacting nanoparticles and can lead to a collective behaviour [181]. Determining the effects of magnetic interaction is complex, because several causes can interplay. These include polydispersity, the randomness of the easy axis direction, and the presence of different types of magnetic interactions [182, 65]. In this study, we aim to systematically investigate the effects of different types of magnetic interactions onto the hysteresis curves and the magnetic blocking in a two-particle system with a fixed particle arrangement. This study is essential for understanding the magnetic properties of closely packed or clustered nanoparticles.

The model studied here consists of two identical spherical nanoparticles with two configurations: one in which the nanoparticles are in direct contact, allowing exchange coupling, and another in which they are separated by a 2 nm gap by removing two cells between the particles but retaining the same configuration so that only dipole coupling and no exchange interaction is present. Each individual nanoparticle has a diameter of 10 nm, and the simulation parameters are the same as for the iron oxide nanoparticles used above. The equilibrium magnetization results for the two configurations are shown in Fig. 4.38. In Fig. 4.38a, where the nanoparticles are in direct contact, the magnetic moments align in the same direction due to exchange coupling. This leads to a uniform magnetization state. In contrast, in Fig. 4.38b, where a 2 nm gap exists between the nanoparticles, the magnetic moments align antiparallel to each other, indicating the dominance of dipole

coupling.

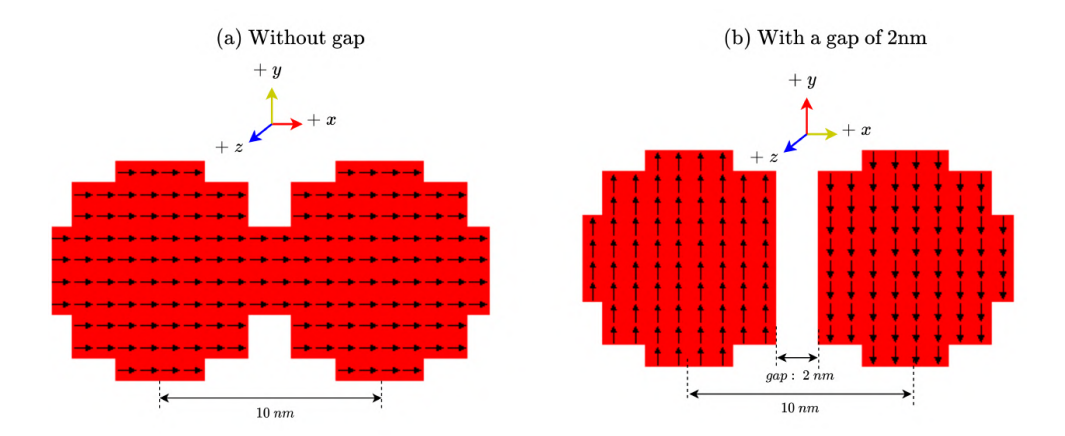


Figure 4.38: Equilibrium magnetization results of two nanospheres with a diameter of 10 nm (a) in direct contact, (b) separated with a gap of 2 nm.

For each system, the demagnetization energy,  $E_{\rm demg}$ , exchange energy,  $E_{\rm exc}$ , and uniaxial anisotropy energy,  $E_{\rm uni}$  are shown in Table 4.9. As expected, the uniform magnetization state has a lower exchange energy,  $E_{\rm exc}$ , than the antiparallel alignment. However, both configurations show a large demagnetization energy. The uniaxial anisotropy energy,  $E_{\rm uni}$ , is much greater in the uniform magnetization state, while it is minimal in the antiparallel alignment. The  $E_{\rm uni}$  is closely related to the particle volume V and the orientation of the magnetic moment. The easy axis is defined in the y-direction. When two connected particles align perpendicular to these easy axes, there is a significant increase in the anisotropy energy. Furthermore, in the particular model with a 2 nm gap between the particles, the direction of magnetization tends to align along both easy axes, resulting in a decrease in the anisotropy energy.

Table 4.9:  $E_{\text{demg}}$ ,  $E_{\text{exc}}$ , and  $E_{\text{uni}}$  per particle for a model of two spherical nanoparticles, including one configuration with direct contact and another with a 2 nm gap between the nanoparticles.

Two Spherical Particles	$E_{\text{demg}}$ kJ/m <sup>3</sup>	$E_{\rm exc}$ kJ/m <sup>3</sup>	$E_{\rm uni}$ kJ/m <sup>3</sup>
No gap	2987	2.4	840
2 nm gap	4737	4.8	0.03

#### Hysteresis curves

Fig. 4.39 shows M(H) hysteresis loops in the magnetic field range of  $\pm 100$  mT for the two spherical nanoparticles both in direct surface contact and with a 2 nm gap. In the case of direct surface contact, i.e. allowing exchange coupling, the hysteresis loop shows a rounded behaviour with the coercive field  $\mu_0H_c=25$  mT and normalized remanence  $M_r/M_s=0.5$ . In contrast, the prevalence of the dipolar coupling reveals a narrow hysteresis loop. One also found the dipolar field elongates the hysteresis loop horizontally along the external field direction, consequently reducing both remanence and coercivity. This indicates that the exchange coupling increases the remanence and coercivity, which leads to a highly uniform magnetization state.

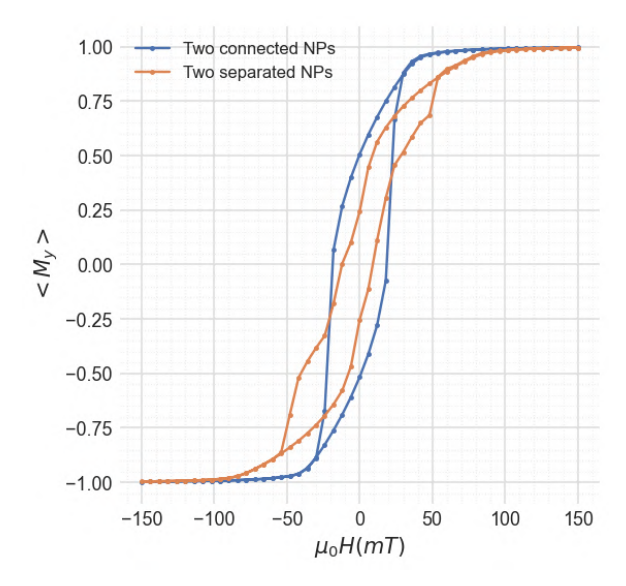


Figure 4.39: Field-dependent magnetization curves,  $\langle M(H) \rangle$  in the range of  $\pm 1.5$  mT, simulated for nanoparticles in direct contact and separated with a gap of 2 nm.

Fig. 4.40 represent M(H) hysteresis loops of two magnetic spheres separated by a gap of 2 nm, with an external magnetic field applied parallel to their anisotropy easy axes ( $\theta = 0^{\circ}$ ). One finds that there is zero remanent magnetization when the external magnetic field is removed, reflecting the antiparallel alignment of the magnetization of the two nanoparticles. In addition to zero remanence, the magnetization curves M(H) display a step-like approach to saturation and hysteresis on reversing the field sweep. An antiparallel superspin structure indicates that the energy of the magnetic dipole interaction is dominant compared with the energy of the magnetic anisotropy. A step-like feature in the loop is then induced when the energy barrier due to the magnetic anisotropy is overcome.

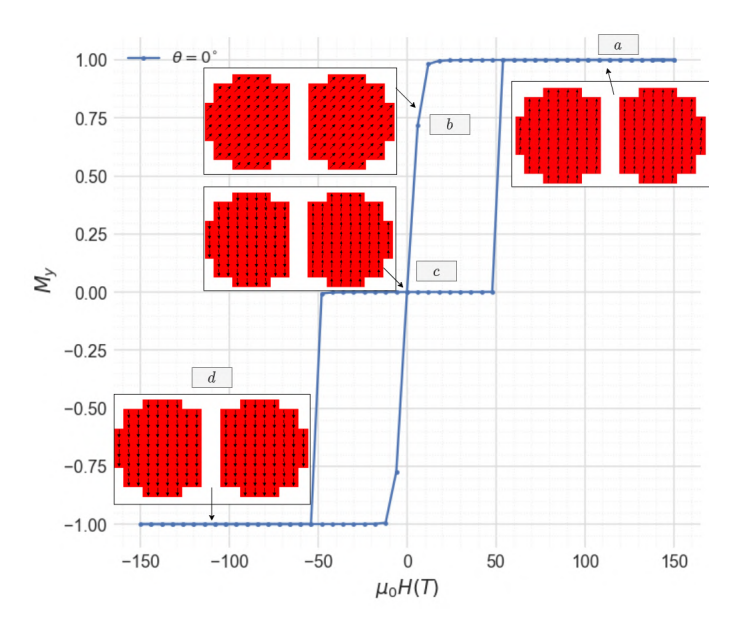


Figure 4.40: Field-dependent magnetization curves in the field range of  $\pm$  1.5 mT simulated for two spherical particles separated by a gap of 2 nm. The anisotropy axis direction is set at  $\theta=0^{\circ}$  with respect to the direction of the applied magnetic field. Points (a) to (d) indicate different states of magnetization during the hysteresis process: (a) saturation magnetization in the direction of the applied field, (b) magnetization reversal upon field reduction, (c) zero field condition, and (d) magnetic saturation in the opposite direction as the field is inverted.

#### Magnetic superspin blocking

Fig. 4.41 presents ZFC and FC magnetization curves for two connected nanoparticles over a temperature range of 0 K to 300 K, subjected to a magnetic field of 5 mT. Surprisingly, a low-temperature peak at approximately 50 K is found in addition to the expected features at 150 K. One also finds a shift of the large peak to higher temperatures when compared with the  $T_B=130$  K of the non-interacting spherical single-domain particles (Fig. 4.36). The exchange coupling leads to an enhancement of the anisotropy barrier and hence shifts the blocking temperature to a larger value.

Fig. 4.42 shows the ZFC and FC magnetization curves for the two-sphere model with a 2 nm gap simulated at 10 mT. The ZFC curve starts with a larger value and displays a low-temperature peak at 50 K in addition to  $T_B$  at approximately 100 K. One also observes a relatively rapid decrease in the magnetization above  $T_B$ , reaching a minimum at 300 K. Simulating the ZFC at 10 mT instead of 5 mT, as before, also has an effect on lowering the anisotropy barrier and thus leads to a lower blocking temperature as expected.

In summary, we investigated the impact of exchange and dipolar couplings on the hysteresis and magnetic superspin blocking of a two-nanoparticle system. The simulation

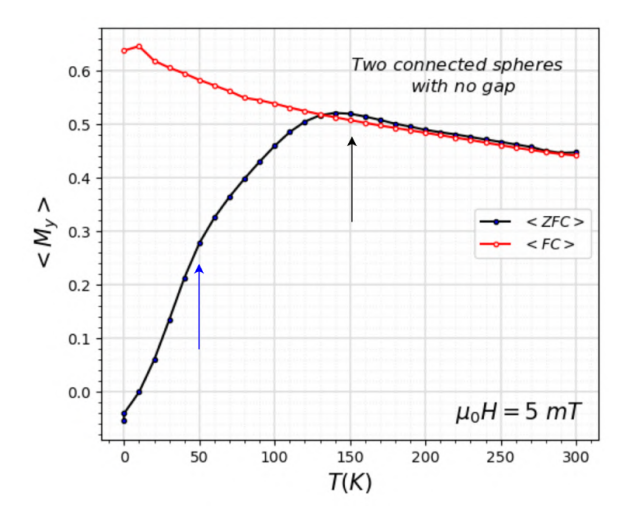


Figure 4.41: Temperature-dependent magnetization curves performed in the temperature range of 0 to 300 K for two spherical connected surface nanoparticles at a magnetic field of 5 mT. The black and blue arrows mark the blocking temperatures, and the second peak is observed below the blocking temperatures.

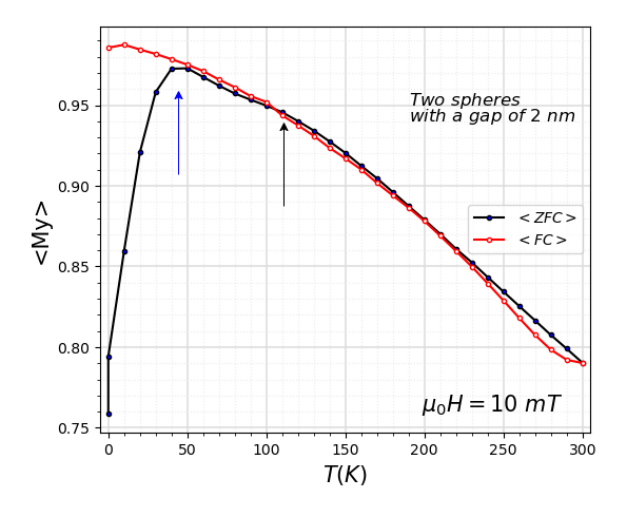


Figure 4.42: Temperature-dependent magnetization curves performed in the temperature range of 0 to 300 K for two spherical separated nanoparticles with a 2 nm gap at a magnetic field of 10 mT. The black and blue arrows mark the blocking temperatures, and the second peak is observed below the blocking temperatures.

results showed two distinct types of hysteresis loops: a rounded-shaped for exchange coupling and a step-like curve for dipolar coupling. The exchange coupling leads to both increased remanence and enhanced coercivity due to the system being uniformly magnetized. In addition, the inter-particle interactions significantly affect magnetic superspin blocking temperature. The exchange coupling shifts the blocking temperature to larger temperatures compared to non-interacting single nanoparticles, indicating an enhanced anisotropy barrier. This understanding of the impact of various magnetic interactions on altering the magnetic properties is important for optimizing and designing nanoparticle assemblies for a range of applications.

#### 4.7.3 Multi-core nanosphere-clusters

The last step was to simulate a cluster of spherical magnetic nanoparticles. The model consists of eight spherical nanoparticles, each with a diameter of 10 nm, randomly connected and randomly arranged as shown in Fig. 4.43a. This chosen arrangement closely resembles the clusters in sample C71. Next, the particle size distribution parameter was employed as shown in Fig. 4.43b. In this model, the diameter of the particles range from 6 nm to 12 nm, to investigate the influence of the size distribution on the magnetic properties, including the hysteresis loop and magnetic superspin blocking.

#### Hysteresis curves

Fig. 4.44 shows the M(H) hysteresis loop for clusters consisting of primary nanoparticles with (i) a uniform size and (ii) a size distribution. The hysteresis loop shows a rectangular shape with the coercive field  $\mu_0 H_c = 20$  mT and a normalized remanence  $M_r/M_s = 0.68$  for clusters with uniform particle size. This behaviour suggests the exciting exchange interactions between the surface particles, which lead to superparamagnetic blocked behaviour. The magnetic ground state presents magnetically ordered particles due to the existence of exchange interactions between the connected surface nanoparticles, as shown in Fig. 4.45a. A large opposite external field is then required to reverse the magnetic moments of the nanoparticles, which is characteristic of a large coercivity. In clusters with different particle diameter, the hysteresis loop has a narrow shape. The decrease in the remanence and coercivity of the system indicates an increase in dipolar interactions, while the exchange interactions decrease. The hysteresis loop shape indicates an inhomogeneous magnetization distribution. The magnetic ground state also exhibits magnetically disordered particles due to an increase in dipolar interactions over exchange interactions, as shown in Fig. 4.45b. In Fig. 4.44 one also observes that the magnetically disordered particles lead to a reduction of the magnetic saturation  $M_s$  with a relatively low remanence and coercivity compared with the clusters with magnetically ordered particles. The hysteresis loop also has a larger number of steps with small magnitude, indicating a switching behaviour of magnetically disordered particles.

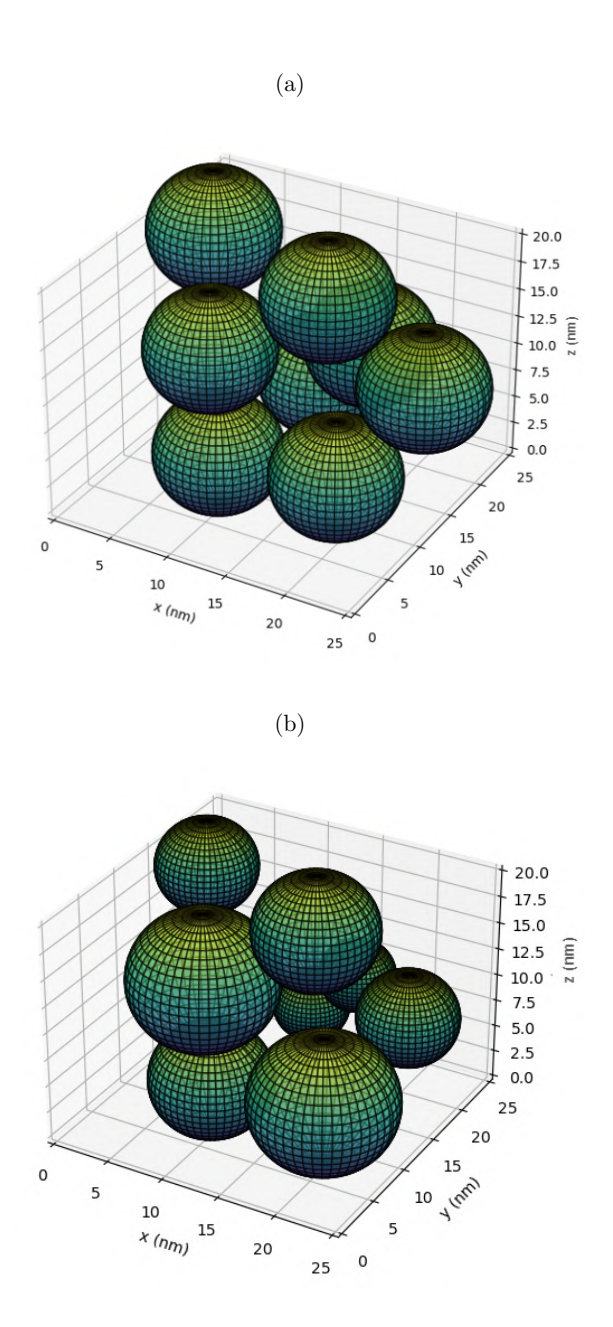


Figure 4.43: Assemblies of spherical magnetic nanoparticles (MNPs), which are randomly organized and connected with (a) a uniform size of 10 nm and (b) a size distribution from 6 to 12 nm.

#### Magnetic superspin blocking

Fig. 4.46 shows the ZFC and FC magnetization curves for a clustered system of randomly connected and arranged particles. In Fig. 4.46a, the blocking temperature is not observed in the temperature range up to 300 K. This behaviour indicates that the effective magnetic barrier energy dominates over the thermal energy  $k_{\rm B}T$ . A large peak is also observed at the low temperature of 110 K. The FC curve becomes almost flat, indicating non-negligible inter-particle interactions.

In clusters with different particle sizes, the blocking temperature shifts to a lower temperature,  $T_B = 210$  K (Fig. 4.46b). The size distribution critically influences the magnetic interactions within the system, ultimately leading to modified magnetic behaviour and a decreased blocking temperature. One also observes a shift of the low-temperature peak from 110 K to 70 K. The flat FC curve below 150 K is apparent, indicating the presence of inter-particle interactions. However, the splitting of the ZFC and FC is close to the  $T_B$ , which is not expected behaviour for polydispered particles. In this study, a directional distribution of the anisotropy easy axes is not included, and hence, it leads to an underestimation of the complexity of the system.

In conclusion, the differences in the shift of  $T_B$  indicate that the type of inter-particle interactions play a major role in determining the energy barrier and thus the overall magnetic behaviour.

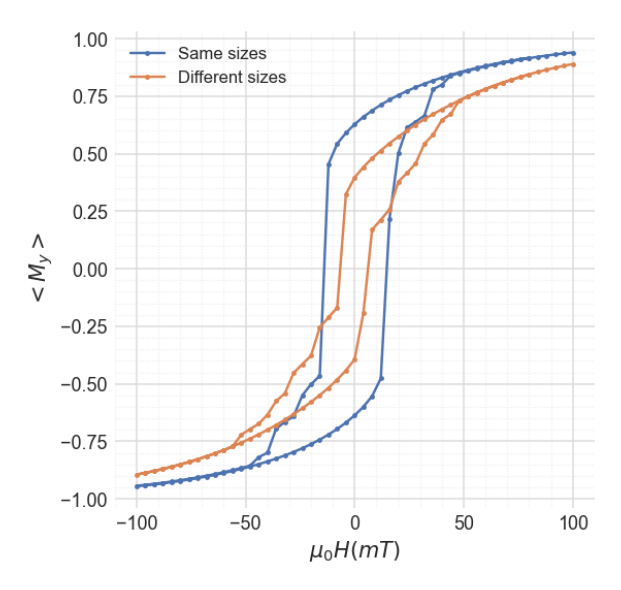


Figure 4.44: Field-dependent magnetization curves in the field range of  $\pm$  100 mT for a clustered system consisting of randomly connected and arranged particles with (i) a uniform particle size and (ii) a size distribution.

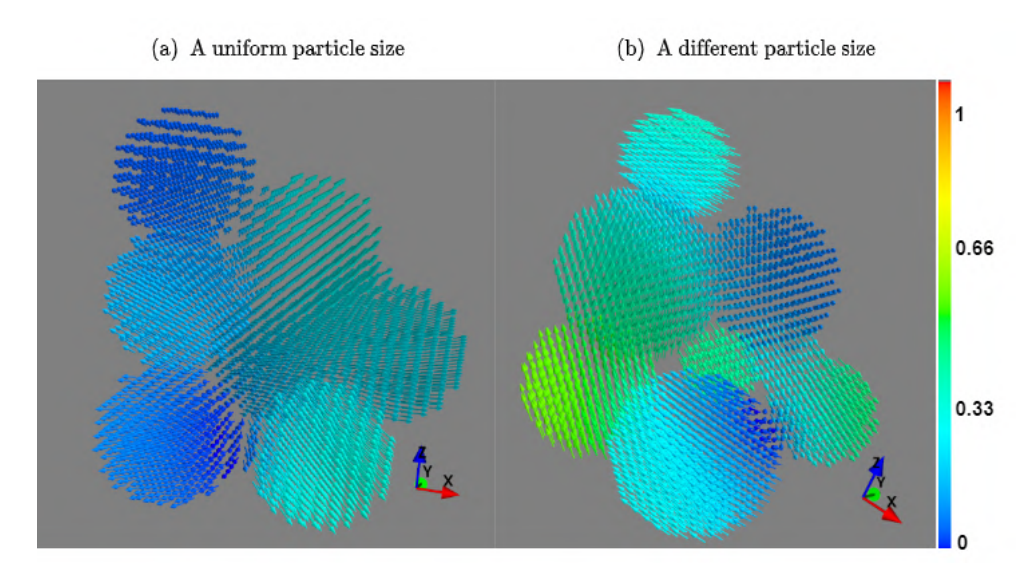


Figure 4.45: Magnetic moments of the particle distribution in a cluster with (a) a uniform particle size, (b) a different particle size.

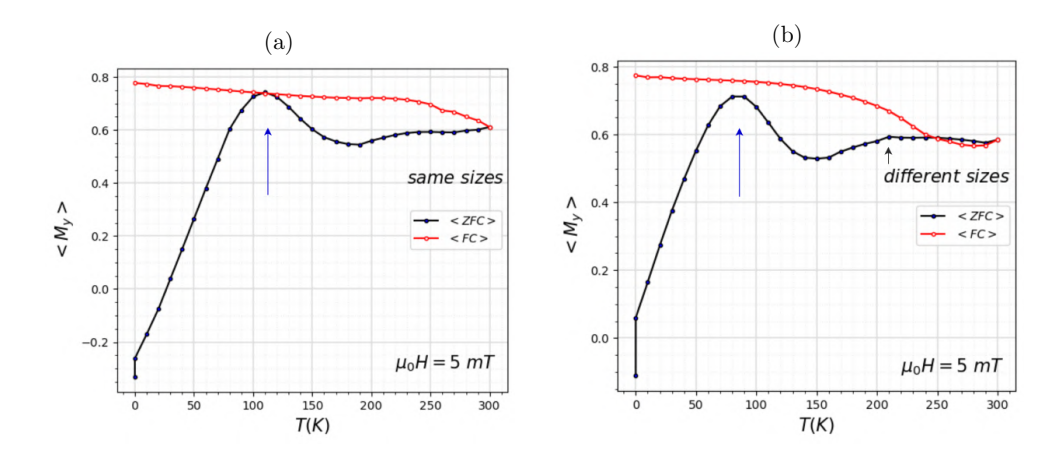


Figure 4.46: Temperature-dependent magnetization curves simulated for a cluster of randomly connected and arranged spherical nanoparticles: (a) uniform in size and (b) with a size distribution.

## Chapter 5

## Conclusions and outlook

In this work, biocompatible iron oxide nanoparticles with three types of coating materials were investigated in order to gain insight into their structural and magnetic properties. The oxidation stability and net magnetization of the iron oxide nanoparticle samples as a function of time were also studied. A range of experimental techniques such as cryogenic transmission electron microscopy (cryo-TEM), magnetometry, Mössbauer spectroscopy, and both X-ray and neutron small-angle scattering were employed to characterize the structural and magnetic proprieties of the coated nanoparticles. Additionally, micromagnetic simulations using the OOMMF software were applied to ensembles of randomly arranged and connected nanoparticles with the aim to model magnetization hysteresis loops, as well as the temperature dependence of magnetization through the zero-field cooling (ZFC) and field cooling (FC) protocols. This provided insights in the superspin structure of the interacting particles inside the cluster arrangements. Overall, the results of the study are as follows:

First, the results of the structural characterization of the different biocompatible nanoparticles indicate that the type of coating significantly influences the organization of the nanoparticles into distinct structures. The SAXS results show that the different coating types lead to different cluster sizes in the solutions: 36 nm for dextran (sample named D40), 56 nm for citrate (sample named C71), and fractal cluster aggregates for APTES (sample named B47). The underlying particle core sizes as obtained from cryo-TEM are 2 nm for sample D40, 9.5 nm for sample C71, and 9.8 nm for sample B47. However, the crystalline sizes determined by XRD are larger than the core sizes found with TEM, which can be attributed to the sizes in TEM being underestimated due to the presence of aggregated particles and a large degree of polydispersity. This makes it difficult to estimate the sizes of single nanoparticles. Overall, the structural properties obtained are directly connected to the magnetic behaviour of the nanoparticles. Therefore, the structural characterization of nanoparticles is essential for optimizing the particle synthesis strategies to achieve the desired magnetic properties for medical applications.

Second, the aging results obtained by Mössbauer spectroscopy show a clear trend of oxidation from magnetite to maghemite over time, particularly for samples C71 and B47, which displayed a rapid decrease in magnetite fraction after less than 0.1 days in air (the

time between the end of the synthesis and the sealing of the sample under  $N_2$  atmosphere). Notably, approximately 40% of the magnetite volume had oxidized within a few hours after exposure to ambient air, highlighting the necessity for rapid sealing under inert atmosphere to preserve the magnetic properties. Sample D40 exhibited an even faster oxidation rate, likely due to its smaller particle size, leading to negligible detection of  $Fe^{2+}$  already in the initial spectra. In contrast, C71 and B47 demonstrated a slower oxidation, with a magnetite fraction of only 10-20% remaining after one month and negligible magnetite fraction detected after three months, as observed by both Mössbauer spectroscopy and magnetometry. In comparison, samples stored under inert conditions maintained a larger magnetite content, preserving a fraction of 20-30% after 6 months, which was comparable to the fraction observed after 10-30 days under ambient air conditions. The detailed understanding of the aging processes of the particles is of great importance for officially approved quality standards. Such knowledge can guide the development of more stable nanoparticles that retain their magnetic properties for extended periods.

Third, magnetic SANS measurements on the C71 sample dispersed in H<sub>2</sub>O and D<sub>2</sub>O provide the magnetic size of the cluster nanoparticles both at zero magnetic field and with an external magnetic field. The zero-field magnetic size obtained from the contrast variation method is slightly larger than that of the individual nanoparticles measured by TEM, consistent with the expected magnetic correlations within the clusters at zero field. The magnetic size is also consistent with the ZFC curves at a small field of 5 mT. Upon reaching saturating magnetic field (1.1 T), the 2D SANS patterns exhibit a predictable anisotropy originating from an anisotropic magnetic scattering distribution. A Guinier fit to the magnetic scattering at 1.1 T reveals a coherent magnetic size of the clusters that is approximately half of the total cluster size, corroborating the presence of magnetic domains inside the clusters. The latter result is important in terms of obtaining nanoparticle assemblies with large magnetic susceptibility, where coherent rotation of the superspins within the cluster is desired. These results have a direct impact on factors such as the  $T_2$  relaxation time in MRI and the specific absorption rate (SAR) for hyperthermia applications. The results of this study provide valuable insights into the design and synthesis of nanoparticles for these medical applications.

Fourth, OOMMF simulations were performed on both a two-particle model and ensembles of randomly arranged and connected nanoparticles using the structural parameters such as the morphology (shape and size), and aggregation state, obtained from the C71 sample. This study is important to gain a deeper understanding of the magnetic interactions among the particle cores and their collective behavior. The "theta evolver" function within OOMMF was used to simulate also thermal fluctuations of the magnetic moments of the nanoparticles. This approach allowed to model the zero-field-cooled (ZFC) and field-cooled (FC) curves.

In the two-particle model, two conditions were simulated: one with dominant dipolar coupling and no exchange interactions, and another with the existence of exchange coupling. The results indicate that these interactions have distinct effects on the shape of the magnetization hysteresis loop and the magnetic superspin blocking. In the case of dominant dipolar interactions without exchange coupling, the hysteresis loop is characterized by a

narrow shape, resulting in a smaller coercivity and remanence. In contrast, the inclusion of exchange interactions leads to a rounded hysteresis loop, with a notable enhancement in both coercivity and remanence. Moreover, the exchange interactions shift the blocking temperature to a larger value compared to that of non-interacting single-domain nanoparticles.

In the model of clustered particles with random connections and arrangements, two conditions were simulated: one with a uniform particle size and another with a distribution of different particle sizes. The results show that uniform particle sizes favor the presence of exchange interactions between the surfaces of the nanoparticles, resulting in a rectangular hysteresis loop characterized by large remanence and coercivity. In contrast, the introduction of a size distribution led to altered inter-particle interactions, resulting in the system exhibiting a smaller remanence and coercivity. Furthermore, the presence of exchange interactions leads to a shift of the blocking temperature to a larger value compared to a system in which both dipolar and exchange interactions are present. Overall, the obtained result helps to obtain a detailed understanding of the role of inter-particle interactions on the magnetic behaviour.

The findings from this research on clustered nanoparticles pave the way for further exploration and understanding of the magnetic behaviour in such systems. A key outcome of this study is the successful determination of the magnetic size of nanoparticles in the liquid state using neutron scattering techniques. To enhance our understanding of the dynamics of aggregated nanoparticles, it is essential to also perform measurements in the immobilized state as this would help to investigate the development of magnetic core size with fields independent of the ensemble behaviour. Combining these results with ZFC and FC measurements for clustered particles in both liquid and immobilized states would provide valuable insights into the mechanisms of magnetic relaxation.

One of the experiments conducted involved time-resolved in situ XANES and anomalous SAXS/WAXS measurements while annealing a single core iron oxide in air at 170°C. The goal was to determine the composition of the iron oxide core and track its changes during annealing. However, we faced difficulties in analyzing the data due to a structure factor that appeared due to the fact that the studied sample was in a powder state. To address this, it would be beneficial to repeat the experiment and find ways to stabilize the particles in different liquids i.e. ionic liquids which have a high boiling point.

In future research, we plan to extend our previous work by investigating the influence of geometrical configurations on magnetic properties. We will use micromagnetic simulations to investigate three arrangements: simple cubic, face-centered cubic (FCC), close-packed, and random packing. We will begin by modifying our models so that the anisotropy for each nanoparticle in the cluster is randomly distributed. This will help us understand how the randomness of these easy axes affects the magnetization behaviour and be closer to the experimental conditions. By exploring these different configurations and easy axis distributions, we aim to gain insights into the complex interactions among nanoparticles and their geometrical influences on magnetic properties. This research will improve our theoretical understanding of the effects of interactions between nanoparticles and provide valuable applications in the field of nanomagnetism.

### Acknowledgments

I would like to take a moment to express my gratitude to everyone who supported me during the thesis period. This work would not have been achievable without the contributions, guidance, and unwavering belief of those around me.

First of all, I would like to thank **Dr. Artem Feoktystov & PD Dr. Oleg Petracic** for being my PhD supervisors. It has been an honor to work with both of you. I truly appreciate your efforts in introducing me to the fascinating world of scattering and nanomagnetism, and I am thankful for your patience and the extensive knowledge you have shared with me. Your support and helpful feedback on my writing made a significant difference in my PhD. I truly enjoyed our discussions and the ideas that helped shape my thesis. Many thanks again for **PD Dr. Oleg Petracic** for introducing me to the OOMMF simulation program and for the discussions. I am very grateful for everything you have done for me.

I would like to thank **Prof. Dr. Thomas Brückel** for accepting me to be a PhD student in JCNS-2 at the Forschungszentrum Jülich.

I would like to thank **Dr. Stefan Mattauch** for giving me the opportunity to work in JCNS-4 at MLZ, Garching.

I would like to thank **PD Dr. Joachim Wuttke** for being the scientific supervisor, and **PD Dr. Sebastian Mühlbauer** for agreeing to be my second referee.

I appreciate the collaboration with **Dr. Harald Unterweger & Dr. Rainer Tietze** who provided the iron oxide nanoparticle samples, supported my participation in the preparation, and contributed to discussions about the motivation of the project.

I appreciate the collaboration with **Dr. Joachim Landers** for providing help in performing Mössbauer experiments and for support in writing.

I would like to thank **Dr. Xiao Sun** for help and support during in situ Anomalous SAXS experiments. I would also like to thank **Dr. Baohu Wu** for his help with the SAXS measurements in Garching and the data reduction.

Acknowledgments 117

I would like to thank **Prof. Elliot Gilbert** for his help and support during the SANS experiments, in addition to **Dr. Asma Qdemat & Dr. Anastasiia Murmiliuk**, for their assistance in joining and helping with the measurements, along with their support in writing the paper published in PCCP.

**Dr. Marie-Sousai Appavou** helped with the transmission electron microscopy experiments at JCNS. He is deeply missed after his passing, and his spirit will always be remembered.

Many thanks to my nanoparticle group, including **Dr. Emmanuel Kentzinger**, **Dr. Nileena Nandakumaran**, **Dr. Asma Qdemat**, **Dr. Tobias Köhler** for the great time spent together during our JCNS-2 nanoparticle group meetings.

I thank JCNS-4 secretaries **Franziska Michel** & **Monika Krug** for all support regarding non-disciplinary matters such as business trips.

I want to express my thanks to **Joao Paulo Fragione Innocente** for help with technical and IT problems.

I thank **Dr. Ahmed Bassalat** from Al-Najah University for his attention and support especially at the beginning of my PhD study.

I would like to acknowledge financial support by the German Federal Ministry of Education and Research in the frame work of the Palestinian-German Science Bridge (PGSB) .

Many thanks for my friend **Sabreen** for all the emotional support and the wonderful memories that will stay with me forever.

Last but not least, my special thanks go to my husband Ibraheem, my son Loai, my parents, and my siblings for their unlimited support in every step of my life.

1.1	aggregates	3
2.1	Magnetic moments from (a) current and (b) orbital angular momentum and the spin of an electron.	8
2.2	Schematic of a magnetic dipole moment $\vec{\mu}_1$ with the corresponding dipolar field, and a second moment $\vec{\mu}_2$ located at distance $r$	10
2.3	$\mathrm{Fe^{3+}\text{-}O^{2-}\text{-}Fe^{3+}}$ configurations at (a) 180°, (b) 90°	13
2.4	Schematic representation of (a) super-exchange and (b) double-exchange	
	interactions in $Fe_3O_4$	13
2.5	Magnetic spin ordering and magnetic susceptibility curves for various mag-	
	netic materials	18
2.6	Sketch of the stray field of elongated particles resulting from the distribution	
	of magnetic poles on its surface	20
2.7	(a) An ellipsoidal Stoner-Wolfarth particle with a uniaxial anisotropy. (b)	
	Energy change of the system as a function of parameter $h$ ( $h = \frac{H_{\text{ext}}}{H_K}$ with	
	$H_K$ being the anisotropy field	22
2.8	Sketch of the scattering process with the incoming plane wave is scattered	00
0.0	by a single fixed scatterer located at position $\vec{R}$	26
2.9	hierarchical structures of agglomeration of cluster particles	34
2.10	Physical meaning of the autocorrelation function for two identical spherical	26
0.11	particles with radius $R$	36
2.11	[72]	37
9 19	Decay scheme of <sup>57</sup> Co nucleus into excited state of the <sup>57</sup> Fe nucleus	42
	Hyperfine interactions within the absorber material and the resulting Möss-	42
2.10	bauer spectrum	43
2 14	Sketch of the precession of the magnetization vector, $\vec{M}$ , precessing around	10
2.11	the effective field, $\vec{H}_{\text{eff}}$ , with damping effects, which are described by the	
	Landau-Lifshitz-Gilbert equation	45
3.1	Schematics of the instrument GALAXI	50
3.2	Schemeatics of the optics of the P62 beamline	50
3.3	•	51

3.4	Mounting of the powder sample in the ceramic heater	52
3.5	Scheme of the QUOKKA instrument layout	52
3.6	The SQUID design and principle	55
3.7	ZFC/FC magnetization measurements of water samples performed without	- 0
0.0	rapid cooling.	56
3.8	A diagram representation of the objective lens function in transmission electron microscopy	57
3.9	Sample preparation steps in a plunge freezer device.	59
5.3	painple preparation steps in a plunge neezer device.	99
4.1	Crystalline and magnetic structure of (a) magnetite, (b) hematite, and (c)	
	wüstite.	65
4.2	Molecular structure of the three types of coatings (a) Citrate, (b) APTES,	0.
4.9	and (c) Dextran	67
4.3	Cryo-TEM images for the (a) C71, (b) B47, (c) and D40 samples	70 71
4.4 4.5	XRD pattern for samples C71 (red), B47 (blue), and D40 (green) SAXS curves in dilution series for samples (a) C71, (b) D40, and (c) B47,	11
4.0	(d) d) represents pair-distance distribution functions, $P(r)$ , for C71 and D40.	73
4.6	A Cryo-TEM image for SC sample	74
4.7	Dilution series SAXS curves for the SC sample.	74
4.8	(a) SAXS curves and (b) pair-distance distribution functions $P(r)$ for the	
	samples C64, CU5, and C71	75
4.9	Cryo-TEM images for (a) C64 and (b) CU5 samples	76
4.10	Hysteresis loops for the C71, D40, and B47 samples at (a) 300 K and (b) 5 K.	77
4.11	Normalized ZFC/FC curves performed in the temperature range of $5-225$	
	K and a magnetic field of 5 mT for samples C71, B47, and D40	78
	ZFC (black) and FC (red) curves for SC sample	79
4.13	ZFC/FC curves measured at different magnetic fields 5 mT, 10 mT, and	
	100 mT for samples (a) C71 and (b) B47, and (C) D40	80
	(a) ZFC/FC curves and (b) $M(H)$ curves at 300 K for C64 and Cu5 samples.	81
	SANS intensity curves of C71 for various $H_2O/D_2O$ mixtures	82
4.16	(a) SAXS curves, and (b) normalized ZFC/FC curves of the fresh sample	02
4 17	and after 6 months from preparation for the C71 sample	83
4.17	or the scattering intensity as a function of the $B_2O$ content at a $Q$ value of $0.06 \text{ Å}^{-1}$ . (b) The determined contrast match points as a function of $Q$ .	84
4 18	Pure magnetic scattering in the D <sub>2</sub> O sample (at zero magnetic field) and	04
1.10	(b) it is Guinier fit	85
4.19	Two-dimensional unpolarized SANS patterns for 100% D <sub>2</sub> O at various	
	vertical magnetic fields (0 to 1.1 T)	86
4.20	(a) Scattering intensity sectors and (b) pure magnetic scattering of D <sub>2</sub> O	
	sample	87
4.21	Two-dimensional unpolarized SANS patterns for 100% $\mathrm{H}_{2}\mathrm{O}$ at various	
	vertical magnetic fields (0 to 1.1 T)	88

4.22	(a) Scattering intensity sectors and (b) pure magnetic scattering of $H_2O$ sample
4.23	Mössbauer spectra for sample (a) C71, (b) B47, and (c) D40 after various aging times of exposure to air, recorded at 5 K and an applied magnetic field of 8 T
4.24	Mössbauer spectra for SC sample recorded at 5 K and an applied magnetic field of 8 T
4.25	Magnetite fraction dependence on time as obtained from Mössbauer spectroscopy and magnetometry
4.26	ASAXS curves were measured at six different energies around Fe $K$ edge of 7112 eV for the SC sample
4.27	In situ SAXS curves measured (a) during heating up, and (b) during annealing in vacuum for 4.5 h at 120°C
4.28	In situ SAXS curves measured (a) during heating up, and (b) during annealing in vacuum for 4.5 h at 170°C
4.29	XANES data (Fe $K$ -edge) during heating and annealing in vacuum at 170°C. 9
4.30	In situ SAXS curves measured at (a) $80^{\circ}$ C and (b) $120^{\circ}$ C 9
4.31	XANES data (Fe K-edge) during annealing in air at 120° 99
4.32	3D representation of magnetization distribution in Fe3O4 nanoparticles
	(diameters 55 nm to 100 nm)
4.33	Energy competition between the demagnetization field and exchange interaction for spherical Fe3O4 nanoparticles as a function of particle diameter. 10
4.34	Field-dependent magnetization curves at various angles of the easy axis relative to the applied magnetic field $(y$ -axis)
4.35	Average field-dependent magnetization curve, $\langle M(H) \rangle$ simulated for a spherical iron oxide nanoparticles with a diameter of 10 nm 10
4.36	emperature-dependent magnetization curves for simulated spherical iron oxide nanoparticles with a diameter of 10 nm
4.37	Snapshot of the magnetic moments' direction for 10 nm iron oxide nanoparticles under a 5 mT external magnetic field along the easy axis $(y$ -axis) at
	selected temperatures: (a) below and (b) above $T_B$
4.38	Equilibrium magnetization results for two nanospheres with a diameter of 10 nm: (a) in direct contact and (b) separated by a 2 nm gap 1000
4.39	Field-dependent magnetization curves, $\langle M(H) \rangle$ , in the range of $\pm 1.5$ mT, simulated for nanoparticles in direct contact and those separated by a 2 nm
	gap
4.40	Field-dependent magnetization curves simulated for two spherical particles separated by a gap of 2 nm. $\dots \dots \dots$
4.41	Temperature-dependent magnetization curves performed in the temperature range of 0 to 300 K for two spherical connected surface nanoparticles at a
	magnetic field of 5 mT

4.42	Temperature-dependent magnetization curves performed in the temperature
	range of 0 to 300 K for two spherical separated nanoparticles with a 2 nm $$
	gap at a magnetic field of 10 mT
4.43	Assemblies of spherical magnetic nanoparticles (MNPs), which are randomly
	organized and connected with $(a)$ a uniform size of 10 nm and $(b)$ a size
	distribution from 6 to 12 nm
4.44	Field-dependent magnetization curves in the field range of $\pm$ 100 mT for a
	clustered system consisting of randomly connected and arranged particles
	with (i) a uniform particle size and (ii) a size distribution
4.45	Magnetic moments of the particle distribution in a cluster with (a) a uniform
	particle size, (b) a different particle size
4.46	Temperature-dependent magnetization curves simulated for a cluster of
	randomly connected and arranged spherical nanoparticles: (a) uniform in
	size and (b) with a size distribution
A1	M(T) curves taken in the 5 - 225 K temperature range and a magnetic field
	of 5 mT, 10 mT, and 1000 mT for samples (a) C64, and (b) CU5 125
A2	Representative spectra of the Mössbauer relaxation study of samples C71,
	B47 (APTES), and D40 measured between 5 K and 250 K 126

# List of Tables

4.1	The hydrodynamic diameter, polydispersity index (PDI), and Zeta potential	
	(mV) for the C71, B47, and D40 samples. Physicochemical characterization	
	techniques were performed at the laboratory of the University Hospital	
	Erlangen.	67
4.2	The hydrodynamic diameter, polydispersity index (PDI), and Zeta potential	
	(mV) of the citrate-coated particles C64 and CU5	68
4.3	List of the samples used in this thesis, indicating their storage conditions	
	(air or nitrogen, $N_2$ ) and the analytical techniques applied	68
4.4	Diameter of single particles $D_{\text{core}}$ and $\sigma$ of the log-normal size distribution	
	of single cores determined by TEM, along with crystalline size $(D_{\rm XRD})$ for	
		71
4.5	$\rho$ and $\rho_{mag}$ in the unit of $10^{-6} \text{ Å}^{-2}$ for the investigated components and	
	solvents and their contrast $\Delta \rho^2$ in unit of $10^{-12} \text{ Å}^{-4}$	82
4.6	Magnetite fraction as a function of oxidation time determined from Möss-	
	bauer spectroscopy analysis	90
4.7	Magnetite fraction and saturation magnetization as a function of oxidation	
	time obtained from magnetometry.	93
4.8	$M_s$ , $A$ , and $K$ simulation parameters for Fe <sub>3</sub> O <sub>4</sub> materials with single-domain	
	(SD), multi-domain (MD), and transition to MD state at critical diameter $D_c$ .	99
4.9	$E_{\text{demg}}$ , $E_{\text{exc}}$ , and $E_{\text{uni}}$ per particle for a model of two spherical nanoparticles,	
	including one configuration with direct contact and another with a 2 nm	
	gap between the nanoparticles	05

## Appendix

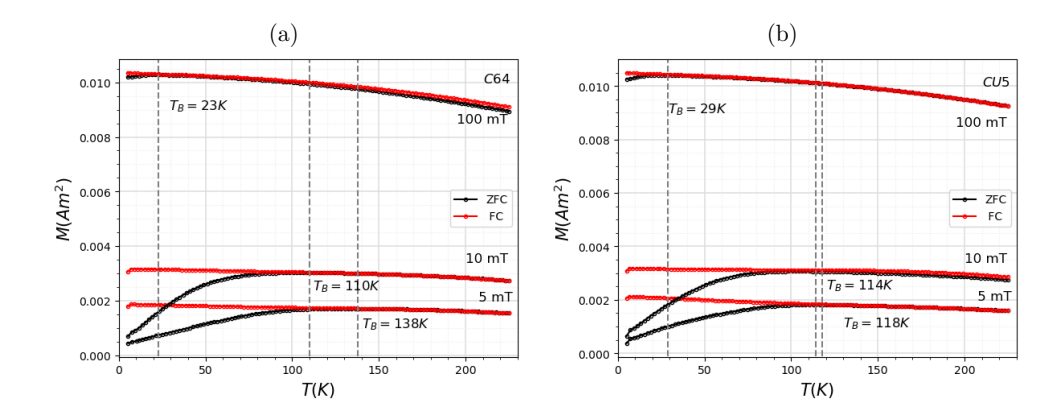


Figure A1: M(T) curves taken in the 5 - 225 K temperature range and a magnetic field of 5 mT, 10 mT, and 1000 mT for samples (a) C64, and (b) CU5.

Appendix 126

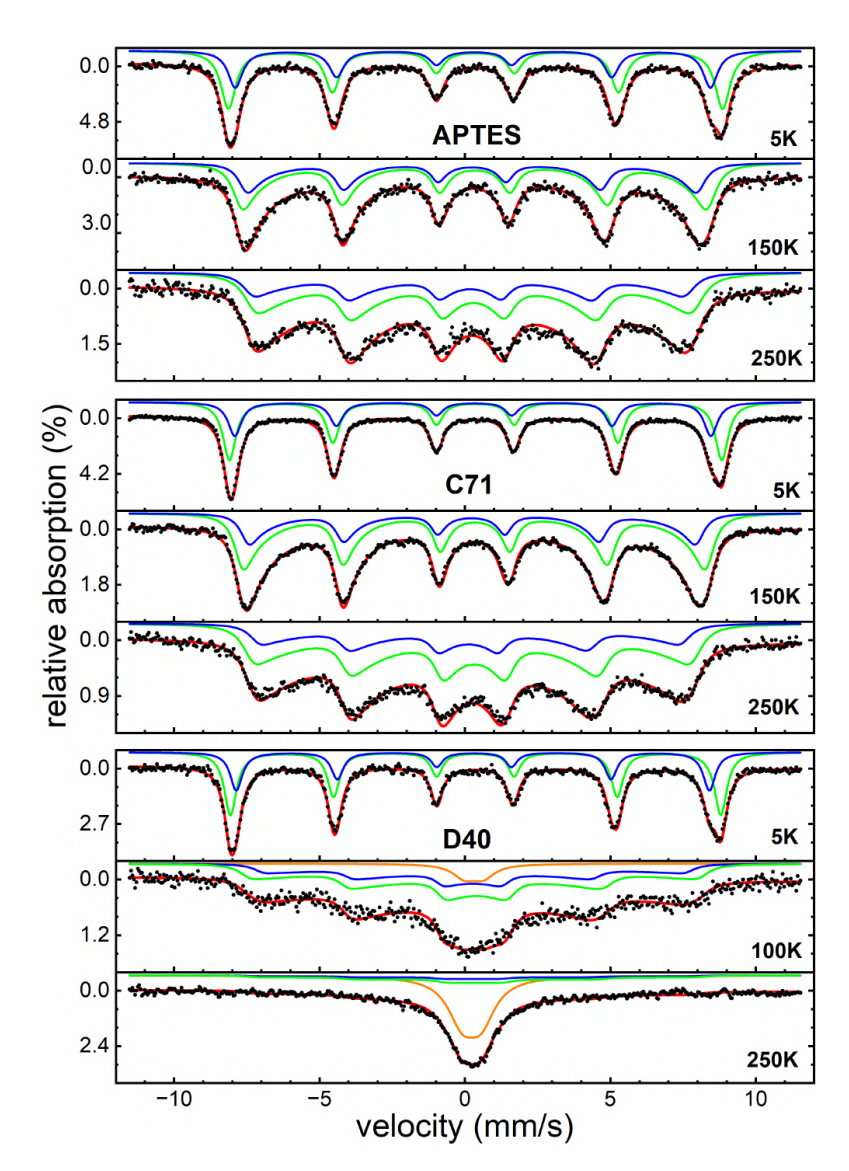


Figure A2: Representative spectra of the Mössbauer relaxation study of samples C71, B47 (APTES), and D40 measured between 5 K and 250 K. For the C71 and B47 samples, three subspectra are displayed up to 250 K. However, for the D40 sample, the three subspectra are unresolved, showing only the presence of one broadened sextet (orange sextet) at 250 K.

## Bibliography

- [1] Nasser A, Qdemat A, Unterweger H, Tietze R, Sun X, Landers J, et al. Impact of coating type on structure and magnetic properties of biocompatible iron oxide nanoparticles: insights into cluster organization and oxidation stability. Physical Chemistry Chemical Physics. 2024;26(38):24912-23.
- [2] Davis ME, Chen Z, Shin DM. Nanoparticle therapeutics: an emerging treatment modality for cancer. Nature Reviews Drug Discovery. 2008;7(9):771-82.
- [3] Cortajarena AL, Ortega D, Ocampo SM, Gonzalez-García A, Couleaud P, Miranda R, et al. Engineering iron oxide nanoparticles for clinical settings. Nanobiomedicine. 2014;1:2.
- [4] Nedyalkova M, Donkova B, Romanova J, Tzvetkov G, Madurga S, Simeonov V. Iron oxide nanoparticles—in vivo/in vitro biomedical applications and in silico studies. Advances in Colloid and Interface Science. 2017;249:192-212.
- [5] Yang L, Kuang H, Zhang W, Aguilar ZP, Xiong Y, Lai W, et al. Size dependent biodistribution and toxicokinetics of iron oxide magnetic nanoparticles in mice. Nanoscale. 2015;7(2):625-36.
- [6] Anselmo AC, Mitragotri S. Nanoparticles in the clinic. Bioengineering & Translational Medicine. 2016;1(1):10-29.
- [7] Ferguson RM, Khandhar AP, Kemp SJ, Arami H, Saritas EU, Croft LR, et al. Magnetic particle imaging with tailored iron oxide nanoparticle tracers. IEEE Transactions on Medical Imaging. 2014;34(5):1077-84.
- [8] Iv M, Telischak N, Feng D, Holdsworth SJ, Yeom KW, Daldrup-Link HE. Clinical applications of iron oxide nanoparticles for magnetic resonance imaging of brain tumors. Nanomedicine. 2015;10(6):993-1018.
- [9] Arruebo M, Fernández-Pacheco R, Ibarra MR, Santamaría J. Magnetic nanoparticles for drug delivery. Nano Today. 2007;2(3):22-32.
- [10] El-Boubbou K. Magnetic iron oxide nanoparticles as drug carriers: Preparation, conjugation and delivery. Nanomedicine. 2018;13(8):929-52.

Bibliography 128

[11] Piñeiro Y, Vargas Z, Rivas J, López-Quintela MA. Iron oxide based nanoparticles for magnetic hyperthermia strategies in biological applications. European Journal of Inorganic Chemistry. 2015;2015(27):4495-509.

- [12] Ito A, Yamaguchi M, Okamoto N, Sanematsu Y, Kawabe Y, Wakamatsu K, et al. T-cell receptor repertoires of tumor-infiltrating lymphocytes after hyperthermia using functionalized magnetite nanoparticles. Nanomedicine. 2013;8(6):891-902.
- [13] Pablico-Lansigan MH, Situ SF, Samia ACS. Magnetic particle imaging: advancements and perspectives for real-time in vivo monitoring and image-guided therapy. Nanoscale. 2013;5(10):4040-55.
- [14] Skotland T, Iversen TG, Sandvig K. Development of nanoparticles for clinical use. Taylor & Francis; 2014.
- [15] El-Boubbou K. Magnetic iron oxide nanoparticles as drug carriers: clinical relevance. Nanomedicine. 2018;13(8):953-71.
- [16] Wahajuddin n, Arora S. Superparamagnetic iron oxide nanoparticles: magnetic nanoplatforms as drug carriers. International Journal of Nanomedicine. 2012:3445-71.
- [17] Dhar D, Ghosh S, Das S, Chatterjee J. A review of recent advances in magnetic nanoparticle-based theranostics of glioblastoma. Nanomedicine. 2022;17(2):107-32.
- [18] Bedanta S, Petracic O, Kleemann W. Supermagnetism. vol. 23. Elsevier; 2015.
- [19] Petracic O. Superparamagnetic nanoparticle ensembles. Superlattices and Microstructures. 2010;47(5):569-78.
- [20] Zhu L, Zhou Z, Mao H, Yang L. Magnetic nanoparticles for precision oncology: theranostic magnetic iron oxide nanoparticles for image-guided and targeted cancer therapy. Nanomedicine. 2017;12(1):73-87.
- [21] McCarthy JR, Weissleder R. Multifunctional magnetic nanoparticles for targeted imaging and therapy. Advanced Drug Delivery Reviews. 2008;60(11):1241-51.
- [22] Lin MM, Kim HH, Kim H, Dobson J, Kim DK. Surface activation and targeting strategies of superparamagnetic iron oxide nanoparticles in cancer-oriented diagnosis and therapy. Nanomedicine. 2010;5(1):109-33.
- [23] Blanco-Andujar C, Walter A, Cotin G, Bordeianu C, Mertz D, Felder-Flesch D, et al. Design of iron oxide-based nanoparticles for MRI and magnetic hyperthermia. Nanomedicine. 2016;11(14):1889-910.
- [24] Patsula V, Moskvin M, Dutz S, Horák D. Size-dependent magnetic properties of iron oxide nanoparticles. Journal of Physics and Chemistry of Solids. 2016;88:24-30.

Bibliography 129

[25] Roca AG, Gutiérrez L, Gavilán H, Brollo MEF, Veintemillas-Verdaguer S, del Puerto Morales M. Design strategies for shape-controlled magnetic iron oxide nanoparticles. Advanced Drug Delivery Reviews. 2019;138:68-104.

- [26] Albanese A, Tang PS, Chan WC. The effect of nanoparticle size, shape, and surface chemistry on biological systems. Annual Review of Biomedical Engineering. 2012;14(1):1-16.
- [27] Benitez M, Mishra D, Szary P, Confalonieri GB, Feyen M, Lu A, et al. Structural and magnetic characterization of self-assembled iron oxide nanoparticle arrays. Journal of Physics: Condensed Matter. 2011;23(12):126003.
- [28] Blanco-Andujar C, Ortega D, Southern P, Pankhurst Q, Thanh N. High performance multi-core iron oxide nanoparticles for magnetic hyperthermia: microwave synthesis, and the role of core-to-core interactions. Nanoscale. 2015;7(5):1768-75.
- [29] Hobson NJ, Weng X, Siow B, Veiga C, Ashford M, Thanh NT, et al. Clustering superparamagnetic iron oxide nanoparticles produces organ-targeted high-contrast magnetic resonance images. Nanomedicine. 2019;14(9):1135-52.
- [30] Shrestha S, Wang B, Dutta P. Nanoparticle processing: Understanding and controlling aggregation. Advances in Colloid and Interface Science. 2020;279:102162.
- [31] Gallo-Cordova A, Ovejero JG, Pablo-Sainz-Ezquerra AM, Cuya J, Jeyadevan B, Veintemillas-Verdaguer S, et al. Unravelling an amine-regulated crystallization crossover to prove single/multicore effects on the biomedical and environmental catalytic activity of magnetic iron oxide colloids. Journal of Colloid and Interface Science. 2022;608:1585-97.
- [32] Moya C, Escoda-Torroella M, Rodríguez-Álvarez J, Figueroa AI, García Í, Ferrer-Vidal IB, et al. Unveiling the crystal and magnetic texture of iron oxide nanoflowers. Nanoscale. 2024;16(4):1942-51.
- [33] Friedrich RP, Janko C, Unterweger H, Lyer S, Alexiou C. SPIONs and magnetic hybrid materials: Synthesis, toxicology and biomedical applications. Physical Sciences Reviews. 2023;8(8):1435-64.
- [34] Shokrollahi H. A review of the magnetic properties, synthesis methods and applications of maghemite. Journal of Magnetism and Magnetic Materials. 2017;426:74-81.
- [35] Lavorato GC, de Almeida AA, Vericat C, Fonticelli MH. Redox phase transformations in magnetite nanoparticles: impact on their composition, structure and biomedical applications. Nanotechnology. 2023;34(19):192001.
- [36] Jiang K, Zhang Q, Hinojosa DT, Zhang L, Xiao Z, Yin Y, et al. Controlled oxidation and surface modification increase heating capacity of magnetic iron oxide nanoparticles. Applied Physics Reviews. 2021;8(3).

[37] Dennis C, Jackson A, Borchers J, Hoopes P, Strawbridge R, Foreman A, et al. Nearly complete regression of tumors via collective behavior of magnetic nanoparticles in hyperthermia. Nanotechnology. 2009;20(39):395103.

- [38] Li L, Mak K, Leung CW, Chan K, Chan W, Zhong W, et al. Effect of synthesis conditions on the properties of citric-acid coated iron oxide nanoparticles. Microelectronic Engineering. 2013;110:329-34.
- [39] Unterweger H, Dézsi L, Matuszak J, Janko C, Poettler M, Jordan J, et al. Dextrancoated superparamagnetic iron oxide nanoparticles for magnetic resonance imaging: Evaluation of size-dependent imaging properties, storage stability and safety. International Journal of Nanomedicine. 2018:1899-915.
- [40] Khan MS, Gowda BJ, Nasir N, Wahab S, Pichika MR, Sahebkar A, et al. Advancements in dextran-based nanocarriers for treatment and imaging of breast cancer. International Journal of Pharmaceutics. 2023:123276.
- [41] Lartigue L, Hugounenq P, Alloyeau D, Clarke SP, Lévy M, Bacri JC, et al. Cooperative organization in iron oxide multi-core nanoparticles potentiates their efficiency as heating mediators and MRI contrast agents. ACS Nano. 2012;6(12):10935-49.
- [42] Confalonieri GB, Vega V, Ebbing A, Mishra D, Szary P, Prida VM, et al. Templateassisted self-assembly of individual and clusters of magnetic nanoparticles. Nanotechnology. 2011;22(28):285608.
- [43] Griffiths DJ, Schroeter DF. Introduction to quantum mechanics. Cambridge University Press; 2018.
- [44] Coey JM. Magnetism and magnetic materials. Cambridge University Press; 2010.
- [45] Griffiths DJ. Introduction to electrodynamics. Cambridge University Press; 2023.
- [46] Kanamori J. Superexchange interaction and symmetry properties of electron orbitals. Journal of Physics and Chemistry of Solids. 1959;10(2-3):87-98.
- [47] Kohn W. Theory of Bloch electrons in a magnetic field: the effective Hamiltonian. Physical Review. 1959;115(6):1460.
- [48] Blundell S. Magnetism in condensed matter. OUP Oxford; 2001.
- [49] Barsan V. Inverse Langevin and Brillouin functions: mathematical properties and physical applications. arXiv preprint arXiv:190207641. 2019.
- [50] Visintin A. A Weiss-type model of ferromagnetism. Physica B: Condensed Matter. 2000;275(1-3):87-91.
- [51] Getzlaff M. Fundamentals of magnetism. Springer Science & Business Media; 2007.
- [52] Singh J. Modern physics for engineers. John Wiley & Sons; 2008.

[53] van Vleck JH. On the anisotropy of cubic ferromagnetic crystals. Physical Review. 1937;52(11):1178.

- [54] Buschow KJ, Cahn RW, Flemings MC, Ilschner B, Kramer EJ, Mahajan S. Encyclopedia of Materials: Science and Technology. MRS Bulletin. 2004;29(7):512-2.
- [55] Řezníček R, Chlan V, Štěpánková H, Novák P, Maryško M. Magnetocrystalline anisotropy of magnetite. Journal of Physics: Condensed Matter. 2012;24(5):055501.
- [56] Arora K, Cazenave A, Engdahl ER, Kind R, Manglik A, Roy S, et al. Encyclopedia of solid earth geophysics. Springer Science & Business Media; 2011.
- [57] Guimarães AP, Guimaraes AP. Principles of nanomagnetism. vol. 7. Springer; 2009.
- [58] Tannous C, Gieraltowski J. The Stoner-Wohlfarth model of ferromagnetism. European Journal of Physics. 2008;29(3):475.
- [59] Stoner EC, Wohlfarth E. A mechanism of magnetic hysteresis in heterogeneous alloys. Philosophical Transactions of the Royal Society of London Series A, Mathematical and Physical Sciences. 1948;240(826):599-642.
- [60] Rubel MH, Hossain MK. Crystal structures and properties of nanomagnetic materials. In: Fundamentals of Low Dimensional Magnets. CRC Press; 2022. p. 183-205.
- [61] Bedanta S, Kleemann W. Supermagnetism. Journal of Physics D: Applied Physics. 2008;42(1):013001.
- [62] Henrard D, Vuong QL, Delangre S, Valentini X, Nonclercq D, Gonon MF, et al. Monitoring of superparamagnetic particle sizes in the Langevin law regime. Journal of Nanomaterials. 2019:2019:1-9.
- [63] Knobel M, Nunes W, Socolovsky L, De Biasi E, Vargas J, Denardin J. Superparamagnetism and other magnetic features in granular materials: a review on ideal and real systems. Journal of Nanoscience and Nanotechnology. 2008;8(6):2836-57.
- [64] Koksharov YA. Magnetism of nanoparticles: effects of size, shape, and interactions. Magnetic Nanoparticles. 2009:197-254.
- [65] Dormann JL, Fiorani D, Tronc E. Magnetic relaxation in fine-particle systems. Advances in Chemical Physics. 1997;98:283-494.
- [66] Petracic O, Chen X, Bedanta S, Kleemann W, Sahoo S, Cardoso S, et al. Collective states of interacting ferromagnetic nanoparticles. Journal of Magnetism and Magnetic Materials. 2006;300(1):192-7.
- [67] Parker D, Dupuis V, Ladieu F, Bouchaud JP, Dubois E, Perzynski R, et al. Spin-glass behavior in an interacting  $\gamma$ -Fe<sub>2</sub>O<sub>3</sub> nanoparticle system. Physical Review B—Condensed Matter and Materials Physics. 2008;77(10):104428.

[68] Sahoo S, Petracic O, Kleemann W, Nordblad P, Cardoso S, Freitas P. Aging and memory in a superspin glass. Physical Review B. 2003;67(21):214422.

- [69] Jonsson T, Mattsson J, Djurberg C, Khan F, Nordblad P, Svedlindh P. Aging in a magnetic particle system. Physical review letters. 1995;75(22):4138.
- [70] Brückel T. A 1 100 years of scattering and beyond. Scattering Methods for Condensed Matter Research: Towards Novel Applications at Future Sources (M Angst, T Brückel, D Richter, and R Zorn, eds), Jülich: Forschungszentrum Jülich. 2012.
- [71] Brückel T. Neutron Scattering: Lectures of the JCNS Laboratory Course Held at the Forschungszentrum Jülich and the Research Reactor FRM II of TU Munich. vol. 38. Forschungszentrum Jülich; 2007.
- [72] Feigin L, Svergun DI, et al. Structure analysis by small-angle X-ray and neutron scattering. vol. 1. Springer; 1987.
- [73] Shull C, Wollan E. X-ray, electron, and neutron diffraction. Science. 1948;108(2795):69-75.
- [74] Kittel C, McEuen P. Introduction to solid state physics. John Wiley & Sons; 2018.
- [75] Beaucage G, Schaefer DW. Structural studies of complex systems using small-angle scattering: a unified Guinier/power-law approach. Journal of Non-Crystalline Solids. 1994;172:797-805.
- [76] Gommes CJ, Jaksch S, Frielinghaus H. Small-angle scattering for beginners. Applied Crystallography. 2021;54(6):1832-43.
- [77] Oliveira CLP, et al. Investigating macromolecular complexes in solution by small angle X-ray scattering. Current Trends in X-ray Crystallography. 2011:367-92.
- [78] Li T, Senesi AJ, Lee B. Small angle X-ray scattering for nanoparticle research. Chemical Reviews. 2016;116(18):11128-80.
- [79] Tang P, Greenwood J, Raper JA. A model to describe the settling behavior of fractal aggregates. Journal of Colloid and Interface Science. 2002;247(1):210-9.
- [80] Hashimoto T. Combined Small-Angle Scattering Methods for Analyses of Hierarchical Structures. In: Principles and Applications of X-ray, Light and Neutron Scattering. Springer; 2022. p. 407-56.
- [81] Londoño OM, Tancredi P, Rivas P, Muraca D, Socolovsky LM, Knobel M. Small-angle X-ray scattering to analyze the morphological properties of nanoparticulated systems. Handbook of Materials Characterization. 2018:37-75.
- [82] Sobry R, Ledent J, Fontaine F. Application of an extended Porod law to the study of the ionic aggregates in telechelic ionomers. Journal of Applied Crystallography. 1991;24(5):516-25.

[83] Glatter O, May R. Small-angle techniques. International Tables for Crystallography. 2006;100:89-112.

- [84] Larsen AH, Pedersen JS, Arleth L. Assessment of structure factors for analysis of small-angle scattering data from desired or undesired aggregates. Journal of Applied Crystallography. 2020;53(4):991-1005.
- [85] Feoktystov A, Avdeev M, Aksenov V, Petrenko V, Bulavin L, Bica D, et al. Contrast variation in small-angle neutron scattering from magnetic fluids stabilized by different mono-carboxylic acids. Solid State Phenomena. 2009;152:186-9.
- [86] Brumberger H. Modern aspects of small-angle scattering. vol. 451. Springer Science & Business Media; 2013.
- [87] Stuhrmann H. Small-angle x-ray scattering of macromolecules in solution. In: Synchrotron Radiation Research. Springer; 1980. p. 513-31.
- [88] Haas S, Zehl G, Dorbandt I, Manke I, Bogdanoff P, Fiechter S, et al. Direct accessing the nanostructure of carbon supported Ru- Se based catalysts by ASAXS. The Journal of Physical Chemistry C. 2010;114(51):22375-84.
- [89] Kumar CS. X-ray and neutron techniques for nanomaterials characterization. Springer; 2016.
- [90] Borsali R, Pecora R. Soft-matter characterization. Springer Science & Business Media; 2008.
- [91] Bill E. Chapter 6—57Fe-Mössbauer spectroscopy and basic interpretation of Mössbauer parameters. Practical Approaches to Biological Inorganic Chemistry, 2nd edn Elsevier, Amsterdam. 2013:201-28.
- [92] Waerenborgh JC, Tavares P, Pereira AS. Mössbauer spectroscopy. Radiation in Bioanalysis: Spectroscopic Techniques and Theoretical Methods. 2019:213-44.
- [93] Mørup S, Brok E, Frandsen C. Spin structures in magnetic nanoparticles. Journal of Nanomaterials. 2013;2013(1):720629.
- [94] Prigogine I, Rice SA. Advances in Chemical Physics. vol. 250. John Wiley & Sons; 2009.
- [95] Friedman A, Friedman A. Micromagnetics. Mathematics in Industrial Problems: Part 5. 1992:182-92.
- [96] Fidler J, Schrefl T. Micromagnetic modelling-the current state of the art. Journal of Physics D: Applied Physics. 2000;33(15):R135.
- [97] Wu K, Wang JP. Magnetic nanoparticles in nanomedicine. Elsevier; 2024.

[98] Miltat JE, Donahue MJ, et al. Numerical micromagnetics: Finite difference methods. Handbook of Magnetism and Advanced Magnetic Materials. 2007;2:742-64.

- [99] Fischbacher J, Kovacs A, Gusenbauer M, Oezelt H, Exl L, Bance S, et al. Micromagnetics of rare-earth efficient permanent magnets. Journal of Physics D: Applied Physics. 2018;51(19):193002.
- [100] Scholz W, Schrefl T, Fidler J. Micromagnetic simulation of thermally activated switching in fine particles. Journal of Magnetism and Magnetic Materials. 2001;233(3):296-304.
- [101] Lemcke O. Implementation of temperature in micromagnetic simulations. Interdisciplinary Nanoscience Center Hamburg, University of Hamburg, Hamburg, Germany. 2004. Available online: http://www.nanoscience.de/group\_r/stmspstm/ projects/temperature/download.shtml.
- [102] Donahue MJ, Porter DG. OOMMF User's Guide: Version 1.0. National Institute of Standards and Technology Gaithersburg, MD; 1999.
- [103] Kentzinger E, Krutyeva M, Rücker U. GALAXI: Gallium anode low-angle x-ray instrument. Journal of large-scale research facilities JLSRF. 2016;2:A61-1.
- [104] Haas S, Sun X, Conceição A, Horbach J, Pfeffer S. The new small-angle X-ray scattering beamline for materials research at PETRA III: SAXSMAT beamline P62. Journal of Synchrotron Radiation. 2023;30(6).
- [105] Evans J. X-ray absorption spectroscopy for the chemical and materials sciences. John Wiley & Sons; 2018.
- [106] Gilbert EP, Schulz JC, Noakes TJ. 'Quokka'—the small-angle neutron scattering instrument at OPAL. Physica B: Condensed Matter. 2006;385:1180-2.
- [107] Wood K, Mata JP, Garvey CJ, Wu CM, Hamilton WA, Abbeywick P, et al. QUOKKA, the pinhole small-angle neutron scattering instrument at the OPAL Research Reactor, Australia: design, performance, operation and scientific highlights. Journal of Applied Crystallography. 2018;51(2):294-314.
- [108] Ersez T, Braoudakis G, Osborn J. Radiation shielding for neutron guides. Physica B: Condensed Matter. 2006;385:1268-70.
- [109] Kline SR. Reduction and analysis of SANS and USANS data using IGOR Pro. Journal of Applied Crystallography. 2006;39(6):895-900.
- [110] Josephson BD. Possible new effects in superconductive tunnelling. Physics Letters. 1962;1(7):251-3.
- [111] José Martínez-Pérez M, Koelle D. NanoSQUIDs: Basics & recent advances. Physical Sciences Reviews. 2017;2(8):20175001.

[112] Kleiner R, Koelle D, Ludwig F, Clarke J. Superconducting quantum interference devices: State of the art and applications. Proceedings of the IEEE. 2004;92(10):1534-48.

- [113] Friedrich B, Lyer S, Janko C, Unterweger H, Brox R, Cunningham S, et al. Scavenging of bacteria or bacterial products by magnetic particles functionalized with a broad-spectrum pathogen recognition receptor motif offers diagnostic and therapeutic applications. Acta Biomaterialia. 2022;141:418-28.
- [114] Buchner M, Höfler K, Henne B, Ney V, Ney A. Tutorial: Basic principles, limits of detection, and pitfalls of highly sensitive SQUID magnetometry for nanomagnetism and spintronics. Journal of Applied Physics. 2018;124(16).
- [115] Kuntsche J, Horst JC, Bunjes H. Cryogenic transmission electron microscopy (cryo-TEM) for studying the morphology of colloidal drug delivery systems. International Journal of Pharmaceutics. 2011;417(1-2):120-37.
- [116] Carter DBWCB. Transmission electron microscopy A textbook for materials science; 2009.
- [117] Leng Y. Materials characterization: introduction to microscopic and spectroscopic methods. John Wiley & Sons; 2013.
- [118] Ponce A, Mejía-Rosales S, José-Yacamán M. Scanning transmission electron microscopy methods for the analysis of nanoparticles. Nanoparticles in Biology and Medicine: Methods and Protocols. 2012:453-71.
- [119] Harris JR. Transmission electron microscopy in molecular structural biology: a historical survey. Archives of Biochemistry and Biophysics. 2015;581:3-18.
- [120] Weissenberger G, Henderikx RJ, Peters PJ. Understanding the invisible hands of sample preparation for cryo-EM. Nature Methods. 2021;18(5):463-71.
- [121] Duisburg-Essen U. U. von Hörsten; Nov. 2024. http://udue.de/pi.
- [122] Abdellatief M, Najdawi MA, Momani Y, Aljamal B, Abbadi A, Harfouche M, et al. Operational status of the X-ray powder diffraction beamline at the SESAME synchrotron. Synchrotron Radiation. 2022;29(2):532-9.
- [123] Stetefeld J, McKenna SA, Patel TR. Dynamic light scattering: a practical guide and applications in biomedical sciences. Biophysical reviews. 2016;8:409-27.
- [124] Unterweger H, Tietze R, Janko C, Zaloga J, Lyer S, Dürr S, et al. Development and characterization of magnetic iron oxide nanoparticles with a cisplatin-bearing polymer coating for targeted drug delivery. International Journal of Nanomedicine. 2014:3659-76.

[125] Mekseriwattana W, Guardia P, Herrero BT, de la Fuente JM, Kuhakarn C, Roig A, et al. Riboflavin-citrate conjugate multicore SPIONs with enhanced magnetic responses and cellular uptake in breast cancer cells. Nanoscale Advances. 2022;4(8):1988-98.

- [126] Xiao Z, Zhang L, Colvin VL, Zhang Q, Bao G. Synthesis and application of magnetic nanocrystal clusters. Industrial & Engineering Chemistry Research. 2022;61(22):7613-25.
- [127] Rahman MM, Khan SB, Jamal A, Faisal M, Aisiri AM. Iron oxide nanoparticles. Nanomaterials. 2011;3:43-67.
- [128] Lübbe AS, Alexiou C, Bergemann C. Clinical applications of magnetic drug targeting. Journal of Surgical Research. 2001;95(2):200-6.
- [129] Sadighian S, Rostamizadeh K, Hosseini-Monfared H, Hamidi M. Doxorubicinconjugated core—shell magnetite nanoparticles as dual-targeting carriers for anticancer drug delivery. Colloids and Surfaces B: Biointerfaces. 2014;117:406-13.
- [130] Dutz S, Hergt R. Magnetic nanoparticle heating and heat transfer on a microscale: Basic principles, realities and physical limitations of hyperthermia for tumour therapy. International Journal of Hyperthermia. 2013;29(8):790-800.
- [131] Maity D, Kandasamy G. Superparamagnetic nanoparticles for cancer hyperthermia treatment. Nanotechnology Characterization Tools for Tissue Engineering and Medical Therapy. 2019:299-332.
- [132] Ludwig F, Eberbeck D, Löwa N, Steinhoff U, Wawrzik T, Schilling M, et al. Characterization of magnetic nanoparticle systems with respect to their magnetic particle imaging performance. Biomedizinische Technik/Biomedical Engineering. 2013;58(6):535-45.
- [133] Cullity BD, Graham CD. Introduction to Magnetic Materials. John Wiley & Sons; 2011.
- [134] Sidhu P, Gilkes R, Posner A. Mechanism of the low temperature oxidation of synthetic magnetites. Journal of Inorganic and Nuclear Chemistry. 1977;39(11):1953-8.
- [135] Sharma VK, Klingelhofer G, Nishida T. Mössbauer spectroscopy: applications in chemistry, biology, and nanotechnology. John Wiley & Sons; 2013.
- [136] Cox P. Transition Metal Oxides. Oxford Science Publications. Clarendon Press Oxford; 1992.
- [137] Morin F. Magnetic susceptibility of  $\alpha$ -Fe<sub>2</sub>O<sub>3</sub> and  $\alpha$ -Fe<sub>2</sub>O<sub>3</sub> with added titanium. Physical Review. 1950;78(6):819.

[138] Roth W. Defects in the crystal and magnetic structures of ferrous oxide. Acta Crystallographica. 1960;13(2):140-9.

- [139] Khalafalla S, Reimers G. Preparation of dilution-stable aqueous magnetic fluids. IEEE Transactions on Magnetics. 1980;16(2):178-83.
- [140] Massart R. Preparation of aqueous magnetic liquids in alkaline and acidic media. IEEE Transactions on Magnetics. 1981;17(2):1247-8.
- [141] Laurent S, Forge D, Port M, Roch A, Robic C, Vander Elst L, et al. Magnetic iron oxide nanoparticles: synthesis, stabilization, vectorization, physicochemical characterizations, and biological applications. Chemical Reviews. 2008;108(6):2064-110.
- [142] Mühlberger M, Janko C, Unterweger H, Friedrich RP, Friedrich B, Band J, et al. Functionalization of T lymphocytes with citrate-coated superparamagnetic iron oxide nanoparticles for magnetically controlled immune therapy. International Journal of Nanomedicine. 2019:8421-32.
- [143] Jung CW. Surface properties of superparamagnetic iron oxide MR contrast agents: ferumoxides, ferumoxtran, ferumoxsil. Magnetic Resonance Imaging. 1995;13(5):675-91.
- [144] Abràmoff MD, Magalhães PJ, Ram SJ. Image processing with ImageJ. Biophotonics International. 2004;11(7):36-42.
- [145] Crow EL, Shimizu K. Lognormal distributions. Marcel Dekker New York; 1987.
- [146] Scherrer P. Bestimmung der Grosse und inneren Struktur von Kolloidteilchen mittels Rontgenstrahlen. Nach Ges Wiss Gottingen. 1918;2:8-100.
- [147] Mishra Y, Mohapatra S, Kabiraj D, Mohanta B, Lalla N, Pivin J, et al. Synthesis and characterization of Ag nanoparticles in silica matrix by atom beam sputtering. Scripta Materialia. 2007;56(7):629-32.
- [148] Borchert H, Shevchenko EV, Robert A, Mekis I, Kornowski A, Grübel G, et al. Determination of nanocrystal sizes: a comparison of TEM, SAXS, and XRD studies of highly monodisperse CoPt3 particles. Langmuir. 2005;21(5):1931-6.
- [149] Whittig L, Allardice W. X-ray diffraction techniques. Methods of Soil Analysis: Part 1 Physical and Mineralogical Methods. 1986;5:331-62.
- [150] Köhler T, Feoktystov A, Petracic O, Nandakumaran N, Cervellino A, Brückel T. Signature of antiphase boundaries in iron oxide nanoparticles. Journal of Applied Crystallography. 2021;54(6):1719-29.
- [151] Jensen H, Pedersen JH, J rgensen J, Pedersen JS, Joensen KD, Iversen SB, et al. Determination of size distributions in nanosized powders by TEM, XRD, and SAXS. Journal of Experimental Nanoscience. 2006;1(3):355-73.

[152] Langford J, Louër D, Scardi P. Effect of a crystallite size distribution on X-ray diffraction line profiles and whole-powder-pattern fitting. Journal of Applied Crystallography. 2000;33(3):964-74.

- [153] Beaucage G. Small-angle scattering from polymeric mass fractals of arbitrary mass-fractal dimension. Journal of Applied Crystallography. 1996;29(2):134-46.
- [154] Svergun D. Determination of the regularization parameter in indirect-transform methods using perceptual criteria. Journal of Applied Crystallography. 1992;25(4):495-503.
- [155] Yari P, Chugh VK, Saha R, Tonini D, Rezaei B, Mostufa S, et al. Static and dynamic magnetization models of magnetic nanoparticles: an appraisal. Physica Scripta. 2023;98(8):082002.
- [156] Plouffe BD, Nagesha DK, DiPietro RS, Sridhar S, Heiman D, Murthy SK, et al. Thermomagnetic determination of Fe<sub>3</sub>O<sub>4</sub> magnetic nanoparticle diameters for biomedical applications. Journal of Magnetism and Magnetic Materials. 2011;323(17):2310-7.
- [157] Nandakumaran N, Barnsley L, Feoktystov A, Ivanov SA, Huber DL, Fruhner LS, et al. Unravelling magnetic nanochain formation in dispersion for in vivo applications. Advanced Materials. 2021;33(24):2008683.
- [158] Frison R, Cernuto G, Cervellino A, Zaharko O, Colonna GM, Guagliardi A, et al. Magnetite-maghemite nanoparticles in the 5–15 nm range: correlating the core-shell composition and the surface structure to the magnetic properties. A total scattering study. Chemistry of Materials. 2013;25(23):4820-7.
- [159] Stuhrmann H. Neutron small-angle scattering of biological macromolecules in solution. Journal of Applied Crystallography. 1974;7(2):173-8.
- [160] Köhler T, Feoktystov A, Petracic O, Kentzinger E, Bhatnagar-Schöffmann T, Feygenson M, et al. Mechanism of magnetization reduction in iron oxide nanoparticles. Nanoscale. 2021;13(14):6965-76.
- [161] Avdeev MV, Aksenov VL. Small-angle neutron scattering in structure research of magnetic fluids. Physics-Uspekhi. 2010;53(10):971.
- [162] Périgo ÉA, Gilbert EP, Metlov KL, Michels A. Experimental observation of magnetic poles inside bulk magnets via Fourier modes of magnetostatic field. New Journal of Physics. 2014;16(12):123031.
- [163] Mühlbauer S, Honecker D, Périgo ÉA, Bergner F, Disch S, Heinemann A, et al. Magnetic small-angle neutron scattering. Reviews of Modern Physics. 2019;91(1):015004.
- [164] Landers J, Stromberg F, Darbandi M, Schöppner C, Keune W, Wende H. Correlation of superparamagnetic relaxation with magnetic dipole interaction in capped ironoxide nanoparticles. Journal of Physics: Condensed Matter. 2014;27(2):026002.

[165] Peddis D, Yaacoub N, Ferretti M, Martinelli A, Piccaluga G, Musinu A, et al. Cationic distribution and spin canting in CoFe<sub>2</sub>O<sub>4</sub> nanoparticles. Journal of Physics: Condensed Matter. 2011;23(42):426004.

- [166] Goss C. Saturation magnetisation, coercivity and lattice parameter changes in the system Fe<sub>3</sub>O<sub>4</sub>-γFe<sub>2</sub>O<sub>3</sub>, and their relationship to structure. Physics and Chemistry of Minerals. 1988;16(2):164-71.
- [167] Batlle X, Pérez N, Guardia P, Iglesias O, Labarta A, Bartolomé F, et al. Magnetic nanoparticles with bulklike properties. Journal of Applied Physics. 2011;109(7).
- [168] WebMineral. Maghemite; 2024. Available from: https://webmineral.com/data/Maghemite.shtml.
- [169] Lak A, Disch S, Bender P. Embracing defects and disorder in magnetic nanoparticles. Advanced Science. 2021;8(7):2002682.
- [170] Coduri M, Masala P, Del Bianco L, Spizzo F, Ceresoli D, Castellano C, et al. Local structure and magnetism of Fe<sub>2</sub>O<sub>3</sub> maghemite nanocrystals: The role of crystal dimension. Nanomaterials. 2020;10(5):867.
- [171] Morales MdP, Veintemillas-Verdaguer S, Montero M, Serna C, Roig A, Casas L, et al. Surface and internal spin canting in  $\gamma$ -Fe<sub>2</sub>O<sub>3</sub> nanoparticles. Chemistry of Materials. 1999;11(11):3058-64.
- [172] Sidhu P, Gilkes R, Posner A. Mechanism of the low temperature oxidation of synthetic magnetites. Journal of Inorganic and Nuclear Chemistry. 1977;39(11):1953-8.
- [173] Kabelitz A, Guilherme A, Joester M, Reinholz U, Radtke M, Bienert R, et al. Time-resolved in situ studies on the formation mechanism of iron oxide nanoparticles using combined fast-XANES and SAXS. CrystEngComm. 2015;17(44):8463-70.
- [174] Pati S, Gopinath S, Panneerselvam G, Antony M, Philip J. High temperature phase transformation studies in magnetite nanoparticles doped with Co<sup>2+</sup> ion. Journal of Applied Physics. 2012;112(5).
- [175] Heider F, Williams W. Note on temperature dependence of exchange constant in magnetite. Geophysical Research Letters. 1988;15(2):184-7.
- [176] Fletcher E, O'reilly W. Contribution of Fe<sup>2+</sup> ions to the magnetocrystalline anisotropy constant K1 of Fe<sub>3-X</sub>Ti<sub>x</sub>O<sub>4</sub> (0< x < 0.1). Journal of Physics C: Solid State Physics. 1974;7(1):171.
- [177] Lewis GR, Loudon JC, Tovey R, Chen YH, Roberts AP, Harrison RJ, et al. Magnetic vortex states in toroidal iron oxide nanoparticles: Combining micromagnetics with tomography. Nano Letters. 2020;20(10):7405-12.

[178] Betto D, Coey J. Vortex state in ferromagnetic nanoparticles. Journal of Applied Physics. 2014;115(17).

- [179] Tsiantos V, Scholz W, Suess D, Schrefl T, Fidler J. The effect of the cell size in Langevin micromagnetic simulations. Journal of Magnetism and Magnetic Materials. 2002;242:999-1001.
- [180] Du H, Du A. Effect of exchange and dipolar interactions on the hysteresis of magnetic nanoparticle systems. physica Status Solidi (b). 2007;244(4):1401-8.
- [181] Jonsson T, Nordblad P, Svedlindh P. Dynamic study of dipole-dipole interaction effects in a magnetic nanoparticle system. Physical Review B. 1998;57(1):497.
- [182] El-Hilo M, Chantrell R, O'grady K. A model of interaction effects in granular magnetic solids. Journal of Applied Physics. 1998;84(9):5114-22.

Band / Volume 283

### The role of cellular development in multicellular antiphage defense of *Streptomyces*

T. Luthe (2024), vi, 173 pp ISBN: 978-3-95806-768-4

Band / Volume 284

#### Probing the Transformation from Transition Metal Complexes to Extended Two-Dimensional Nanostructures

D. Baranowski (2024), XII, 103 pp

ISBN: 978-3-95806-772-1

#### Band / Volume 285

#### **Neutron Scattering**

Lectures of the JCNS Laboratory Course held at Forschungszentrum Jülich and at the Heinz-Maier-Leibnitz Zentrum Garching edited by S. Förster, K. Friese, M. Kruteva, S. Nandi, M. Zobel, R. Zorn (2024), ca. 365 pp

ISBN: 978-3-95806-774-5

Band / Volume 286

#### Ab initio investigation of intrinsic antiferromagnetic solitons

Amal Jawdat Nayef Aldarawsheh (2024), xv, 164 pp

ISBN: 978-3-95806-785-1

Band / Volume 287

### Understanding the dynamics of Plant-Bacteria-Bacteriophage interactions as a means to improve plant performance

S. H. Erdrich (2024), ix, 176 pp ISBN: 978-3-95806-791-2

Band / Volume 288

# Prediction of Magnetic Materials for Energy and Information Combining Data-Analytics and First-Principles Theory

R. Hilgers (2024), xv, 215 pp ISBN: 978-3-95806-795-0

Band / Volume 289

#### Biodegradation and microbial upcycling of plastics

J. de Witt (2025), XVI, 259 pp ISBN: 978-3-95806-804-9

Band / Volume 290

## Practical Methods for Efficient Analytical Control in Superconducting Qubits

B. Li (2025), 202 pp ISBN: 978-3-95806-807-0

#### Schriften des Forschungszentrums Jülich Reihe Schlüsseltechnologien / Key Technologies

Band / Volume 291

### Ab initio investigation of topological magnetism in two-dimensional van der Waals heterostructures

N. Abuawwad (2025), xviii, 135 pp

ISBN: 978-3-95806-808-7

Band / Volume 292

### Tolerance engineering of Pseudomonas for the efficient conversion and production of aldehydes

T. Lechtenberg (2025), XVI, 185 pp

ISBN: 978-3-95806-817-9

Band / Volume 293

Exploring the process window for production of itaconic,

#### 2-hydroxyparaconic, and itatartaric acid with engineered Ustilago strains

P. Ernst (2025), x, 145 pp ISBN: 978-3-95806-825-4

Band / Volume 294

### Surface Plasmon Resonance Microscopy for the Characterization of Cell-Substrate Distances

J. Bednar (2025), xxiii, 187 pp ISBN: 978-3-95806-830-8

Band / Volume 295

## Microfluidic-MEA hybrid systems for electrophysiological recordings of neuronal co-cultures

J. Stevanović (2025), ix, 186 pp ISBN: 978-3-95806-831-5

Band / Volume 296

# Structural and Magnetic Properties of Biocompatible Iron Oxide Nanoparticles for Medical Applications

A. Nasser (2025), xii, 140 pp ISBN: 978-3-95806-837-7

Weitere Schriften des Verlags im Forschungszentrum Jülich unter

http://wwwzb1.fz-juelich.de/verlagextern1/index.asp

Schlüsseltechnologien / Key Technologies Band / Volume 296 ISBN 978-3-95806-837-7

